

EXPERIMENTAL STUDY OF COIL AND SHELL  
PHASE CHANGE MATERIAL  
HEAT EXCHANGER

by

Ajinkya R. Patil

Submitted in partial fulfilment of the requirements  
for the degree of Master of Applied Science

at

Dalhousie University  
Halifax, Nova Scotia  
May 2020

© Copyright by Ajinkya R. Patil, 2020

## *Dedication*

*This study is wholeheartedly dedicated to my beloved father, mother, uncle, aunty and other family members, who have been my source of inspiration and gave me strength when I thought of giving up, who continually provided their moral, spiritual, emotional and financial support.*

# Table of Contents

List of Tables .....	v
List of Figures .....	vi
Abstract .....	ix
List of Abbreviations and Symbols Used .....	x
Acknowledgements .....	xii
Chapter 1: Introduction .....	1
1.1 Need for thermal energy storage .....	1
1.2 Types of thermal energy storage devices .....	2
1.2.1 Sensible heat storage .....	2
1.2.2 Latent heat storage .....	3
1.2.3 Thermochemical storage .....	4
1.3 Literature review .....	5
1.3.1 Operation of PCM-TES .....	6
1.3.2 Types of PCM .....	7
1.3.3 Designs of PCM-TES .....	10
1.3.4 Methods used to enhance the heat transfer rate of PCM-TES device .....	16
1.3.5 Methods used to evaluate the performance of PCM-TES .....	21
1.4 Research objectives .....	27
Chapter 2: Experimental design .....	29
2.1 PCM heat exchanger (PCM-HX) .....	29
2.2 Experimental setup .....	33
2.2.1 Heating and cooling circulating bath .....	34
2.2.2 Sensors .....	36
2.2.3 Data acquisition system .....	42
2.3 Experimental procedure .....	43

2.4 Data analysis methodology .....	48
2.4.1 Heat transfer rate.....	48
2.4.2 Uncertainty analysis.....	48
2.4.3 Accounting for the heat loss/gain by the PCM-HX.....	49
2.4.4 Total energy transfer.....	50
Chapter 3: Results and discussion.....	52
3.1 Temperature, energy and pressure results.....	52
3.2 Repeatability of the experimental setup.....	59
3.3 Charging experiment results.....	61
3.4 Discharging experiment results.....	67
3.5 HTF flow rate variation.....	73
3.6 Chapter conclusion.....	75
Chapter 4: Data reduction, comparison and discussion.....	77
4.1 Comparison of experiments using average power obtained over specific period...77	
4.2 Comparison of experiments using average power obtained over total energy stored/extracted .....	85
4.3 Comparison of experiments using normalized average heat transfer rate obtained over total energy stored/extracted .....	93
4.4 Comparison of used data reduction methods .....	97
4.5 Chapter conclusion.....	100
Chapter 5: Conclusion and future work.....	102
References.....	107
Appendix A: Copper coil drawings .....	116
Appendix B: Heat loss calculations .....	121
Appendix C: Data sheets.....	122



## List of Tables

Table 2.1: Thermophysical properties of dodecanoic acid (Desgrosseilliers <i>et al.</i> , 2013). .....	32
Table 2.2: Temperature sensor calibration data at different set point bath temperatures. ....	40
Table 2.3: List of performed experiments.....	47
Table 4.1: Percent deviation from the trendlines of different data reduction methods.....	99
Table 4.2: The mean $Q_{\text{norm}}$ values and their percent standard deviation for different configurations of PCM-HX.....	100

## List of Figures

Figure 1.1 Simplified schematic of a Shell-and-tube PCM-TES device. ....	11
Figure 2.1: Schematic representation and pictures of: a) PCM-HX and b) Copper coil.....	30
Figure 2.2: The 2D and 3D schematic representation of a) 1-coil, b) 2-coil and c) 3-coil setups of the PCM-HX. ....	31
Figure 2.3: a) A CAD model and b) a picture of experimental setup used in this study.....	33
Figure 2.4: Picture of the Cole-Parmer Polystat RK-12122-56 heating and cooling circulating water bath.....	34
Figure 2.5: Schematic diagram of water-bath flow circuit a) when experiments were carried out on the PCM-HX and b) when changing the water-bath temperature. ....	35
Figure 2.6: Picture of the Omega FTB 4605 flow meter .....	36
Figure 2.7: Various temperature sensors used in the experimental setup: a) Omega brand RTD Probe sensor with model number PR-22-3-100-A-1/8-0300-M12, b) T-type thermocouple with 1/8" diameter and 6" length, and c) T-type thermocouple with 1/16" diameter and 12" length. ....	38
Figure 2.8: 3D CAD model of the nylon holder. ....	39
Figure 2.9: Picture of an Omega brand PX26-015DV differential pressure transducer. ...	42
Figure 2.10: Picture of the NI-cDAQ 9174 chassis with the NI9213, NI9217, NI9435 and NI9237 modules mounted on it.....	43
Figure 2.11: Schematic representation of the temperature intervals used for all the experiments performed in this study.....	45
Figure 3.1: Typical trend of raw data obtained from different temperature sensors during a) charging and b) discharging processes. ....	53
Figure 3.2: Typical trend of raw data obtained from different temperature sensors during the a) charging and b) discharging processes performed on 1-coil, 2-coil and 3-coil setup. ....	56
Figure 3.3: Typical cumulative energy profiles obtained during the a) charging and b) discharging processes performed on 1-coil, 2-coil and 3-coil setup.....	57

Figure 3.4: Power curves obtained during the repeatability test performed on 2-coil and 3-coil setups with a HTF flow rate of 3.3 L/min: a) charging and b) discharging processes. ....	60
Figure 3.5: Equivalent energy ( $E$ ) experiment results (power curves) obtained during the charging process of a) 1-coil, b) 2-coil and c) 3-coil setups with a HTF flow rate of 3.3 L/min. ....	63
Figure 3.6: Same initial PCM temperature ( $T_i$ ) experiment results (power curves) obtained during the charging process of a) 1-coil, b) 2-coil and c) 3-coil setups with a HTF flow rate of 3.3 L/min. ....	65
Figure 3.7: Same final PCM temperature ( $T_R$ ) experiment results (power curves) obtained during the charging process of a) 1-coil, b) 2-coil and c) 3-coil setups with a HTF flow rate of 3.3 L/min. ....	67
Figure 3.8: Equivalent energy ( $E$ ) experiment results (power curves) obtained during the discharging process for the a) 1-coil, b) 2-coil and c) 3-coil setups with a HTF flow rate of 3.3 L/min. ....	69
Figure 3.9: Same initial PCM temperature ( $T_i$ ) experiment results (power curves) obtained during the discharging process of a) 1-coil, b) 2-coil and c) 3-coil setups with a HTF flow rate of 3.3 L/min. ....	71
Figure 3.10: Same final PCM temperature ( $T_R$ ) experiment results (power curves) obtained during the discharging process of a) 1-coil, b) 2-coil and c) 3-coil setups with a HTF flow rate of 3.3 L/min. ....	72
Figure 3.11: Heat transfer rates as a function of time using the 3-coil setup with flow rates of 3.3 and 6.3 L/min for various temperature combinations: a) during charging and b) during discharging. ....	74
Figure 4.1: Average system power over the first 2 hours as a function of the HTF temperature obtained during a) charging and b) discharging processes at 3.3 L/min HTF flow rate. ....	79
Figure 4.2: Average system power over the first 4 hours as a function of the HTF temperature obtained during a) charging and b) discharging processes at 3.3 L/min HTF flow rate. ....	80
Figure 4.3: Average system power over the first 2 hours as a function of $Ste_m$ for various $Ste_t$ obtained during a) charging and b) discharging processes at 3.3 L/min HTF flow rate. ....	83
Figure 4.4: Average system power over the first 4 hours as a function of $Ste_m$ for various $Ste_t$ obtained during a) charging and b) discharging processes at 3.3 L/min HTF flow rate. ....	84

Figure 4.5: Heat transfer rate as a function of stored energy obtained during the charging process of a) 1-coil, b) 2-coil and c) 3-coil setups with a HTF flow rate of 3.3 L/min.....	88
Figure 4.6: Heat transfer rate as a function of extracted energy obtained during the discharging process of a) 1-coil, b) 2-coil and c) 3-coil setups with a HTF flow rate of 3.3 L/min. ....	89
Figure 4.7: Average power obtained over the entire energy storage capacity as a function of $Ste_m$ for various $Ste_t$ obtained during a) charging and b) discharging processes at 3.3 L/min HTF flow rate.....	92
Figure 4.8: Normalized power ( $Q_{norm}$ ) as a function of $Ste_m$ for various $Ste_t$ obtained during a) charging and b) discharging processes at 3.3 L/min HTF flow rate. ....	94
Figure 4.9: Revised graph of normalized power ( $Q_{norm}$ ) as a function of $Ste_m$ for various $Ste_t$ obtained during a) charging and b) discharging processes at 3.3 L/min HTF flow rate.....	96
Figure 4.10: The charging experiment graph of average power obtained over the entire energy storage capacity as a function of $Ste_m$ for various $Ste_t$ with shown result trendlines.....	98
Figure A.1: Drawing of 1-coil setup coil or 3-coil setup middle coil.....	116
Figure A.2: Drawing of top coil in the 3-coil setup.....	117
Figure A.3: Drawing of bottom coil in the 3-coil setup.....	118
Figure A.4: Drawing of top coil in the 2-coil setup.....	119
Figure A.5: Drawing of bottom coil in the 2-coil setup.....	120

## **Abstract**

Phase change material-based thermal energy storage (PCM-TES) is a promising thermal energy storage technology because of its high energy storage density and narrower working transition temperature. These devices store energy in the form of latent heat in a phase change material. For these devices, there are no previously established guidelines to determine the relationship between the heat transfer rate, and their physical and operational parameters. To develop such guidelines for different PCM-TES configurations, their performance data at different operating conditions are needed.

In this work, different configurations of coil-and-shell type PCM-TES device are built and tested at different operating conditions. The obtained results are analyzed, and key parameters impacting the heat transfer process are identified. Also, an attempt is made to compare different experiments using melting Stefan number ( $Ste_m$ ), total Stefan number ( $Ste_t$ ), average heat transfer rate ( $Q_{avg}$ ) and normalized heat transfer rate ( $Q_{norm}$ ).

# List of Abbreviations and Symbols Used

## Abbreviations

<b>CAD</b>	Computer Aided Designed
<b>HTF</b>	Heat Transfer Fluid
<b>HX</b>	Heat Exchangers
<b>IEA</b>	International Energy Agency
<b>LAMTE</b>	Laboratory of Applied Multiphase Thermal Engineering
<b>LHS</b>	Latent Heat Storage
<b>Mtoe</b>	Million Tonne of Oil Equivalent
<b>NTU</b>	Number of Transfer Units
<b>PCM</b>	Phase Change Material
<b>PCM-HX</b>	Phase Change Material based Heat Exchanger
<b>PCM-TES</b>	Phase Change Material based Thermal Energy Storage Devices
<b>SHS</b>	Sensible Heat Storage
<b>SHSM</b>	Sensible Heat Storage Material
<b>TCS</b>	Thermochemical Storage
<b>TES</b>	Thermal Energy Storage

## Symbols

<b><math>A</math></b>	Metal contact area between the HTF and PCM
<b><math>C_{p,HTF}</math></b>	Specific heat of the HTF
<b><math>C_{p,l}</math></b>	Specific heat of the liquid PCM
<b><math>C_{p,pcm}</math></b>	Average of solid and liquid phase specific heat values of PCM
<b><math>C_{p1,pcm}</math></b>	Specific heat of the PCM at initial phase
<b><math>C_{p2,pcm}</math></b>	Specific heat of the PCM at final phase
<b><math>C_{p,s}</math></b>	Specific heat of the solid PCM
<b><math>C_{p,SHSM}</math></b>	Specific heat of the SHSM
<b><math>E_{SHS}</math></b>	Total energy stored/extracted from the SHS device
<b><math>E_{LHS}</math></b>	Total energy stored/extracted from the LHS device
<b><math>E</math></b>	Total energy stored/extracted from the PCM-HX
<b><math>E_{max}</math></b>	Upper limit of uncertainty in the $E$
<b><math>E_{min}</math></b>	Lower limit of uncertainty in the $E$
<b><math>k_s</math></b>	Thermal conductivity of solid PCM
<b><math>k_l</math></b>	Thermal conductivity of liquid PCM
<b><math>L</math></b>	Latent heat of the PCM
<b><math>\dot{m}_{HTF}</math></b>	Mass flow rate of the HTF
<b><math>\dot{m}_{HTF,norm}</math></b>	Normalized HTF thermal capacity flow rate
<b><math>m_{pcm}</math></b>	Mass of the PCM inside the LHS device
<b><math>m_{SHSM}</math></b>	Mass of the SHSM inside the SHS device

$Q(t)$	Heat transfer rate between the PCM and HTF measured by sensors
$Q_{actual}$	Instantaneous power stored/extracted from the PCM-HX
$Q_{actual,max}$	Upper limit of uncertainty in the $Q_{actual}$
$Q_{actual,min}$	Lower limit of uncertainty in the $Q_{actual}$
$Q_{therm}$	Normalized thermal power
$Q_{avg}$	Average power obtained during an experiment
$Q_{mean}$	Average power per unit energy stored
$Q_{mean,upper\ limit}$	Upper limit of uncertainty in the $Q_{mean}$ value
$Q_{mean,lower\ limit}$	Lower limit of uncertainty in the $Q_{mean}$ value
$Q_{norm}$	Normalized average power
$Ste_m$	Melting stefan number
$Ste_{m,c}$	Melting stefan number during the charging process
$Ste_{m,d}$	Melting stefan number during the discharging process
$Ste_t$	Total stefan number
$T_{f,SHSM}$	Final temperature of the SHSM
$T_{f,pcm}$	Final temperature of the PCM
$T_i$	Initial temperature of the PCM
$T_{in}$	HTF temperature at the inlet of the PCM-HX
$T_{i,pcm}$	Initial temperature of the PCM
$T_{i,SHSM}$	Initial temperature of the SHSM
$T_m$	PCM melting temperature
$T_{out}$	HTF temperature at the outlet of the PCM-HX
$T_R$	Reservoir / HTF temperature
$V_{HTF}$	HTF volume
$\varepsilon$	Effectiveness of the HX
$\rho_l$	Density of the liquid PCM
$\rho_s$	Density of the solid PCM
$dQ$	Uncertainty in the measured heat transfer rate between the HTF and PCM
$\Delta T_{avg}$	Average temperature difference between the HTF and PCM

## **Acknowledgements**

I would like to thank my supervisor Dr. Dominic Groulx for guidance and constant support over the course of this project, and my committee members, Dr. Jan Haelssig and Dr. Alain Joseph, for their time and feedback.

I would also like to acknowledge the technical and support staff in the Department of Mechanical Engineering, especially Kate Hide, Peter Jones, Jonathan MacDonald, Albert Murphy, Mark MacDonald and Angus MacPherson. Their help during this project was invaluable.

Thanks are also owed to my colleagues Mohammad Azad, Florent Herbinger and Maha Bhouri for sharing their technical knowledge and research experiences.

Lastly, I am grateful to the Natural Science and Engineering Research Council (NSERC) of Canada and the Canadian Foundation for Innovation (CFI) for their financial assistance in the development and operation of my experimental setup.



# **Chapter 1: Introduction**

## **1.1 Need for thermal energy storage**

Over the past centuries, excessive burning of fossil fuels has adversely affected our environment and slowly deteriorated our ecosystem. Combustion of fossil fuels produces greenhouse gases which are causing global warming and increasing worldwide pollution (Akhmat *et al.*, 2014). According to the data published by the International Energy Agency (IEA), from 1971 to 2016, the world primary energy supply has increased by almost 2.5 times and the use of fossil fuels has increased by roughly 234% from 4,768 to 11,156 million tonne of oil equivalent (Mtoe) (International Energy Agency (IEA), 2016; Skaalum and Groulx, 2017). Therefore, to restore our environment, it is crucial to reduce our dependence on fossil fuels through an increase in the utilization of clean and abundantly available renewable energy sources like solar, wind and tidal energy. However, the biggest drawback in the utilization of renewable energy sources is their intermittent nature. For example, the energy obtained by the sun at any given point on Earth varies with the time of day, the season of the year and the weather. A solution to this time dependency problem is to store energy during the periods of production and use the stored energy to meet energy demands when they occur at a later time; this could be achieved through the use of thermal energy storage (TES) devices (Nazir *et al.*, 2019).

Out of different types of available TES devices, latent heat based storage (LHS) systems are a very promising technology due to their high energy density and narrow operating temperature range (Groulx, 2018). However, the deployment of LHS devices is, in large part, restricted by the lack of proper design rules (Groulx, 2018). Design rules are

necessary to correlate the thermal performance and physical operating parameters of LHS devices. Thus, to develop such design rules, there is a need to collect quality data by performing systematic experiments on different LHS systems designs. Therefore, in this research work, one LHS device is built and systematic experiments are performed on it to gather this quality data. This gathered data will contribute to the development of design rules for LHS systems.

## **1.2 Types of thermal energy storage devices**

During energy production period, excess thermal energy can be stored in TES devices. During the demand period, the TES device can release the stored thermal energy to the user. Based on their working principle and material used, TES devices are classified into three main categories as follows.

1. Sensible Heat Storage (SHS)
2. Latent Heat Storage (LHS)
3. Thermochemical Storage (TCS)

### **1.2.1 Sensible heat storage**

Nowadays, sensible heat storage devices are ubiquitous in the heating system of residential and commercial buildings. The SHS device stores energy in the form of internal energy of its storage material by raising its temperature. As shown in Eq. (1.1), the amount of energy stored in the SHS device ( $E_{SHS}$ ) is proportional to the mass, specific heat and the change in temperature of the storage material used in it (Tatsidjodoung *et al.*, 2013).

$$E_{SHS} = m_{SHSM} \cdot C_{p,SHSM} \cdot |(T_{i,SHSM} - T_{f,SHSM})| \quad (1.1)$$

where,  $m_{SHSM}$ ,  $C_{p,SHSM}$ ,  $T_{i,SHSM}$  and  $T_{f,SHSM}$  are the mass, specific heat value, initial and final temperature of the sensible heat storage material (SHSM) respectively.

The specific heat values of most storage materials used lies roughly between 0.3 and 4.1 kJ/kg-K (Rempel and Rempel, 2013). A known problem encountered in SHS systems is the increase in potential heat losses from the system to the surroundings when the temperature of the system increases. This restricts the upper limit of the temperature that the storage material can be increased to. This is typically solved by using large amounts of insulation, which increases the cost of the SHS system. In this case, in order to increase the amount of energy stored, additional mass of storage material is used resulting in an increases in the size of SHS devices. Hence the SHS devices are less effective for storing large amount of energy in a limited available space (Lizana *et al.*, 2017).

### 1.2.2 Latent heat storage

Similar to SHS devices, latent heat storage devices also use an energy storage material, called phase change material (PCM). This material undergoes a phase transformation during its operation and a large amount of thermal energy is stored in this process. However, some amount of temperature difference is necessary through the PCM to conduct heat. Thus, some thermal energy is also stored in the form of sensible heat inside the LHS system (Nazir *et al.*, 2019). Equation (1.2) represents the total amount of energy stored in the LHS device ( $E_{LHS}$ ) operating over a range of temperature that encompasses the transition temperature of the material (Lizana *et al.*, 2017).

$$E_{LHS} = m_{pcm} \cdot \{C_{p1,pcm} \cdot |(T_{i,pcm} - T_m)| + L + C_{p2,pcm} \cdot |(T_m - T_{f,pcm})|\} \quad (1.2)$$

where,  $m_{pcm}$ ,  $C_{p1,pcm}$ ,  $C_{p2,pcm}$ ,  $T_{i,pcm}$ ,  $T_m$ ,  $T_{f,pcm}$  and  $L$  are the mass, specific heat value at the initial phase, specific heat value at the final phase, initial temperature, melting temperature, final temperature and latent heat energy of the PCM respectively.

The phase transition in LHS devices can be solid-solid, solid-liquid or liquid-gas depending on the material used and the working temperature of the LHS device (Pielichowska and Pielichowski, 2014; Praveen and Suresh, 2018). Out of these transitions, liquid-gas transitions have the highest energy storage density. However, these liquid-gas phase transitions involve large volume changes, which build high pressure inside the LHS device. Therefore, the device becomes risky to handle and requires a very robust and air-tight vessel; the cost is also increased drastically and makes them uneconomical for small scale applications (Pielichowska and Pielichowski, 2014). On the other hand, solid-solid phase transition LHS systems have the smallest energy storage density and are often very costly which makes them less practical options for storage devices (Pielichowska and Pielichowski, 2014). Solid-liquid phase transition LHS devices have larger energy storage density than the solid-solid LHS devices. Also, the solid-liquid phase transitions of PCM typically involves less than 10% volume changes during the phase transition, and does not require air-tight sealing, which makes its design simple and economical for small scale applications. Thus, the solid-liquid transition based LHS systems offers a very appealing storage solution (Tatsidjodoung *et al.*, 2013).

### **1.2.3 Thermochemical storage**

Thermochemical storage systems are the most energy-dense thermal storage system. They contain a material which undergoes a reversible chemical reaction during its operations. During these reversible chemical reactions, the thermal energy is used to break a larger

chemical molecule of the material into smaller molecules, and thermal energy is stored . When these smaller molecules later combine, they release energy in the form of an exothermic reversible reaction and provide it for usage. The volumetric energy density of TCS is about 5 times higher than LHS and 10 times higher than the SHS (Pardo *et al.*, 2014). However, this technology is still in the development stage, and is not commercially available. Also, it typically requires higher temperatures for their operation (Nazir *et al.*, 2019).

The LHS systems have higher energy density, narrower operating temperature range and negligible heat losses compared to SHS systems. Also, they often operate at a much lower temperature than a SHS of the same energy capacity. Besides, unlike TCS systems, LHS systems have been vigorously tested under different realistic conditions. Thus, to efficiently use renewable energy sources, LHS is a very promising technology which needs to be explored. Hence, in this thesis, a LHS system is used, and LHS will be discussed in more detail in the following literature review.

### **1.3 Literature review**

Every LHS device, also known as phase change based thermal energy storage devices (PCM-TES), is comprised of the following three components.

- A PCM with a melting temperature within the operating range of the storage application.
- An enclosure which stores the PCM
- A thermally conductive surface which separates the PCM and heat transfer fluid (HTF) flow. In most PCM-TES devices, these thermally conductive surfaces are made of material like copper and aluminium, and they are shaped in the form of channels or tubes.

### **1.3.1 Operation of PCM-TES**

PCM-TES devices are heat exchangers, where heat is exchanged between the PCM and HTF across the thin walls of channels inside the enclosure. Based on the direction of heat transfer, these heat transfer processes are classified into two types: 1) charging process and 2) discharging process.

#### ***Charging process:***

In the charging process, hot HTF flows through the inner channels and transfer heat to the relatively cold PCM. During this process, depending on the physical state of the PCM, energy is added in the form of sensible heat and latent heat at different parts of the PCM- TES simultaneously. Sensible heat is added to the subcooled solid-state PCM, and it is brought to the melting temperature. Latent heat is added to a solid-state PCM at the melting temperature leading to a change of phase to liquid. A large percentage of energy is stored in this process. Again, energy in the form of sensible heat is added to the molten PCM to keep raising its temperature towards the HTF temperature.

Experimental studies of PCM charging have shown that during the charging process, initially, the heat is transferred only via conduction. However, once enough volume of molten PCM forms, further heat transfer happens mainly by means of natural convection inside the PCM (Longeon *et al.*, 2013; Murray and Groulx, 2014; Karami and Kamkari, 2019). Due to the natural convection currents inside the molten PCM, the hot liquid PCM moves upward. Thus, the solid PCM in the upper part of LHS device melts quickly. On the other hand, in the lower portion of LHS device, heat is mainly added by means of conduction. Hence, the bottom side PCM melts slowly (Longeon *et al.*, 2013; Liu and Groulx, 2014).

### ***Discharging process:***

The process of extracting stored heat from the hotter molten PCM by passing relatively colder HTF through the inner tubes is called the discharging process. During discharging, initially the PCM in contact with the tubes releases its energy to the HTF and solid PCM is formed in between the remaining hot PCM and the wall of the HTF channel. As the PCM has very low thermal conductivity, this deposited solid PCM insulation adds additional thermal resistance causing a reduction in the heat transfer rate. As time passes, due to solidification, more and more PCM deposits around the HTF carrying tube, further increasing the thermal resistance. This phenomenon leads to a continuous decrease in the heat transfer rate (Longeon *et al.*, 2013). Also, unlike the charging process, the discharging process shows little to no evidence of natural convection and is mostly dominated by conduction heat transfer (Liu and Groulx, 2014).

### **1.3.2 Types of PCM**

PCM being an important part of a PCM-TES, the choice of the PCM is very important for any particular application. Ideally, PCM should have the following properties (Noël *et al.*, 2016):

- The melting temperature of the PCM should be within the operating range of the application.
- It should have high volumetric latent heat capacity to store a large amount of energy in a small space.
- It should have high thermal conductivity to store and discharge the energy at high rates.
- It should be chemically very stable so that it can be used for long-term applications without degrading over time.

- It should be non-toxic in nature.
- It must be inexpensive and readily available in the market to keep the system affordable.
- It should not exhibit supercooling.
- It should be non-corrosive to the container.

However, in the real world, it is very rare to find a PCM which possesses all these ideal characteristics. PCMs are classified into the following three groups based on their chemical nature.

### **1. Organic PCM**

Organic PCMs are composed of carbon, hydrogen and oxygen atoms. Various paraffins, fatty acids, alcohols, carbocyclic acids, amides, alkanes come under this category. Generally, the melting point of these materials lies between -40 to 150 °C (Tatsidjodoung *et al.*, 2013; Nazir *et al.*, 2019). Organic PCMs have considerably high latent heat values (around 100~300 kJ/kg) (Nazir *et al.*, 2019). They show very negligible supercooling, *i.e.*, the PCM solidifies at a temperature that is equal or only slightly below its melting temperature, and the latent heat from almost all the PCM can be extracted at the melting temperature of the PCM (Lizana *et al.*, 2017). Organic PCMs are also distinguished for their chemically stable nature and fixed melting temperature. However, they have a few significant drawbacks like low thermal conductivity and high flammability.

### **2. Inorganic PCM**

Various metals, metal alloys and salt hydrates fall into this category. These PCMs have very high volumetric latent heat storage capacity (up to 2 GJ/m<sup>3</sup>) (Pielichowska and



Pielichowski, 2014). They are classified into two major groups a) salt hydrate PCMs and a) metallic PCMs

**a) *Salt hydrate PCMs***

Salt hydrates are inorganic salts containing water crystallization. During the transition from solid to liquid the water molecules separate from the salts and anhydrous salt and water is obtained. In this process energy is stored in the form of latent heat (Pielichowska and Pielichowski, 2014).

The melting temperature of various salt hydrates varies from 14°C to 117°C, which makes them suitable for low-temperature applications and they have high energy storage capacity (up to 250 kJ/kg) (Pielichowska and Pielichowski, 2014). However, the salt hydrates have major drawbacks like high tendency to supercool, exhibiting incongruent melting. Due to supercooling, salt hydrates release the stored latent heat at lower temperatures and it decreases the efficiency of LHS devices. Again, the incongruent melting behaviour of salt hydrates results in phase segregation, which gradually decreases their performance. Usually, the phase segregation of salt hydrates is avoided by adding a thickening agent in it, which holds the salt hydrate molecules together (Cabeza *et al.*, 2003; Sharma *et al.*, 2009).

**b) *Metallic PCMs***

Metals and metal alloys come under this category. They have very high volumetric latent heat of fusion but low heat of fusion per weight (Tatsidjodoung *et al.*, 2013). They melt at high temperatures, which makes them unsuitable for domestic low-temperature

applications. However, they are suitable for concentrated solar power energy storage applications. Unlike organic PCMs, they have high thermal conductivity.

### ***3. Eutectic PCM***

Eutectic PCMs are mixtures of two or more components. They could be a combination of organic-organic, inorganic-inorganic or inorganic-organic compounds. Eutectic PCMs have some excellent characteristics like sharp melting temperatures, no phase segregation and possess high energy density. Usually, their latent heat capacity lies in between the organic and inorganic PCMs (Tatsidjodoung *et al.*, 2013; Pielichowska and Pielichowski, 2014).

#### **1.3.3 Designs of PCM-TES**

Most PCMs available for low and medium temperature applications possess very low thermal conductivity ( $k = 0.1$  to  $0.7$  W/m·K) (Lin *et al.*, 2018). This low thermal conductivity naturally results in low heat transfer rates during the charging and discharging processes of PCM-TES. Due to the low heat transfer rates, it takes a longer period to store and extract the energy from the LHS devices and makes them impractical for high energy rate demanding application (Groulx *et al.*, 2016). This problem is called the “rate problem”. To solve the rate problem, engineers have come up with different innovative designs of PCM-TES devices (Abdulateef *et al.*, 2018). Some of the major design types of PCM-TES are mentioned below.

#### ***Shell-and-tube design***

A shell-and-tube is the simplest design of PCM-TES devices (Longeon *et al.*, 2013). Due to its ease of fabrication and bulk energy storage capacity, it is widely studied in the

literature (Trp *et al.*, 2006; Akgun *et al.*, 2007; Hosseini *et al.*, 2014). Figure 1.1 shows a basic diagram of shell and tube PCM-TES. It consists of two concentric tubes which divide the PCM-TES into two parts. Out of these two parts, the PCM fills in one, whereas the HTF flows through the other. Generally, to avoid heat losses from the HTF to the surroundings, the HTF is passed through the inner tube and the PCM is stored in the outer annular space between the two tubes.

The heat transfer rate between the PCM and HTF is highest during the initial period of charging and discharging as the temperature difference between the PCM and HTF is highest at those instants. However, as time passes, the temperature difference between the PCM and HTF decreases, which results in a gradual decline in the heat transfer rate. Although simple to fabricate and easy to study, the simple shell-and-tube design is the worst one in terms of achievable power per unit volume of the PCM.

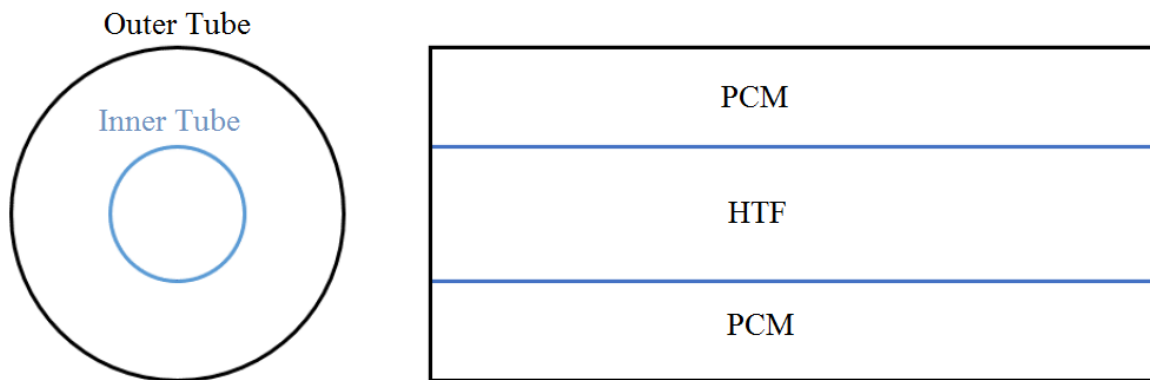


**Figure 1.1 Simplified schematic of a Shell-and-tube PCM-TES device.**

Some researchers tried to improve the heat transfer rate by increasing the natural convection dominated region inside the PCM-TES. Researchers like Yusuf Yazıcı *et al.* (2014) and Pahamli *et al.* (2016) designed eccentric horizontal shell-and-tube type PCM-TES in which the inner tube is moved downward from the center of its outer shell. In this study it was observed that the inner tube eccentricity increased the natural convection dominated region inside the PCM-TES, which resulted in higher heat transfer rates during the charging process compared to the concentric shell-and-tube PCM-TES design. However, during the solidification process in the eccentric shell-and-tube design, the thermal resistance in the upward direction increased by a large amount. It drastically increased the time required to finish the solidification process (Yazici *et al.*, 2014). Few studies investigated the effect of the orientation of shell-and-tube PCM-TES devices. It was observed that horizontal shell and tube PCM-TES designs give better heat transfer rates compared to the vertical ones (Seddegh *et al.*, 2016).

### ***Multiple PCM in a shell-and-tube***

While passing through the inner tubes of a shell-and-tube PCM-TES device, the HTF continuously exchanges heat with the surrounding PCM. In this process, the driving temperature difference of the HTF gradually decreases over the length of the inner tube. Therefore, the HTF exchanges less heat with the PCM near the exit point of the inner tubes than the entry point. Lower heat transfer rates are achieved at the HTF exit side of the inner tube compared to the entry side.

Thus, in order to get a high heat transfer rate over the length of the inner tube during the charging process, some researchers used multiple PCMs in the shell-and-tube PCM-TES. In this design, PCMs are kept side by side in the annular space in a decreasing melting

temperature order so that the lowest melting temperature PCM will be at the exit of the HTF carrying tube (Fang and Chen, 2007). Also, during the discharging process, similar thermal enhancement can be achieved by using this design. However, in that case, the HTF flow direction inside the device needs to be reversed. In this design, the improvement in heat transfer rate largely depends on the melting temperatures of the used PCMs.

### ***Shell-and-tube design with elliptical inner tube***

Similar to eccentricity, some researchers built a shell-and-tube heat exchanger with elliptical shape inner tube and studied the effect of the inner tube shape on the PCM heat transfer rates during the charging and discharging processes (Rabienataj Darzi *et al.*, 2016). Using a vertical elliptical tube instead of a circular HTF carrying inner tube showed an increase in the melting rate of the PCM-TES device. However, it decreased the overall solidification rate. A shell-and-tube LHS device with a horizontal elliptical tube did not show any improvements in the melting rate but reduced the solidification performance of the device [27].

### ***Coil-in-pipe design***

To increase the heat transfer area between the PCM and HTF, some studies employed different kinds of spiral inner tubes instead of a straight tube (Kabbara, 2015; Chen *et al.*, 2016; Ahmadi *et al.*, 2018; Zheng *et al.*, 2018; Ardahaie *et al.*, 2019). This design improved the heat transfer rate of the PCM-TES but decreased the latent heat storage capacity of the device. Also, in this design, the spiral tube diameter had a negligible effect on the heat transfer rate enhancement compared to the coil diameter.

### ***Shell-and-tube with fins***

To improve the heat transfer rate, researchers added different shaped fins to the HTF carrying tube of LHS devices (Rathod and Banerjee, 2015; Sciacovelli *et al.*, 2015; Abdulateef *et al.*, 2017; Pizzolato *et al.*, 2017; Abdulateef *et al.*, 2018; Kazemi *et al.*, 2018; Mahdi *et al.*, 2018; Mahdi and Nsofor, 2018). The added fins increased the heat transfer area between the PCM and HTF, which improved the heat transfer rate of the PCM-TES. In these studies, the effects of different fin parameters like fin thickness, shape, length, surface area, position and fin numbers on the heat transfer rate of the LHS device are studied.

### ***Triplex-tube with or without fin***

A few researchers like Al-Abidi *et al.* (2013) came up with a triplex-tube heat exchanger design. In this design, three concentric tubes are employed, in which the PCM is kept in the middle tube, whereas the HTF flows through the innermost and outermost tubes. In this design, the area between the HTF and PCM is very large compared to the shell and tube type PCM-TES design for the same volume of PCM. Thus, using a triplex-tube type PCM-TES device, higher heat transfer rates can be achieved. Some studies used fins or nano-particles with a triplex-tube LHS design to achieve further heat transfer rate increase (Al-Abidi *et al.*, 2013; Abdulateef *et al.*, 2017; Almsater *et al.*, 2017; Mahdi and Nsofor, 2018).

### ***Multitube-in-pipe***

Instead of using a single large tube carrying HTF flow, using multiple smaller tubes is another way to increase the heat transfer rate of PCM-TES devices without compromising

the latent heat storage capacity (Agyenim *et al.*, 2010; Raul *et al.*, 2018; Kousha *et al.*, 2019). Some studies showed that by using multitubes in a shell, the PCM melting time could be reduced by up to 50%. Some researchers combined the multitube-in-pipe design with other LHS designs and came up with better designs like multitube-in-pipe with fins (Gasia *et al.*, 2017; Lakhani *et al.*, 2017; Youssef *et al.*, 2018) and multitube-in-triplex-tube LHS design (Esapour *et al.*, 2016; Esapour *et al.*, 2016).

### ***Multipass coil-in-shell***

The numerical work published by Belusko *et al.* (2015) suggested that instead of using single-pass flows through multitubes, using a counterflow HTF through multipass coils gives superior improvement in heat transfer rates. Therefore, some researchers have built multipass coil-in-shell designs and studied their performances (Castell *et al.*, 2011; Tay *et al.*, 2012). Some studies used fins with multipass coil-in-shell design and obtained even better thermal performance (Rahimi *et al.*, 2014; Seddegh *et al.*, 2017; Koukou *et al.*, 2018).

### ***Plate/Modular***

Some researchers have developed compact PCM-TES devices in which PCM is enclosed in several small rectangular modules and HTF flows around the boundary of these modules (Campos-Celador *et al.*, 2014; Lissner *et al.*, 2016; Liu *et al.*, 2018). Mostly this type of PCM-TES design is used for applications with air as a HTF. These modular systems are very convenient to install and can be easily resized to meet the application storage demand by changing the number of modules in the system (Kim *et al.*, 2010).

### ***Packed bed system***

Packed bed thermal storage is another interesting design of PCM-TES devices. In this design, PCM is encapsulated into small spheres and these spheres are closely packed inside a container (Izquierdo-Barrientos *et al.*, 2016). The HTF flows through the container and travels through the gaps between these spheres. This design of PCM-TES device can be used with both liquid and gaseous type of HTF. The ratio of surface area between PCM and HTF to the volume of PCM is very high in this design, which gives high heat transfer rates during charging and discharging (Delgado *et al.*, 2012; Pakrouh *et al.*, 2017). It was observed that the size of PCM capsules used in this type of device is a very important parameter, which affects the heat transfer rates and efficiency of the PCM-TES (Nallusamy *et al.*, 2007).

#### **1.3.4 Methods used to enhance the heat transfer rate of PCM-TES device**

Some applications demand high heat transfer rates for their smooth operations. Therefore, in such cases, there is a need to enhance the heat transfer rates inside the PCM-TES devices. The following presents four ways used to enhance the heat transfer rates in PCM-TES devices:

1. Adding nanoparticles into the PCM
2. Use of metal foam inside the PCM
3. Adding fins to the HTF carrying tube
4. Use of multitubes and compact coils in the LHS

These methods are described as follows.



### ***1. Adding nanoparticles into the PCM***

In this method, the thermal conductivity of the PCM is increased by dispersing highly conductive nanoparticles (metal oxide powder and carbon nanoparticles of different shapes and sizes) into it (Parameshwaran *et al.*, 2013). The resulting increased thermal conductivity of the PCM improves the heat transfer rate in the PCM-TES device. However, there are some drawbacks to this method. For example, metal-metal oxide powders are vulnerable to corrosion and chemical attack. Also, there is a limit up to which the thermal conductivity of the PCM can be increased using this method. Adding excessive nanoparticles form small clusters of nanoparticles that get separated from the PCM. This reduces effective thermal conductivity, latent heat of fusion and increases the viscosity of the molten PCM composite (Parameshwaran *et al.*, 2013; Kibria *et al.*, 2015). Besides, the higher the concentration of nanoparticles, the lower the resulting latent heat capacity of PCM composites (Fan *et al.*, 2013). Moreover, preparing nanoparticles with controlled size involves complicated processes. Also, to disperse them uniformly into the PCM without segregation requires sophisticated techniques, which makes the entire system expensive (He *et al.*, 2019). Besides, some studies comparing different methods used for heat transfer enhancement in the PCM-TES showed that this method does not appear to work as advertised (Groulx, 2015; Agyenim, 2016).

### ***2. Use of metal foam/mesh inside the PCM***

Some researchers came up with a technique of using highly conductive metal foam/mesh inside the PCM to increase the thermal performance of the LHS systems. The metal foams have low bulk density, high porosity and high thermal conductivity. Due to these properties, they are used to increase the spread of thermal energy within the PCM, which

enhances the heat transfer rate of LHS systems. Many studies have shown improvement of the thermal performance of the LHS by embedding PCM into the metal foam (Xiao *et al.*, 2013; Huang *et al.*, 2017; Qureshi *et al.*, 2018).

Various parameters of metal foams such as porosity, pore density and pore size significantly affect the amount of achieved heat transfer enhancement in the PCM-TES (Zhao *et al.*, 2010; Li *et al.*, 2012; Wang *et al.*, 2016; Jin *et al.*, 2017). However, synthesizing metal foams of any specific pore density, porosity and pore size is a very difficult process. Moreover, to insert PCM uniformly into the metal foams requires a unique impregnation technique, which increases the manufacturing cost of these new LHS systems (Xiao *et al.*, 2013).

### ***3. Adding fins to the HTF carrying tube***

Increasing the heat transfer area between the HTF and PCM by adding fins is another excellent way to improve the heat transfer rate of PCM-TES devices. Unlike metal foams, fins are easy to fabricate. Besides, in contrast to the nanoparticle addition method, adding fins neither increases the viscosity nor reduces the latent heat capacity and the specific heat values of the PCM inside the LHS system. Moreover, the work of researchers like Mahdi and Nsofor (2018) showed that for two identical LHS systems, one containing fins and the other containing nanoparticles of equal volume, the system containing fins displayed much better thermal enhancement. Due to all these reasons, the fin addition method is a very attractive solution to increase the thermal response of PCM-TES devices (Abdulateef *et al.*, 2018).

Numerous studies have been conducted to explore the effects of different fin shapes and geometries on the heat transfer rate of the LHS system. Fin geometries like longitudinal/rectangular, circular, annular, tree-shape and pin are used in LHS systems and extensively studied (Ermis *et al.*, 2007; Baby and Balaji, 2012; Jung and Boo, 2014; Rathod and Banerjee, 2015).

With increasing fin numbers inside the LHS device, the heat transfer area between the PCM and HTF increases. However, it does not always enhance the heat transfer rate of the device (Rabienataj Darzi *et al.*, 2016). The reason is that the resistance offered by fins to the molten PCM currents increases exponentially with higher fin numbers inside the LHS device. It results in a drastic decline in the convective mode of the heat transfer and thus decreases the overall heat transfer rate between the PCM and HTF during the charging process. Therefore, it confirms that adding fins in excess is not only ineffective but also a waste of resources and the energy storage capacity of the LHS device.

In light of the above findings, various studies have been conducted to investigate the best fin configurations and the optimum number of fins that should be used in the LHS system (Kazemi *et al.*, 2018; Mahdi *et al.*, 2018) and came up with novel fin designs (Pizzolato *et al.*, 2017; Youssef *et al.*, 2018). Although these new fin configurations are very efficient and enhance the thermal response of the LHS systems, their usage is not practical as their fabrication process is very time consuming and costly. Even if, in some cases, fin designs are easy to manufacture, welding these fins to the HTF carrying tubes (usually made of copper and aluminum) is a very difficult process that increases the cost of PCM-TES devices drastically.

#### ***4. Use of multitubes and compact coils in the PCM-TES***

Similar to fins, multiple HTF carrying tubes and coils are used to increase the heat transfer surface between PCM and HTF, causing a thermal enhancement in the PCM-TES devices. Contrasting to the nanoparticle dispersion method, it does not exhibit drawbacks like reduction in latent heat value of PCM, phase segregation and increase in the PCM viscosity. Unlike metal foams, the multitubes and multipass coils do not require specialized manufacturing technology for their production. They are easily produced by cutting and bending readily available metal tubes. Contrary to fins, there is hardly any welding involved in their installation inside the PCM-TES devices. It makes them very economical to produce.

Some studies analyzed the effect of tube number on the heat transfer rate of PCM-TES and observed that higher the number of tubes, higher would the heat transfer rate be (Esapour *et al.*, 2016; Esapour *et al.*, 2016). A few studies checked the effect of tubes position on the thermal performance of PCM-TES (Esapour *et al.*, 2016). It is found that placing tubes in the upper half of the container results in the worst performance, whereas placing tubes in the lower half gives superior thermal enhancement. Some researchers used multipass coils in the PCM-TES devices as it is easy to install. In most of these studies, coils were positioned vertically (Castell *et al.*, 2011; Tay *et al.*, 2012; Rahimi *et al.*, 2014; Liu *et al.*, 2018). There are hardly any studies performed with simple horizontal multipass coils in PCM-TES devices. The study of Seddegh *et al.* (2016) reported that LHS devices with horizontally oriented HTF carrying tubes give superior thermal enhancement than that of the vertically oriented ones, particularly during part-load conditions.

### **1.3.5 Methods used to evaluate the performance of PCM-TES**

Selecting the most efficient PCM-TES design and building a right-sized one for a given application is a very challenging task. Because unlike conventional heat exchangers (HX) for which well-established general design rules are available, similar rules for PCM-TES devices are not known. Also, in conventional heat exchangers (fluid-fluid), heat is exchanged between two steady fluid flows, continuously moving in then out of the heat exchanger. On the other hand, in PCM-TES devices, heat is exchanged between a steadily moving HTF flow and a stationary mass of PCM. Due to this, the heat exchange process in the PCM-TES naturally becomes highly transient and much more difficult to characterize (Groulx, 2018).

Several researchers have come up with new methods and tried to develop design guidelines for various designs of PCM-TES devices working under different operating conditions (Castell and Solé, 2015).

For example, Eames and Adref (2002) derived two empirical relationships to determine the instantaneous heat transfer rate during the melting and freezing of water enclosed in a spherical enclosure. These equations are derived for single spherical PCM-TES dipped in a HTF flow. However, in practice, single spherically enclosed PCM is hardly used. Instead, multiple spherical PCM-TES closely packed in a cylinder are used. Hence, these equations have very little practical application. Also, these equations do not take into account the effect of other essential factors like HTF flow rate variation or enclosure material which affect the heat transfer rate of PCM-TES. Lazaro *et al.* (2009) studied a rectangular modular PCM-TES designed for building cooling application and derived a correlation to determine the PCM melting temperature and number of modules necessary to meet the

desired cooling load. These equations are valid for only specific module size used in the study which limits its generalization.

To cover a broad operating range and include the variations in the geometry, some researchers used dimensional analysis and developed dimensionless correlations to characterize PCM-TES devices. For example, Ho and Viskanta (1984) numerically studied a PCM enclosed in a 2D rectangular enclosure with an isothermal bottom surface and an adiabatic top surface and developed an equation for melt-fraction in terms of dimensionless Fourier number and Stefan number. Gau and Viskanta (1986) further extended this study using gallium as a PCM. They introduced the aspect ratio parameter in the melt-fraction equation, which incorporated the size variations of the enclosure geometry. Similarly, other researchers studied 2D enclosures with different boundary conditions and developed dimensionless equations (Bénard *et al.*, 1985; Wolff and Viskanta, 1988; Pal and Joshi, 2001). Researchers like Bastani *et al.* (2014) performed a parametric study on PCM wall-boards used for a building cooling application. They developed a dimensionless correlation to determine the relationship between the complete charging time and the PCM wall-board thickness. The charging time was represented by Fourier number ( $Fo$ ), whereas the Biot number ( $Bi$ ) was used to correlate the thickness of PCM.

Some researchers chose different geometries like cylindrical or spherical enclosing PCM and developed melt-fraction equations for different cylindrical and spherical PCM-HX configurations with constant boundary temperature conditions (Sparrow and Broadbent, 1982; Sparrow and Broadbent, 1983; Ho and Viskanta, 1984; Assis *et al.*, 2007). In these dimensionless correlations, they considered the effect of natural convection by introducing

the Grashof and Rayleigh numbers. During the heat transfer process, the PCM can be at temperatures different than its melting temperature. To consider the effect of initial condition variations, some researchers used dimensionless superheat and subcooling parameters (Bilir and İlken, 2005; Archibold *et al.*, 2014). Some researchers examined the impact of the HTF flow rate by using the Reynolds number (Rathod and Banerjee, 2013). Few researchers considered the effect of shell material (Archibold *et al.*, 2014). Some researches performed studied with different boundary conditions (Rizan *et al.*, 2012).

The above dimensionless correlations, focussing on melting rate and melting time, were derived and tested for specific boundary conditions like constant temperature or constant heat flux boundaries. Although they can be used as tools to help in the overall design of a storage device built using their specific geometries; they are still not complete correlation for the design of a full PCM-HX.

There is a need for general correlations to characterize the complete heat exchanger in PCM-TES. Some researchers are treating PCM-HX by applying the effectiveness-NTU method with some assumptions to characterize their performance. In this approach, the PCM temperature is assumed to be constant during the entire heat transfer process and taken as the melting temperature ( $T_m$ ) to evaluate the effectiveness of the PCM-TES as in Eq. (1.3).

$$\varepsilon = \frac{(T_{in} - T_{out})}{(T_{in} - T_m)} \quad (1.3)$$

where  $T_{in}$  and  $T_{out}$  are the inlet and outlet temperatures of the HTF flowing through the PCM-TES. The average effectiveness value determined over the PCM melting/freezing

process is used to characterize the performance of the PCM-TES at different operating parameters.

Castell *et al.* (2011) studied a coil-in-tank PCM-TES and performed a parametric study on it. They found a relationship between the effectiveness and the ratio of the HTF mass flow rate over the heat transfer surface (defined as a mass flux). Tay *et al.* (2012) extended this work further by considering more cases and derived a single expression for the effectiveness of the PCM-TES. Fang *et al.* (2019) used the effectiveness-NTU method and developed correlations to find the optimum length of a tube-in-tank heat exchanger to get the desired effectiveness. Tay *et al.* (2014) applied the effectiveness-NTU method to characterize the performance of shell-and-tube with fin type PCM-TES devices and developed an equation to determine the average effectiveness of the device. López-Navarro *et al.* (2014) studied a circular coil-in-tank geometry PCM-TES device. They came up with two equations to determine the average effectiveness of the device during melting and solidification. Researchers like Aziz *et al.* (2018) developed a semi-analytical equation based on the NTU method to determine the effectiveness of a spherical PCM-TES and verified it with numerical simulations. Amin *et al.* (2012) experimentally determined a relationship to find the effectiveness of packed bed type PCM-TES. Amin *et al.* (2014) extended this work for packed bed PCM-TES and developed a semi-analytical solution for optimum designing.

Although the NTU method applies to broad operating conditions, there is no single effectiveness equation that can be applied to all heat exchanger geometries operating at any condition. Again, there are some major shortcomings of this method. The NTU method is based on the assumption that all the PCM inside the PCM-TES device remains at a



constant uniform temperature entire process. And often, this temperature is taken as the PCM melting temperature. However, that's not true as all of the PCM inside the PCM-TES device is not at a uniform temperature and its temperature is continuously changing the entire time. Also, in most PCM-TES devices, the PCM is below or above its melting temperature. Thus, the difference in the temperature of HTF is greater than one expected by the NTU method. It leads to effectiveness greater than 1, which is against the definition of effectiveness itself (Groulx, 2018).

Some researchers compared different PCM-TES designs by plotting their various transient characteristics. For example, Agyenim (2016) numerically studied four different types of PCM-HX designs and compared their performance by plotting the average PCM temperature as a function of time. Skaalum and Groulx (2017) compared PCM-HXs with different types of fins by plotting the obtained instantaneous heat transfer rate between the PCM and HTF over the period of the experiments. Some numerical studies compared different configurations of PCM-HXs by measuring their melt-fraction characteristics (Kok, 2020). These comparison methods do not consider the effect of variation in the size, used PCM and used HTF characteristics. Hence, these methods are not adequate to accurately evaluate different systems.

Researchers like Herbinger *et al.* (2019) studied and compared different configurations of vertically finned tube-and-shell PCM-HX by plotting average heat transfer rates obtained during various experiments as a function of the HTF and initial PCM temperature, expressed through Stefan numbers. Medrano *et al.* (2009) prudently compared different types of heat exchangers. In this work, the author came up with a new dimensional parameter, normalized thermal power ( $Q_{therm}$ ), defined as the average power obtained

during the experiment divided by the average temperature difference between the HTF and PCM ( $\Delta T_{avg}$ ), and by the metal contact area between the HTF and PCM ( $A$ ), as shown in Eq. 1.4.

$$Q_{therm} = \frac{Q_{avg}}{\Delta T_{avg} \cdot A} \quad (1.4)$$

This method incorporates the variation in the heat transfer area between the PCM and HTF during the comparison of different PCM-HXs. However, it does not consider the effect of variations in used PCM, chosen HTF mass flow rate and the volume of PCM-HXs. Lazaro *et al.* (2019) improved it further by introducing normalized HTF thermal capacity flow ( $\dot{m}_{HTF,norm}$ ), defined as HTF mass flow rate ( $\dot{m}_{HTF}$ ) multiplied by specific heat ( $C_{p,HTF}$ ) divided by the HTF volume ( $V_{HTF}$ ) of the HTF (shown in Eq. (1.5)) in conjunction with a normalized average power ( $Q_{norm}$ ) term, defined as average power ( $Q_{mean}$ ) per unit volume of the PCM used ( $V$ ) per unit temperature difference between the HTF temperature and PCM melting point ( $\Delta T$ ), as follows:

$$\dot{m}_{HTF,norm} = \frac{\dot{m}_{HTF} \cdot C_{p,HTF}}{V_{HTF}} \quad (1.5)$$

$$Q_{norm} = \frac{Q_{mean}}{V \cdot \Delta T} \quad (1.6)$$

This method takes account the variation of size as well as the HTF parameters. Also, it studied the effect of dimensionless numbers such as Biot number and Stefan number on the proposed parameters. In Chapter 4 of this thesis, this  $Q_{norm}$  parameter is used in

combination with the experiments comparison method proposed by Herbinger *et al.* (2019).

#### **1.4 Research objectives**

As discussed in the literature review, there is a growing body of research conducted to solve the rate problem in PCM-TES. To address this issue, researchers have come up with different designs of PCM-TES devices. The heat transfer processes inside these different PCM-TES designs are transient. Therefore, evaluating the performance of individual designs and comparing them without actually building and testing the devices is an arduous task. Thus, there is a need for general design rules predicting the performance of different designs of PCM-TES devices. Few engineers have tried to characterize the performance of these devices using different methods and developed some design guidelines for specific designs under certain operating conditions. However, these guidelines are often inadequate and there is a need to develop more inclusive design guidelines. To develop such design rules, the transient characteristics of a wide variety of PCM-TES designs at different operating conditions is necessary to obtain.

In pursuit of that goal, the objective of this research work is to collect transient thermal characteristics of coil-and-shell PCM-HX at different operating conditions and geometric configurations and identify key parameters influencing the heat transfer rate of PCM-HX. To achieve this objective, the following sub-objectives were set during this project:

- Design and build different configurations of coil-and-shell PCM-HX.
- Build the required experimental setup by modifying the testing bench in the Lab of Applied Multiphase Thermal Engineering (LAMTE) at Dalhousie University.

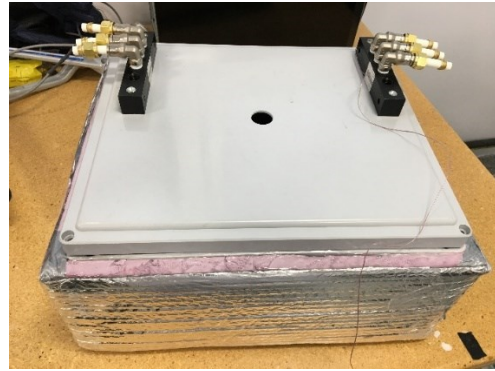
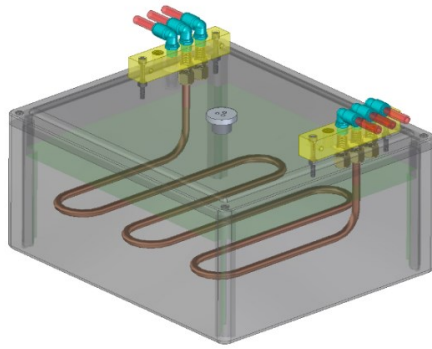
- Perform experimental studies using a set of controlled experiments and identify key parameters affecting the heat transfer rate.
- Perform the analysis and reduce the transient experimental results using various data reduction approaches found in the literature and compare the accuracy of those data reduction approaches.

## **Chapter 2: Experimental design**

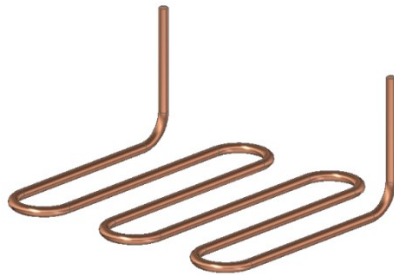
The current chapter first describes the design of the manufactured PCM Heat Exchanger (PCM-HX) and provides details of the constructed experimental setup built for testing this PCM-HX. The latter section of the chapter explains the experimental procedure followed during the charging and discharging experiments. The final section presents the data analysis methods used for the processing of experimental results, including uncertainty analysis.

### **2.1 PCM heat exchanger (PCM-HX)**

Figure 2.1a) shows the constructed horizontal multi-pass coil PCM-HX. A rectangular fibreglass box with dimensions of  $38.75 \times 33.7 \times 17.75 \text{ cm}^3$  was selected for the shell of the PCM-HX. The horizontal multi-pass coils were produced by using soft copper tube coils of 3/8" outer diameter (OD), shown in Fig. 2.1b). The copper coils were first straightened using a tube straightener. These straightened copper tubes were then curved through  $180^\circ$  turns having a radius of curvature 30 mm five times while keeping the distance between the successive curves to 220 mm. To avoid potential leakage from the system, both ends of these multi-pass copper coils were bent at a  $90^\circ$  angle in a plane perpendicular to the previous bending plane; therefore, pointing upward when in the system. Once completed, these coils were attached to connector blocks using compression fittings. The connector block and coil assembly were then attached to the top cover of the PCM-HX with the help of a nuts and bolts arrangement, as shown in Fig 2.1a).



a)



b)

**Figure 2.1: Schematic representation and pictures of: a) PCM-HX and b) Copper coil.**

Twelve kg of dodecanoic acid was poured inside the PCM-HX box. By varying the number of coils inside the box, three different configurations, namely 1-coil, 2-coil and 3-coil setups (shown in Fig. 2.2) were built to examine the effect of the number of coils on the thermal performance of the PCM-HX. These coils were placed symmetrically in each setup so that the distance between the consecutive coils would be twice the distance between the top surface of the PCM and topmost coil. Also, the distance of the bottommost coil from the bottom surface of the PCM-TES device was kept equal to the distance

between the top surface of the PCM and topmost coil in each configuration. In total, five coils were made to make these three setups. The detailed drawings of these coils are included in Appendix A.

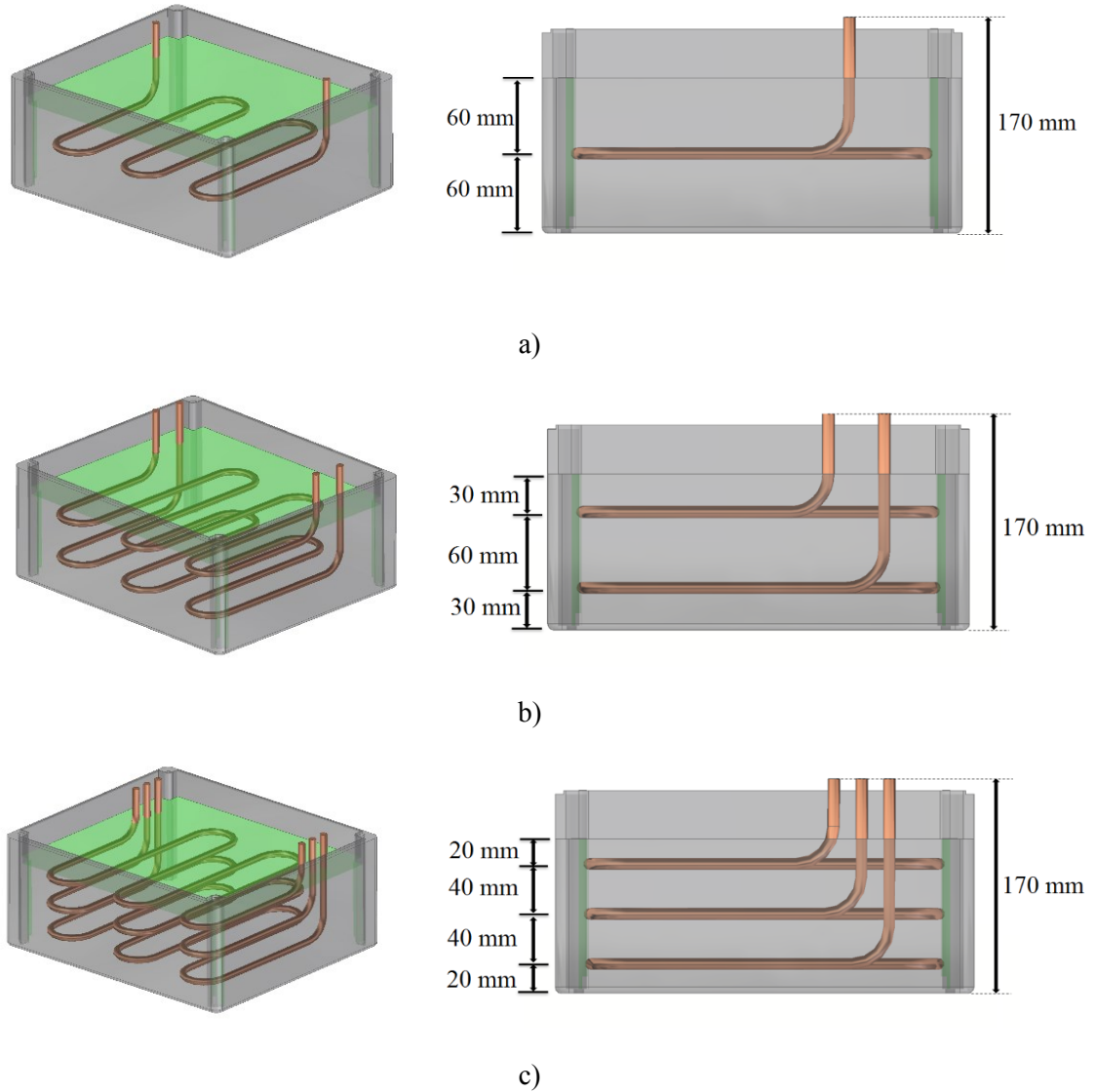


**Figure 2.2: The 2D and 3D schematic representation of a) 1-coil, b) 2-coil and c) 3-coil setups of the PCM-HX.**

Dodecanoic acid ( $\text{CH}_3(\text{CH}_2)_{10}\text{COOH}$ ) is a natural fatty acid derived from coconut oil (Desgrosseilliers *et al.*, 2013). It is non-toxic and therefore very safe for lab usage. It has a high latent heat of fusion (184 kJ/kg), low volume change during phase change (about 6%) and has a melting temperature of approximately 43°C. In addition to the above, it has a relatively low cost and it is readily available in the market. Thus, dodecanoic acid was selected as the PCM for this experimental study. The properties of dodecanoic acid are listed in Table 2.1.

**Table 2.1: Thermophysical properties of dodecanoic acid (Desgrosseilliers *et al.*, 2013).**

Melting temperature ( $T_m$ )	$43.3 \pm 1.5$ °C
Density of solid PCM ( $\rho_s$ )	$930 \pm 20$ kg/m <sup>3</sup>
Density of liquid PCM ( $\rho_l$ )	$873 \pm 20$ kg/m <sup>3</sup>
Specific heat of solid PCM ( $C_{p,s}$ )	$1.95 \pm 0.03$ kJ/kg-K
Specific heat of liquid PCM ( $C_{p,l}$ )	$2.4 \pm 0.2$ kJ/kg-K
Thermal conductivity of solid PCM ( $k_s$ )	$0.15 \pm 0.004$ W/m-K
Thermal conductivity of liquid PCM ( $k_l$ )	$0.143 \pm 0.004$ W/m-K
Latent heat of fusion ( $L$ )	$184 \pm 9$ kJ/kg



## 2.2 Experimental setup

A mobile testing bench equipped with water bath, data acquisition and computer was available in the LAMTE from the previous experimental work of Skaalum and Groulx (2017) and Herlinger *et al.* (2018). This testing bench was modified and used to investigate the performance of the above presented PCM-HX. Figure 2.3 shows a computer aided design (CAD) model of the experimental arrangement as well as a photograph of it. Different charging and discharging experiments were conducted on the PCM-HX using water as heat transfer fluid (HTF). The PCM-HX and all required equipment were mounted on this bench. The data sheets of all equipment are included in the appendix C.

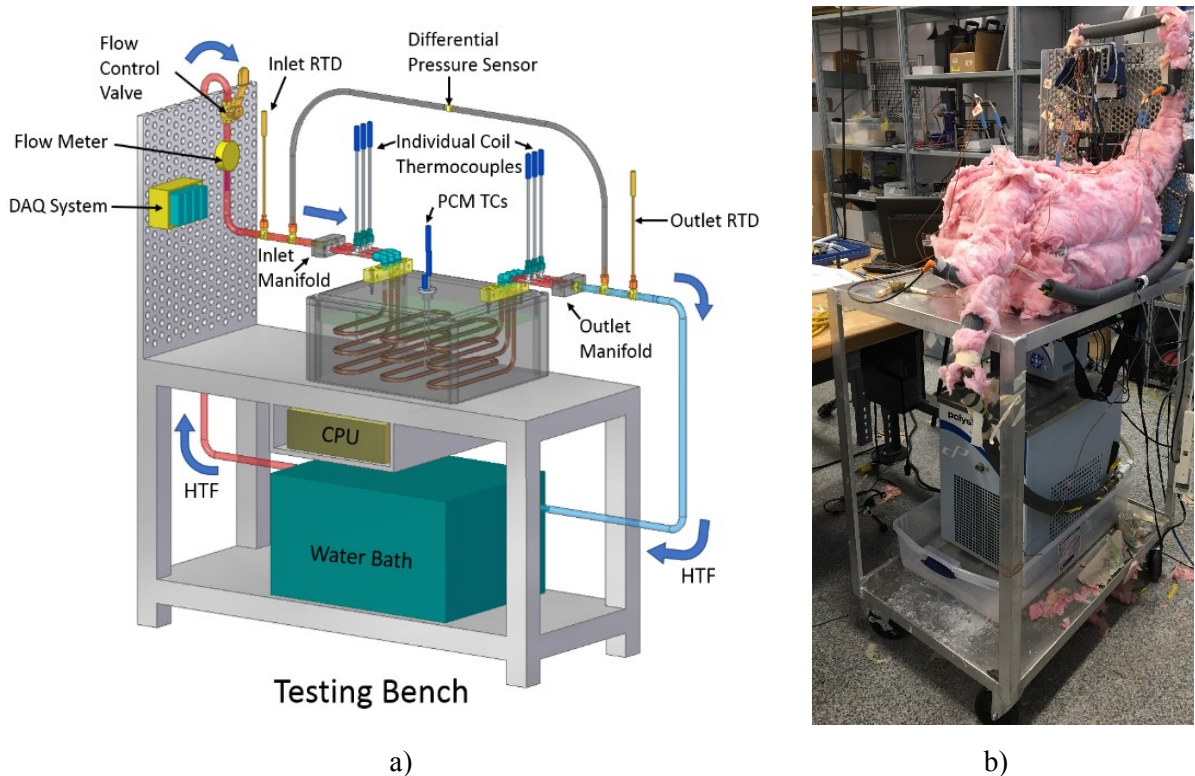


Figure 2.3: a) A CAD model and b) a picture of experimental setup used in this study.

### 2.2.1 Heating and cooling circulating bath

A Cole-Parmer Polystat RK-12122-56 (shown in Fig. 2.4) heating and cooling circulating water bath was used to pass the water through the PCM-HX. This device maintains water inside its tank at a precise temperature using its 800 W cooling capacity (at 20 °C) and 1.2 kW heating capacity. It could supply fluid between -35°C and 150°C with a stability of  $\pm 0.025$  °C. However, in this study, water in the temperature range of 21 to 65°C was utilized. It has a built-in pump which produces a free flow of 21 L/min and a maximum pressure of 11.7 psi.

This water bath was placed under the testing bench, and the PCM-HX was connected between its inlet and outlet port with the necessary piping. Two manifolds were added between the two ends of the PCM HX and the water bath ports, which formed the experimental setup loop. These manifolds divided the HTF flow equally into 1 to 3 individual flows depending on the PCM-HX coil numbers used for a specific experiment.



**Figure 2.4: Picture of the Cole-Parmer Polystat RK-12122-56 heating and cooling circulating water bath.**

Before starting any new experiment, it was necessary to change the water-bath temperature without passing any water flow through the PCM-HX device. However, by the design of water-bath, it was necessary to keep water circulating from its outlet port to the inlet port in order to change the water-bath temperature. Thus, using three ball-valves, a bypass loop parallel to the PCM-HX loop was added, as shown in Fig. 2.5. Figure 2.5a) shows the normal valve positions when the experiments were running, whereas Fig. 2.5b) shows the valve positions when the water bath temperature was changing, and no water was flowing through the PCM-HX.

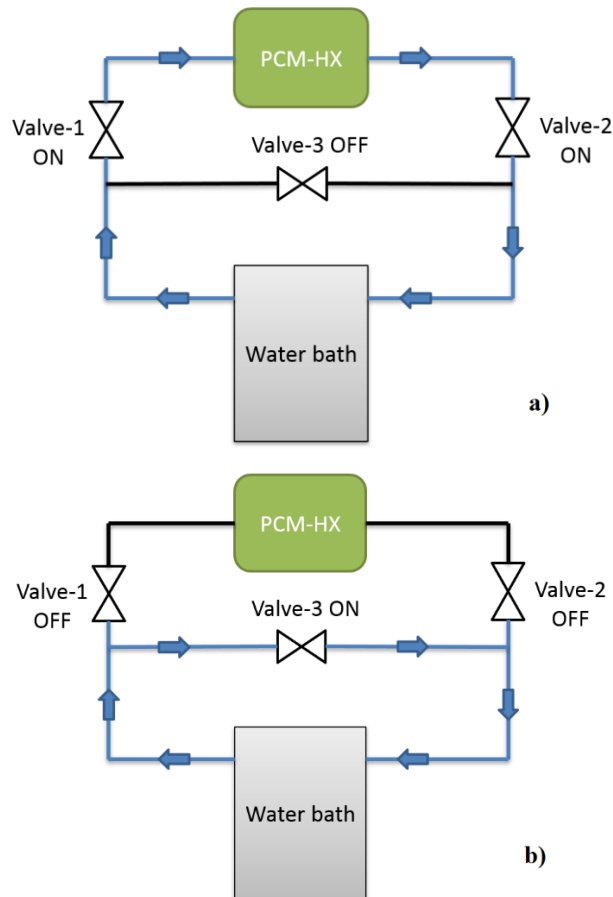


**Figure 2.5: Schematic diagram of water-bath flow circuit a) when experiments were carried out on the PCM-HX and b) when changing the water-bath temperature.**

## 2.2.2 Sensors

### 2.2.2.1 Flow measurement

An Omega FTB 4605 model turbine type flow meter was used to continuously measure the HTF flow rate, shown in Fig. 2.6. It was placed in line with the water flow and positioned in between the outlet port of the water bath and the inlet manifold of the PCM-HX. A manual operated ball valve was also placed in the fluid line next to the flow meter to control the flow rate of the HTF, as shown in Fig. 2.3. During operation, the water flowing through the flow meter forces its turbine to spin. During each turbine revolution, a fixed amount of fluid passes through the loop. The flow meter is equipped with Hall Effect sensor attached to the turbine shaft, which gives a one current pulse output during each revolution. Therefore, by tracking the rate of these generated pulses, the instantaneous volume flow rate of the fluid can be measured.



**Figure 2.6: Picture of the Omega FTB 4605 flow meter**

The flowmeter was connected to an NI 9435 module which counted these pulses and LABVIEW converted it into a volume flow rate by using the manufacturer given conversion factor of 40 pulses/L. Prior to using it in the experimental setup, for verification of this conversion factor, the flow meter was connected to the water bath, and water was discharged through it at a constant temperature of 25 °C for 1 minute. The total pumped volume of water over that minute was then compared to the LABVIEW output

from the flowmeter. This process was repeated five times, and the average conversion factor was calculated and came to 39.96 pulses/L (*i.e.*  $\approx 40$  pulses/L). Thus, the verification process was completed. Also, the flow meter has a manufacturer specified uncertainty of  $\pm 2\%$  of the reading.

### **2.2.2.2 Temperature measurement**

#### **RTD**

Two Omega brand RTD Probe sensors (model number PR-22-3-100-A-1/8-0300-M12) were used to precisely measure the temperature of the HTF entering and exiting the PCM-HX, shown in Fig. 2.7 a). One RTD probe was mounted just before the inlet manifold and the other after the outlet manifold. They were installed in the flow line using tee connectors and compression fittings. These RTD probes are 3" in length and 1/8" in diameter. They contain a Pt-100 RTD element and have an IEC Class-A accuracy of  $\pm 0.28$  °C up to 65°C.

#### **Thermocouples**

To ensure the HTF is flowing through all the coils and monitor the temperature of the water flowing through the individual coils of the PCM-HX, T-type thermocouple probes with 1/8" cladding diameter and length of 6" were installed between each manifold and connector blocks. These thermocouples have an accuracy of  $\pm 0.5$  °C and are shown in Fig. 2.7 b).

To monitor the PCM temperature, three additional T-type thermocouple probes were inserted at the center of the PCM-HX and submerged to three different heights of 0 mm, 60 mm and 110mm from the bottom of the enclosure. These thermocouples were 1/16" in



diameter and 12" long as shown in Fig. 2.7 c). To hold them together and maintain their positions inside the PCM, a nylon holder was 3D printed, shown in Fig. 2.8. This holder had three 1/16" diameter holes at the center in which these thermocouples were inserted and fixed with adhesives. One 25 mm diameter hole was drilled in the top cover of the PCM-HX and the holder was fitted in that hole.



a)



b)



c)

**Figure 2.7: Various temperature sensors used in the experimental setup: a) Omega brand RTD Probe sensor with model number PR-22-3-100-A-1/8-0300-M12, b) T-type thermocouple with 1/8" diameter and 6" length, and c) T-type thermocouple with 1/16" diameter and 12" length.**

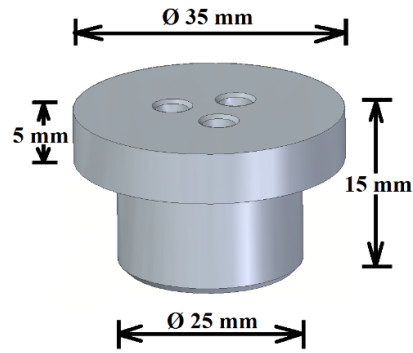


**Figure 2.8: 3D CAD model of the nylon holder.**

It is expected that the PCM at the very bottom of the box, below the exit connector block, would receive the least amount of heat since the HTF will be at its coldest before leaving the system. Therefore, the PCM in this corner would melt/solidify last. Thus, to ensure the completion of charging/discharging experiments, one T-type wire thermocouple was positioned at the bottom corner of the box. When this thermocouple reached the water bath temperature, the experiment was stopped as it signified that all the PCM inside the box had melted (or solidified) and reached to the final temperature.

While assembling the experimental setup, and before usage, all the RTDs and thermocouples used to measure HTF temperatures were calibrated using a FLUKE 7102 Micro-Bath Thermometer Calibrator. This device uses a silicon oil bath and precisely maintains its temperature to a set point. All the sensors were simultaneously immersed in the bath and their deviations from the set temperature were determined. The setpoint of the oil bath was varied from 20 to 70°C with increments of 5°C. Table 2.2 shows the temperature readings obtained from temperature sensors during the calibration process. All the temperature sensors were calibrated using these deviation values into the LABVIEW.

**Table 2.2: Temperature sensor calibration data at different set point bath temperatures.**

Set Point	Inlet RTD	Outlet RTD	T <sub>inlet1</sub>	T <sub>inlet2</sub>	T <sub>inlet3</sub>	T <sub>outlet1</sub>	T <sub>outlet2</sub>	T <sub>outlet3</sub>
<b>(Reading deviations from the set point in °C)</b>								
20	0.03	0.02	-0.01	0.01	-0.12	0.07	0.04	0.10
25	0.04	0.03	0.01	0.02	-0.10	0.09	0.06	0.12
30	0.06	0.04	0.03	0.05	-0.08	0.11	0.08	0.14
35	0.06	0.04	0.06	0.08	-0.04	0.14	0.11	0.16
40	0.08	0.07	0.03	0.06	-0.08	0.12	0.09	0.14
45	0.08	0.07	0.10	0.12	0.00	0.20	0.16	0.22
50	0.10	0.08	0.10	0.12	0.00	0.19	0.15	0.20
55	0.10	0.08	0.11	0.14	0.01	0.21	0.16	0.23
60	0.11	0.10	0.12	0.15	0.03	0.21	0.18	0.22
65	0.11	0.11	0.09	0.13	0.00	0.20	0.17	0.22

The temperature control sensor of the FLUKE 7102 micro-bath had an accuracy of  $\pm 0.25^{\circ}\text{C}$ ; therefore, the actual oil bath set temperature would be within  $\pm 0.25^{\circ}\text{C}$  from the set point. Also, the micro-bath had a stability of  $\pm 0.02^{\circ}\text{C}$ . Therefore, during the equilibrium water-bath condition, its temperature could fluctuate within this  $\pm 0.02^{\circ}\text{C}$  temperature range. In addition, the micro-bath had a uniformity of  $\pm 0.02^{\circ}\text{C}$ , which implies that the temperature difference between any two points inside the oil bath was maintained within this  $\pm 0.02^{\circ}\text{C}$  temperature range. Thus, when the temperature sensor was calibrated in LABVIEW, it had an inherent accuracy of  $\pm 0.29^{\circ}\text{C}$  (i.e. equal to  $0.25^{\circ}\text{C} + 0.02^{\circ}\text{C} + 0.02^{\circ}\text{C}$ ). However, in this study, the difference in the inlet and outlet RTD temperatures (i.e.  $(T_f - T_i)$ ) was of interest for calculating the instantaneous rate of heat transfer between the HTF and PCM. During the calibration process, all the temperature sensors (2



RTD, 3 inlet thermocouples and 3 outlet thermocouples) were dipped simultaneously in the oil bath. Therefore, the uncertainty caused by the oil bath accuracy and stability did not contribute to the uncertainty of temperature difference in the RTD readings and only the oil bath uniformity played a role in the uncertainty of the temperature difference between the RTDs (or any two sensors). Therefore, the measured difference between the inlet and outlet RTD temperatures (*i.e.*  $(T_f - T_i)$ ) had an uncertainty of  $\pm 0.02$  °C. The remaining four thermocouples embedded in the PCM during the study were not calibrated. Thus, they had an accuracy of  $\pm 0.5$ °C as provided by the manufacturer.

### **2.2.2.3 Pressure measurement**

The operating cost of the LHS system would in part be related to the power required to move the HTF through the PCM-HX. Therefore, to measure the pumping power required for a given PCM-HX, an Omega brand PX26-015DV differential pressure transducer was used in the setup, shown in Fig. 2.9. Two tubes branched off the main water line just before the inlet manifold and right after the outlet manifold of the PCM-HX and connected to the two input ports of the pressure transducer. According to the relative pressure difference in these tubes, the diaphragm in the pressure transducer deflects and generates an electric signal. This signal was converted into appropriate pressure value in Pa using the manufacturer given relation of 100 mV sensor output equivalent to a 15-psi pressure difference into LABVIEW. This pressure sensor has an accuracy of  $\pm 1\%$  of its full-scale reading, *i.e.*,  $\pm 0.15$  psi. Before using this sensor, a known differential pressure was applied at the two ports of the pressure sensor using a water column and the results reading shown in LABVIEW compared to the expected theoretical result; this served as confirmation of the sensor accuracy.

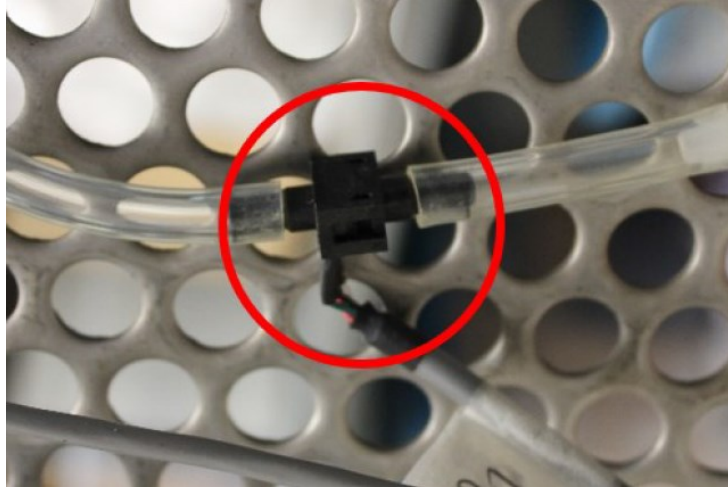


**Figure 2.9: Picture of an Omega brand PX26-015DV differential pressure transducer.**

### **2.2.3 Data acquisition system**

A National Instruments data acquisition system (NI-cDAQ 9174 chassis) was employed to process and record the measurements provided by the sensors into the computer. The NI 9213 module was used to measure the readings provided by all the thermocouples. RTDs were connected to the NI 9217 module. The NI 9435 module was chosen to measure the output of the turbine flow meter. The NI 9237 module was used to measure the signal of the pressure sensor since it has simultaneous bridge circuits with shunt calibration and remote sense features which makes it very precise for strain measurements.

All these modules were mounted on the NI-cDAQ 9174 chassis, shown in Fig. 2.10. It communicated all the measurements to the computer through LABVIEW. LABVIEW provided real-time display of data and allowed the processing of individual signals received from the NI-cDAQ 9174 chassis. For example, recorded calibration of the temperature sensors, converting the flow meter pulse count into the flow rate and conversion of pressure from the pressure sensors signals.



**Figure 2.10: Picture of the NI-cDAQ 9174 chassis with the NI9213, NI9217, NI9435 and NI9237 modules mounted on it.**

## **2.3 Experimental procedure**

The following procedure was adopted while conducting the charging and discharging experiments on the PCM-HX:

- Bring all the PCM inside the PCM-HX to a uniform initial temperature by passing water maintained at that temperature through the copper coils of the PCM-HX.
- Once all the PCM reached the initial temperature, turn off the water supply through the coils by closing the manual ball valves and open the bypass line.
- Change the water bath temperature from the initial temperature to the desired final temperature.
- Once the bath temperature reached the desired HTF temperature, shut off the bypass loop and turn on the main valve to start the flow of the water at the final temperature through the PCM-HX. Using the manual ball valve, adjust the desired flow rate.
- At the same time, once the water starts to flow through the circuit, turn on LABVIEW to begin recording the sensor readings at an interval of 4 seconds into a .csv file.

- Through the experiment, the PCM temperature will start to change from initial temperature to the final temperature. This change was tracked by observing the temperature readings of the thermocouples dipped inside the PCM.
- Once these dipped thermocouples reached the final temperature (*i.e.* HTF bath temperature), stop the experiment by turning off LABVIEW and shutting down the bath circulation pump.

The above procedure was repeated for all the charging and discharging experiments. Figure 2.11 presents a visual representation of the list of experiments performed in this study when it comes to temperature ranges used. The red and blue arrows represent the PCM charging and discharging experiments respectively, with the arrows showing the initial PCM temperature, with the change in the PCM temperature until the final value (the HTF temperature). All of these experiments were performed on 2-coil and 3-coil setups. As 1-coil experiments took longer to fully perform (more than 60 hours for their completion), only a few of these experiments were performed. During all these experiments, the HTF flow rate was maintained at 3.3 L/min.

These experiments are defined by two dimensionless numbers, namely the total Stefan number ( $Ste_t$ ) and the melting temperature Stefan number ( $Ste_m$ ). The total Stefan number takes into account the entire range of sensible energy to be exchanged in the process:

$$Ste_t = \frac{C_{p,PCM}|(T_R - T_i)|}{L} \quad (2.1)$$

where  $T_R$ ,  $T_i$  are the HTF and initial PCM temperatures.  $C_{p,PCM}$  is taken as the average between the solid and liquid phase specific heat values of PCM from Table 2.1.

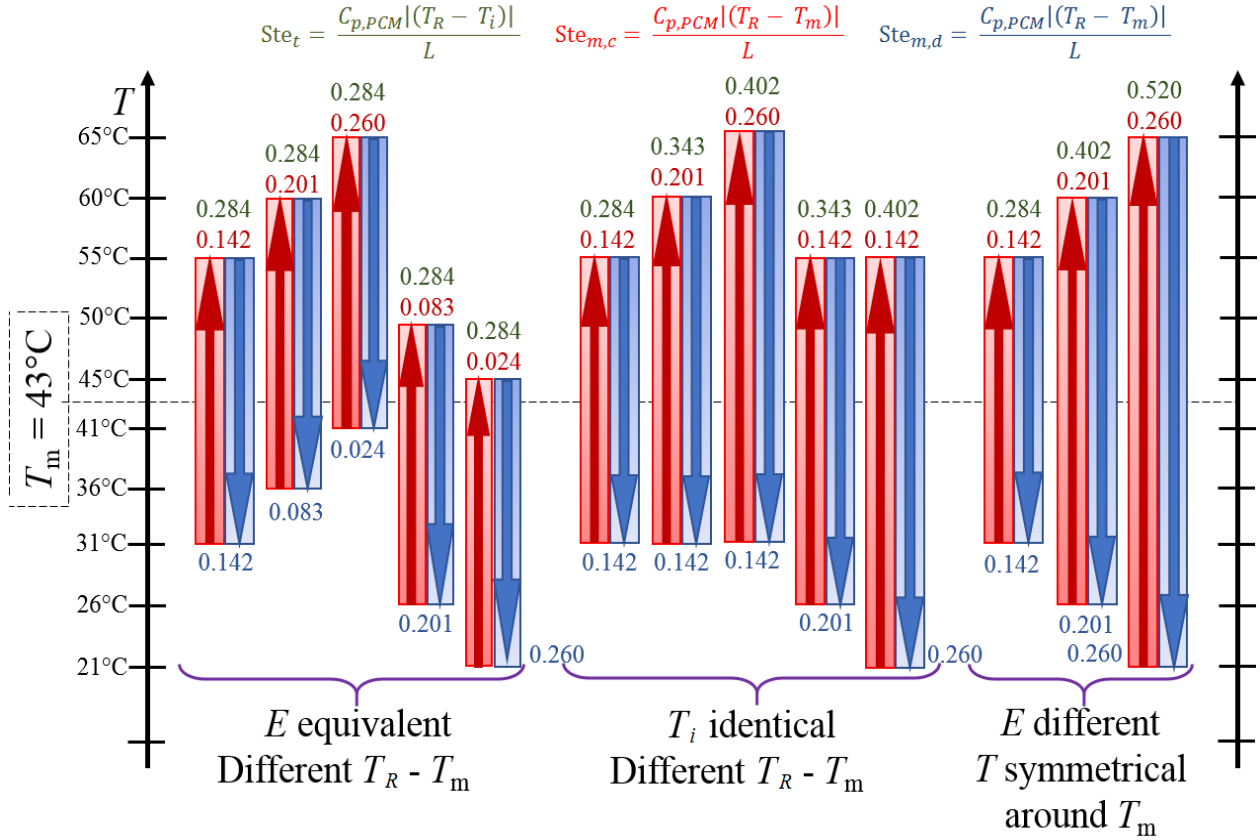


**Figure 2.11: Schematic representation of the temperature intervals used for all the experiments performed in this study.**

On the other hand, the melting Stefan number considers the temperature difference between the driving HTF temperature and melting temperature of the PCM; this temperature difference could be seen as the driving force behind the overall heat transfer in the PCM-HX (this study will in part look into the validity of this statement). It is defined as:

$$\text{Ste}_m = \frac{C_{p,PCM}|(T_R - T_m)|}{L} \quad (2.2)$$

where  $T_m$  is the PCM melting temperature. The concept of the melting Ste-number applies equally to solidification experiments; therefore, the name will not be changed between charging and discharging experiments. However, an addition to the nomenclature will be

introduced to distinguish between the charging and discharging experiments: the melting Ste-number calculated for the charging experiment will be represented as  $Ste_{m,c}$  whereas for the discharging experiment it will be  $Ste_{m,d}$ .

The flexible and firm tubings used in the flow circuit had a maximum operating temperature limit of 80 °C. Therefore, as a precaution, 65 °C was selected as a maximum temperature in the study. The average room temperature of 21 °C was chosen as a minimum temperature for the study. It also turns out that the melting temperature of the PCM, 43 °C, falls directly between those two extremes.

The controlled temperature ranges selected for the experiments fall within one of three groups: a) equivalent energy ( $E$ ) experiments, b) same initial temperature ( $T_i$ ) experiments and c) symmetrical temperatures around  $T_m$  experiments. For the equivalent  $E$  experiments, each had an identical  $Ste_t$  but different  $Ste_m$  values; in other words, the same amount of energy needed to be transferred in all those cases, but the temperature difference between the HTF and the PCM melting point differed for each. For the same initial temperature ( $T_i$ ) experiments, each had different  $Ste_t$  and  $Ste_m$  values so the impact/importance of the initial temperature could be looked at. Finally, for symmetrical temperatures around  $T_m$  experiments,  $|(T_m - T_i)| = |(T_R - T_m)|$  and those experiments are good complements to the first two sets.

Table 2.3 presents the lists of all the experiments performed following the representation of Fig. 2.11. All these experiments were performed on 2-coil and 3-coil setups, whereas only the experiments shown with red were performed on the 1-coil setup. The experiments highlighted in yellow falls under all three types of experiments.

**Table 2.3: List of performed experiments**

Type of experiments	Melting experiments		Solidification experiments	
	Initial PCM temperature in °C	Final PCM temperature in °C	Initial PCM temperature in °C	Final PCM temperature in °C
a) Equivalent energy ( $E$ )	21	45	45	21
	26	50	50	26
	31	55	55	31
	36	60	60	36
	41	65	65	41
b) Same initial temperature ( $T_i$ )	31	55	55	31
	31	60	55	26
	31	65	55	21
c) Symmetrical temperatures around $T_m$	21	65	65	21
	26	60	60	26
	31	55	55	31

Similar to the HTF temperature, the flow rate is also an essential factor which affects the heat transfer rate. Flow rate variation changes the HTF residence time inside the copper coils as well as changes the thermal resistance between the HTF and the coil, through a modification of the internal forced convection coefficient in the pipes. Thus, it is necessary to investigate the effect of flow rate variation on the heat transfer rate. The 3-coil setup has a high heat transfer rate and requires less time for experiment completion due to its high heat transfer area between the PCM and HTF. Thus, it was chosen to test the effect of flow rate variation on the heat transfer rate. Therefore, another set of experiments with the HTF flow rate of 6.3 LPM using the same temperature ranges as presented previously were

conducted on the 3-coil setup and compared with the corresponding results from the 3-coil setup with a 3.3 LPM flow rate.

## 2.4 Data analysis methodology

### 2.4.1 Heat transfer rate

During the experiments, heat is transferred between the HTF and the PCM. As the whole system is insulated, the heat gain by one must be equal to the heat lost by the other during the heat transfer process. Therefore, the heat transferred to the PCM can be obtained by calculating the sensible heat change of the HTF, *i.e.*, water. Thus, the instantaneous heat transfer rate between PCM and water can be calculated by using Eq. (2.3).

$$Q(t) = \dot{m}_{HTF} C_{p,HTF} (T_{in} - T_{out}) \quad (2.3)$$

where  $Q(t)$  is the instantaneous power stored or extracted from the PCM-HX.  $\dot{m}_{HTF}$  is the instantaneous mass flow rate of the water, which is equal to the density times the volumetric flow rate of the water through the system,  $C_{p,HTF}$  is the specific heat of water and  $T_{in}$ ,  $T_{out}$  are the water temperatures measured at the inlet and outlet respectively by the RTDs.

### 2.4.2 Uncertainty analysis

The RTDs and flowmeters have some inherent uncertainties in their measurements. The difference between the RTD temperatures (*i.e.*  $(T_{in} - T_{out})$ ) has an uncertainty of  $\pm 0.02$  °C as discussed in Section 2.2. Also, as mentioned earlier, the flow meter has a manufacturer specified uncertainty of  $\pm 2\%$  of the reading. Using these values, the total uncertainty in the calculated heat transfer rate ( $dQ$ ) can be obtained by using the multiplication with multiple uncertainties rule. It is given by:



$$d(Q) = d(\dot{m} C_{p,HTF} (T_{in} - T_{out}))$$

$$dQ = C_{p,HTF} \cdot \left[ \sqrt{\{(T_{in} - T_{out}) \cdot d\dot{m}\}^2 + \{\dot{m} \cdot d(T_{in} - T_{out})\}^2} \right] \quad (2.4)$$

$$dQ = C_{p,HTF} \cdot \left[ \sqrt{\{(T_{in} - T_{out}) \cdot (0.02 \dot{m})\}^2 + \{\dot{m} \cdot (0.02)\}^2} \right]$$

Using this uncertainty, the upper and lower limit of the possible actual heat transfer rate is calculated.

### 2.4.3 Accounting for the heat loss/gain by the PCM-HX

In practice, it is impossible to perfectly insulate a system. Therefore, during the experiments, the PCM-HX gains or loses some of its stored energy to the environment, which must be taken into account to calculate the net heat stored/extracted from the PCM-HX. The net heat loss or gain by the system can be easily determined by the continuous power required at the end of each experiment to keep the system in its final state. This power requirement should theoretically be zero if the system was perfectly insulated.

Therefore, the net power stored/extracted in the PCM-HX was calculated by simply subtracting/adding the heat loss/gain from the experimentally calculated power, as shown by Eqs. (2.5) and (2.6).

$$Q_{actual} = |Q_{calculated}| - |Q_{loss}|, \text{ for charging experiments} \quad (2.5)$$

$$Q_{actual} = |Q_{calculated}| + |Q_{gain}|, \text{ for discharging experiments} \quad (2.6)$$

These experimentally obtained  $Q_{loss}$  and  $Q_{gain}$  values were verified mathematically and are presented in Appendix B.

By adding and subtracting  $dQ$  from the  $Q_{actual}$  value, the upper and lower limit of uncertainty in the actual heat transfer rate was calculated respectively, as shown by Eqs. (2.7) and (2.8).

$$Q_{actual,max} = Q_{actual} + dQ \quad (2.7)$$

$$Q_{actual,min} = Q_{actual} - dQ \quad (2.8)$$

#### 2.4.4 Total energy transfer

The total energy transferred ( $E$ ) between the HTF and PCM is calculated by integrating the instantaneous heat transfer rate over the duration of the experiment:

$$E = \int_{start\ time}^{end\ time} Q_{actual}(t) dt \quad (2.9)$$

The upper and lower limit of the uncertainty (*i.e.*  $E_{max}$  and  $E_{min}$ ) in the total energy transferred ( $E$ ) between the HTF and PCM were calculated by integrating the  $Q_{actual,max}$  and  $Q_{actual,min}$  over the duration of the experiment, as shown by Eqs. (2.10) and (2.11).

$$E_{max} = \int_{start\ time}^{end\ time} Q_{actual,max}(t) dt \quad (2.10)$$

$$E_{min} = \int_{start\ time}^{end\ time} Q_{actual,min}(t) dt \quad (2.11)$$

Another way of calculating the total energy transfer is the use of temperature changes of the PCM. Assuming all the PCM starts uniformly at one temperature and reaches uniformly the final temperature, the total theoretical energy change of the PCM is calculated, as in Eq. (2.12).

$$\begin{aligned}
 E_{pcm} &= E_{latent} + E_{sensible} & (2.12) \\
 &= m_{pcm}L + mC_{p,s}|(T_m - T_{i,pcm})| \\
 &\quad + mC_{p,l}|(T_{f,pcm} - T_m)|
 \end{aligned}$$

where  $E_{pcm}$  is the change in the PCM energy,  $E_{latent}$  and  $E_{sensible}$  are the changes in the latent and sensible energy of the stored PCM,  $m_{pcm}$  is the mass and  $L$  is the latent heat of the PCM,  $C_{p,s}$  and  $C_{p,l}$  are the specific heat of the solid and liquid PCM, and  $T_{i,pcm}$  and  $T_{f,pcm}$  are the initial and final temperature of the PCM.

By using the above described experimental arrangement (Section 2.2), instantaneous temperatures and flow rate of the HTF flowing through the PCM-HX (Section 2.1) were measured during various experiments (Section 2.3). This measured raw data, obtained from the flow and temperature sensors, were processed using the data analysis method (Section 2.4), and the instantaneous heat transfer rate between the PCM-HX and HTF was obtained for individual experiments.

## Chapter 3: Results and discussion

This chapter presents the results obtained during the various charging and discharging experiments performed on the 1-coil, 2 coil and 3-coil setups. By comparing these results with each other, the effect of different operating parameters (initial PCM temperature, number of coils used, HTF temperature and flow rate) on the heat transfer rate of the PCM-HX is analyzed.

### 3.1 Temperature, energy and pressure results

Figure 3.1 show the typical temperature profiles recorded by the two RTD sensors positioned at the HTF inlet and outlet, the three T-type thermocouples placed at different heights within the PCM-TES device and one T-type thermocouple placed outside the PCM-TES device measuring ambient temperature during the charging and discharging experiments.

Figure 3.1a) shows the temperature data collected during the 21 to 65°C charging experiment (initial PCM temperature of 21°C and HTF temperature of 65°C) performed on the 3-coil setup with a HTF flow rate of 3.3 L/min. From the inlet and outlet temperature curves, it can be seen that the temperature difference between the inlet and outlet RTD sensors ( $\Delta T$ ) increases during the initial period (approximately the first hour) and reaches a maximum value and then decreases gradually. This phenomenon can be explained by the increase in the heat transfer rate in the initial period due to the setting up of natural convection currents inside the molten PCM. Once the peak  $\Delta T$  is reached, it starts declining as the average PCM temperature inside the PCM-TES device increases leading to gradually decreasing heat transfer rates between HTF and PCM.

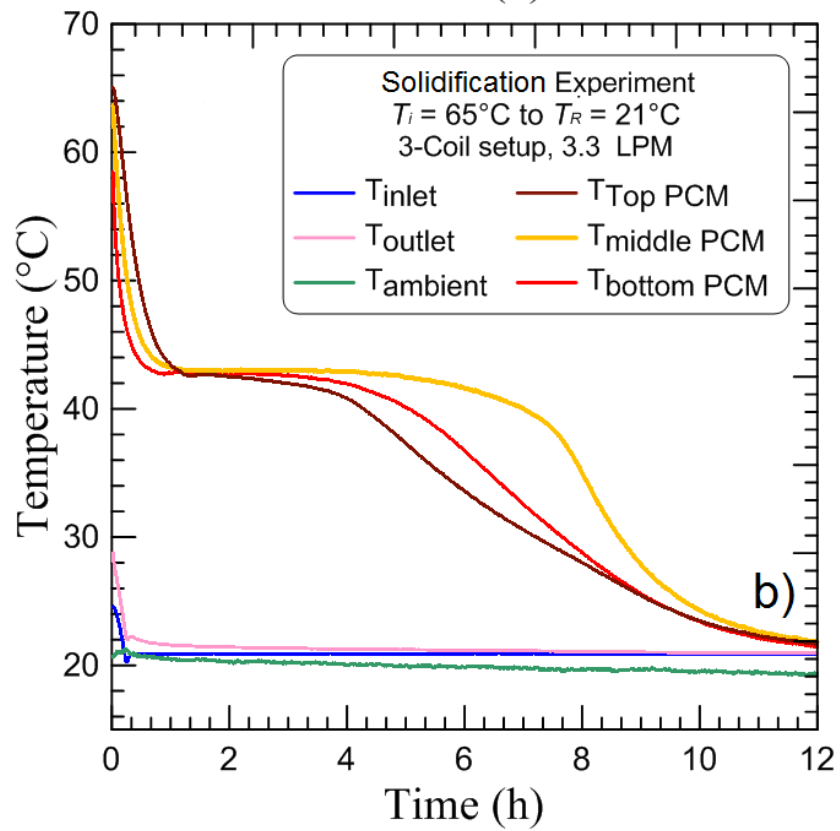
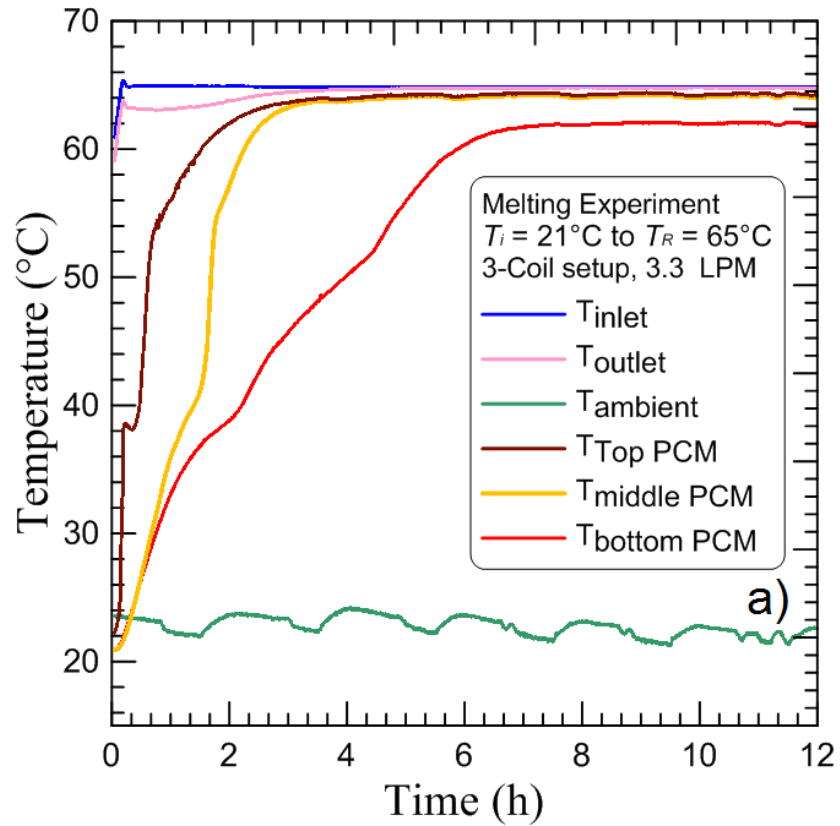


Figure 3.1: Typical trend of raw data obtained from different temperature sensors during a) charging and b) discharging processes.

In the charging experiment, once the hot HTF starts flowing through the coils of the PCM-TES device, the temperature recorded by the three thermocouples embedded into the PCM starts increasing. It rapidly reaches the melting point of the PCM. At this point, further heat addition causes a phase transformation in the PCM without changing its temperature. Thus, a small flattening of the temperature increase has occurred in these thermocouple profiles around 43°C. Once the phase change process is completed, the PCM temperature again starts increasing. However, at this point, the driving temperature difference between the PCM and HTF is reduced significantly, and further heat addition process takes place at a slower pace until finally the PCM temperature reaches the HTF temperature. However, in Fig. 3.1a), it can be observed that the bottom thermocouple temperature never reached to HTF temperature. It is in part due to the very slow heat transfer process at the end, so the bottom part of the PCM extremely slowly receives additional energy, this shows as a nearly constant temperature below the HTF temperature. Also, partly due to the effect of thermal stratification inside the molten PCM, the bottom PCM never reached the HTF temperature.

Similarly, Fig. 3.1b) shows the temperature data collected during the 65 to 21°C discharging experiment (initial PCM temperature at 65°C and HTF temperature of 21°C) performed on the 3-coil setup at 3.3 L/min. Here also, once the cold HTF starts flowing through the coils of the PCM-TES device, the temperature recorded by the three thermocouples embedded into the PCM starts decreasing. The sensible heat from the PCM gets quickly removed and thus the temperature of the thermocouples falls sharply initially to reach the melting point of the PCM. The phase transformation of the PCM takes place from this point onwards without changing the PCM temperature. This forms a plateau in

the temperature profile. Once the phase change process is completed, the PCM temperature again starts falling and eventually reaches to HTF temperature. Based on the thermal resistance between the HTF surface and the PCM near these three thermocouples, their temperature profiles vary from each other.

Figure 3.2 shows the comparison of temperature profiles obtained for 1-coil, 2-coil and 3-coil setups. Figure 3.2a) compares the temperature profiles recorded during the 21 to 65°C charging experiments performed on 1-coil, 2-coil and 3-coil setups at 3.3 L/min. Figure 3.2b) compares the temperature data recorded during the 65 to 21°C discharging experiments performed on 1-coil, 2-coil and 3-coil setups at 3.3 L/min.

From these figures, it can be observed that for the same charging and discharging experiments performed on different coil setups, different temperature profiles are recorded. The temperature profiles of different PCM embedded thermocouples have a higher rate of change of temperature with the increasing number of coils. This is easily explained by an increase in exchange surface area and by the fact that with more coils, heat is brought closer to the bottom of the PCM enclosure. It increases the amount of melting near the bottom of the enclosure and heat is more uniformly spread into the PCM.

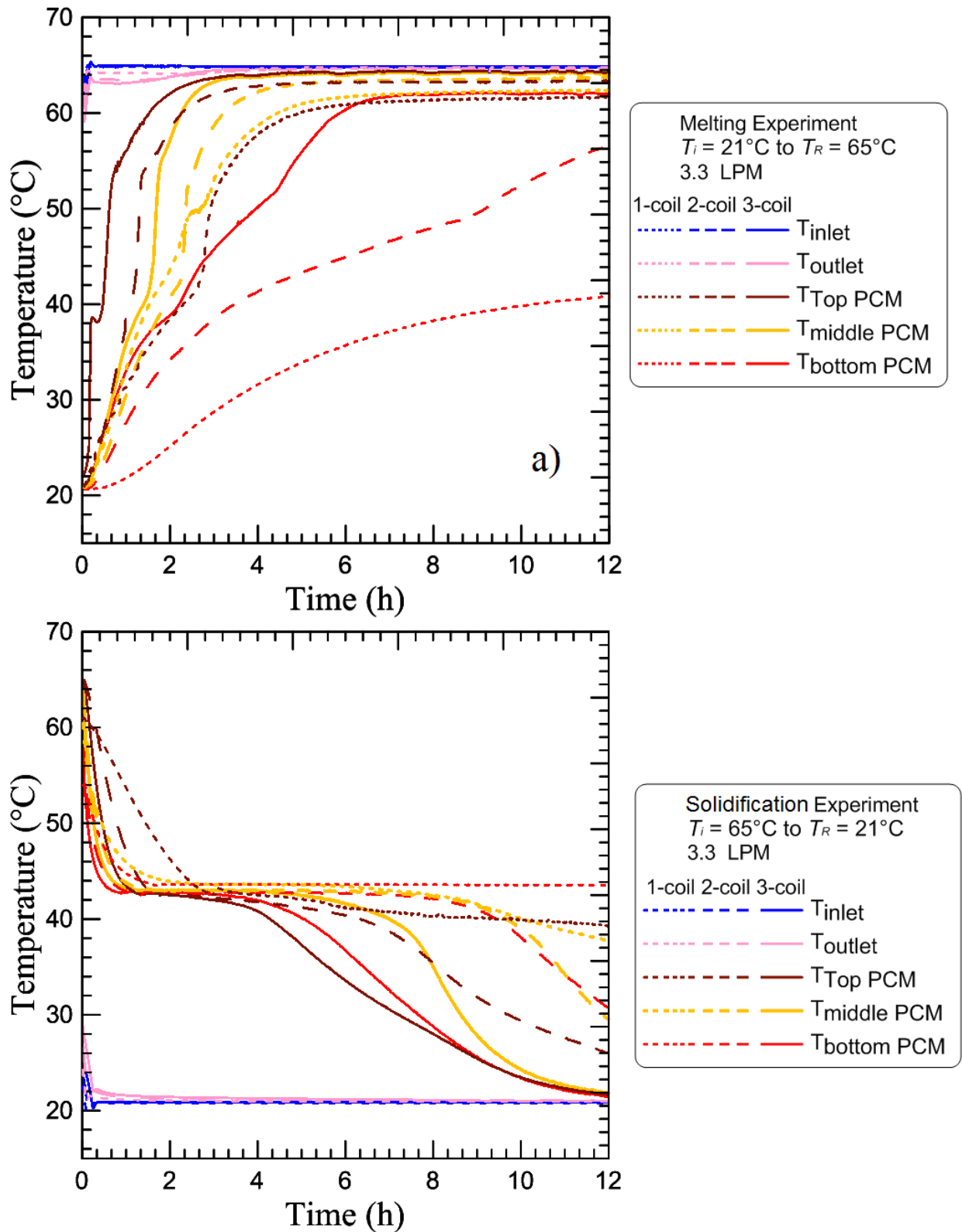


Figure 3.2: Typical trend of raw data obtained from different temperature sensors during the a) charging and b) discharging processes performed on 1-coil, 2-coil and 3-coil setup.



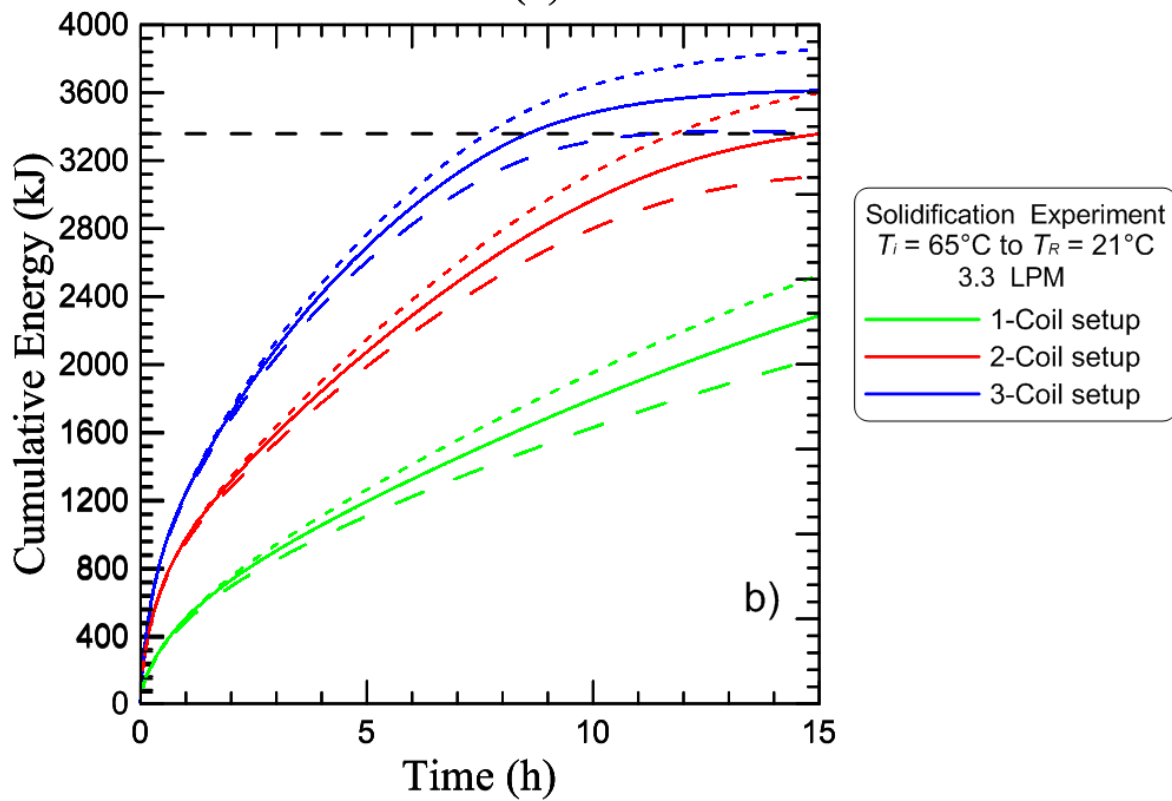
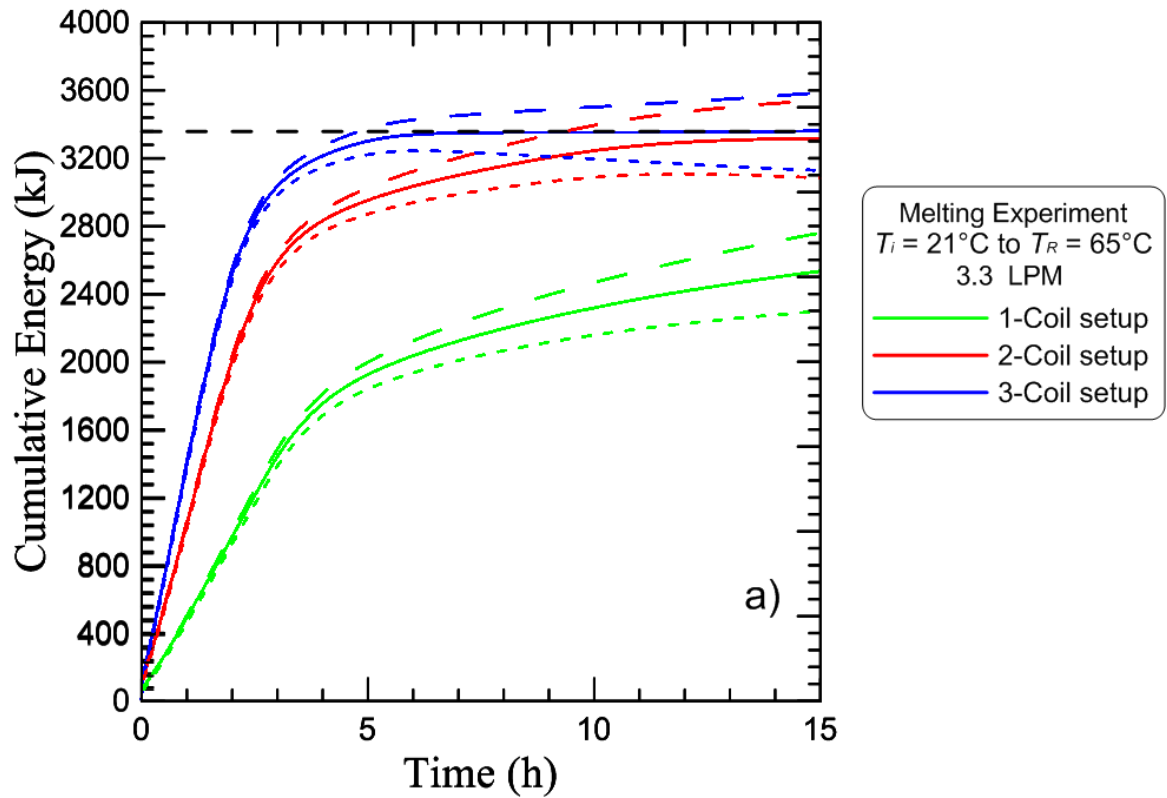


Figure 3.3: Typical cumulative energy profiles obtained during the a) charging and b) discharging processes performed on 1-coil, 2-coil and 3-coil setup.

Figure 3.3 shows the comparison of cumulative energy profiles obtained for 1-coil, 2-coil and 3-coil setups. Figure 3.3a) compares the cumulative energy profiles recorded during the 21 to 65°C charging experiments performed on 1-coil, 2-coil and 3-coil setups at 3.3 L/min. Figure 3.3b) compares the cumulative energy obtained during the 65 to 21°C discharging experiments performed on 1-coil, 2-coil and 3-coil setups at 3.3 L/min. The respective coloured dotted lines in these figures show the upper and lower limit of measurement uncertainties obtained from Eqs. (2.10) and (2.11). The black horizontal dotted line is the theoretical energy storage capacity of the PCM-HX during these experiments calculated by using Eq. (2.12). At the end of these experiments, the theoretical stored energy value falls in between the measurement uncertainties. This validates that using HTF energy change, the energy stored inside the PCM-HX can be reasonably measured.

The cumulative energy profiles of charging experiments increase sharply during the initial periods as the natural convection process boost the heat transfer rates inside the PCM-TES device. However, once all the PCM above the coils melted and the natural convection process inside the PCM-TES is saturated, further heat transfer takes place by means of conduction only. Thus, a sharp bend is observed in these profiles. On the other hand, in the discharging experiments, the natural convection heat transfer is absent from the beginning. Hence, there is no rapid increase in the cumulative energy profiles of discharging experiments. However, due to a gradual increase in the thermal resistance between coils and molten PCM, the rate of heat extracted slowly decreases. Again, these profiles confirm the observations made from Fig. 3.2.

A pressure sensor recorded the pressure drop across the three different configurations of PCM-HX at 3.3 L/min flow rate. The same amount of fluid was passed through the system for all experiments (1-coil, 2-coil or 3-coil). Therefore, the flow velocity in each coil was least for the 3-coil setup, highest for 1-coil setup and in between for the 2-coil setup. The highest pressure drop of around 8 psi was observed in the 1-coil setup, whereas the least pressure drop of around 5 psi was measured in the case of the 3-coil PCM-HX configuration. Also, the pressure drop of around 6 psi was found in the 2-coil setup. Thus, it indicates that the impact of velocity played a bigger role than the additional minor losses through the piping and fittings, etc.

### **3.2 Repeatability of the experimental setup**

This section presents the power curves (heat transfer rate as a function of time) and stored energy profiles obtained during the various charging and discharging experiments performed on the 1-coil, 2-coil and 3-coil setups. Before conducting all the experiments, the repeatability of the experimental setup was confirmed by performing one charging ( $T_i = 21^\circ\text{C}$  to  $T_R = 65^\circ\text{C}$ ) and discharging ( $T_i = 65^\circ\text{C}$  to  $T_R = 21^\circ\text{C}$ ) experiment three times on the 2-coil and 3 Coil setups with a HTF flow rate of 3.3 L/min. No repeatability test was conducted on the 1-coil setup as it takes extended periods (approximately 60 hours) for the completion of the experiment. The obtained power curves during the repeated experiments are shown in Fig. 3.4. These results are almost coinciding with each other, which confirms the high repeatability of the experiment and the experimental setup. Thus, the rest of all other remaining experiments mentioned in Section 2.3 were carried out only once in this study.

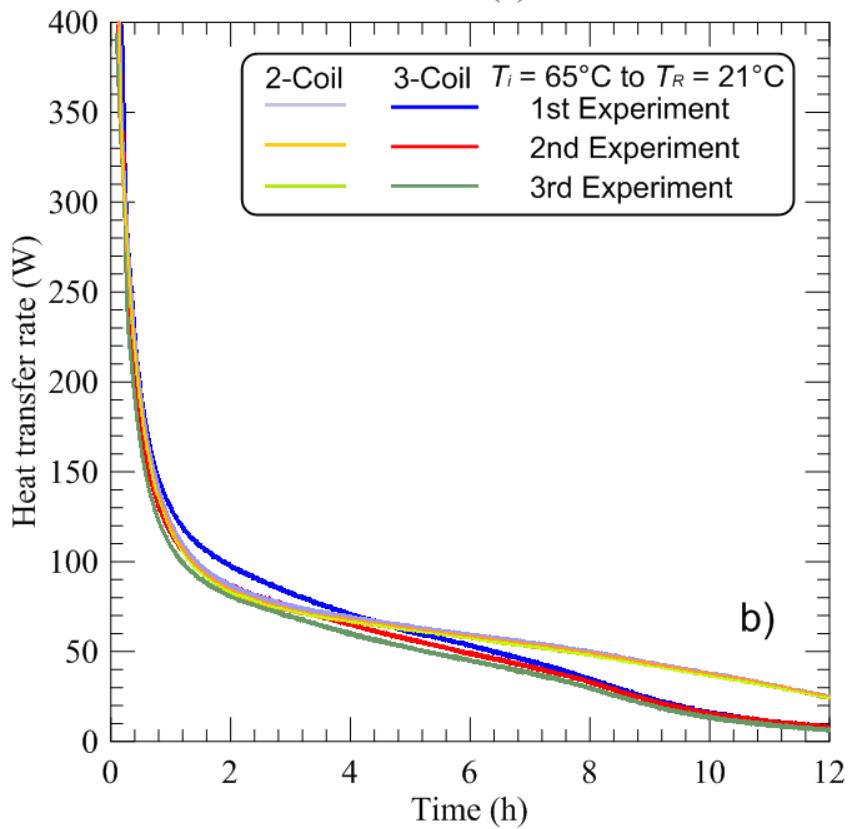
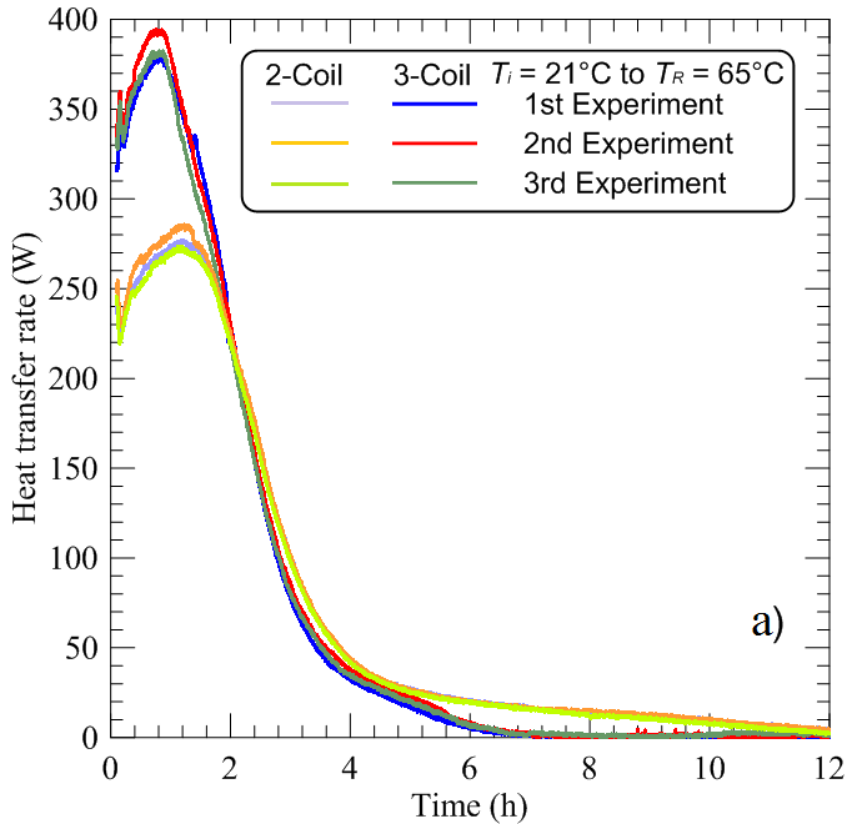
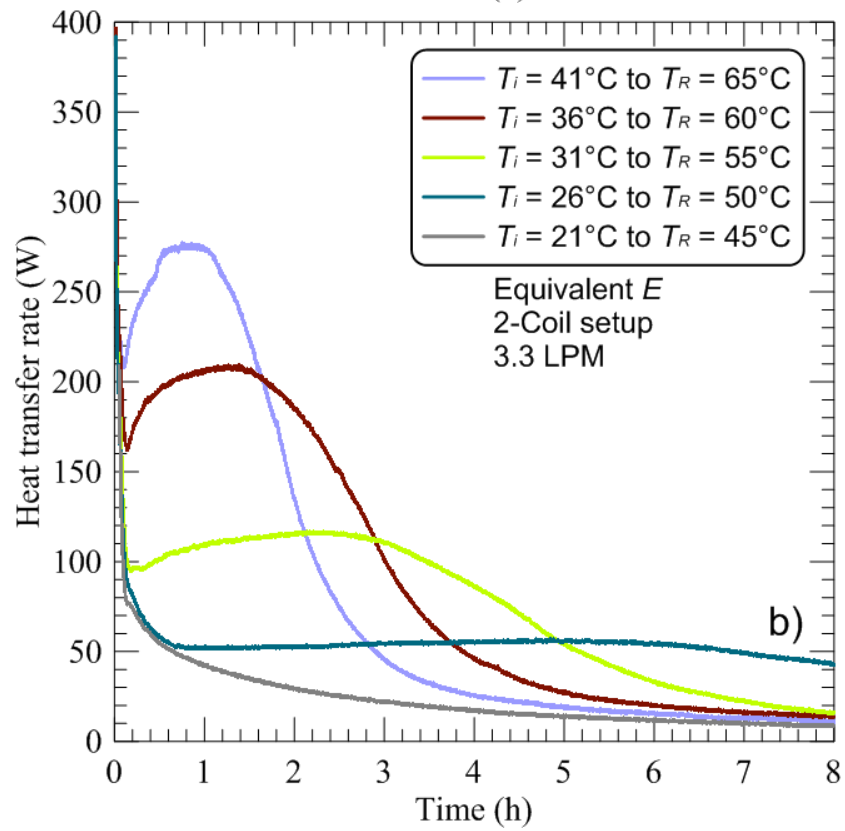
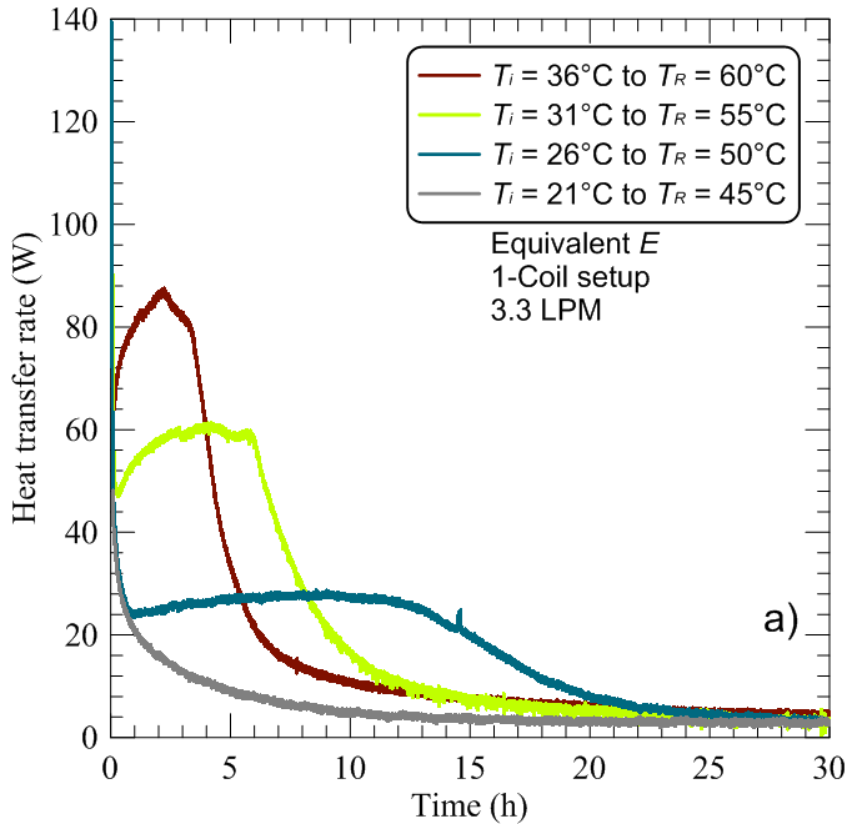


**Figure 3.4: Power curves obtained during the repeatability test performed on 2-coil and 3-coil setups with a HTF flow rate of 3.3 L/min: a) charging and b) discharging processes.**

### 3.3 Charging experiment results

Figures 3.5, 3.6 and 3.7 show the power curves obtained during the various charging experiments performed on 1-coil, 2-coil and 3-coil setups with a HTF flow rate of 3.3 L/min. These experimental results are classified into 3 groups as shown in Fig. 2.11. Figure 3.5 presents the results for experiments with the same equivalent energy ( $E$ ) changes. Figure 3.6 shows the results obtained for experiments with the same initial temperature of the PCM ( $T_i$ ) and Fig. 3.7 presents the results obtained for experiments with the same final temperature of PCM ( $T_R$ ).

All the results shown in Figs. 3.5, 3.6 and 3.7 follow a similar pattern. During the early stage of the charging process (first 20 minutes or less) conduction heat transfer is the dominant process. Initially, the heat transfer rates are large due to the high temperature difference between the PCM and HTF flow. Except for Fig. 3.5, this initial heat transfer data (*i.e.* first 6 minutes result) is not shown as the initial result part of different experiments overlap with each other and make graphs unreadable. However, rapidly the heat transfer rate starts dropping as the driving temperature difference between the HTF and PCM starts dropping. Meanwhile the PCM surrounding the copper coils starts melting. Once the volume of molten PCM around the copper coils inside the PCM-HX is large enough, heat transfer moves to convection and the heat transfer rate re-increase (Azad *et al.*, 2019). The power then reaches a maximum and slowly decreases afterward as the temperature difference between the HTF and PCM slowly decreases. As expected, all these obtained power curves confirm that a larger amount of heat is transferred (higher power are achieved) with an increase in the number of coils.



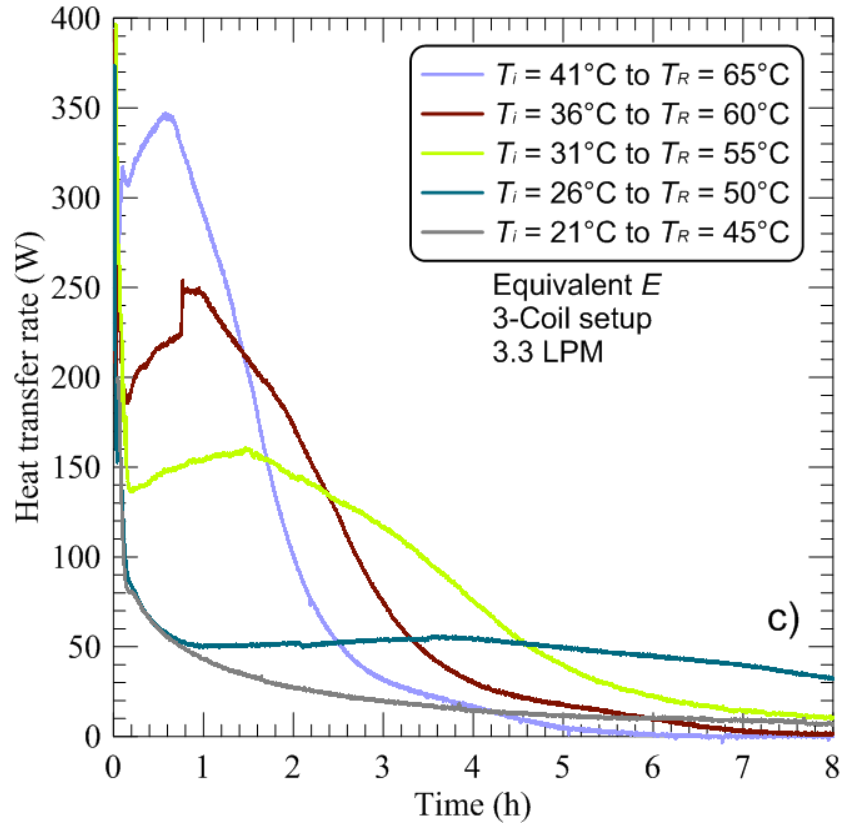


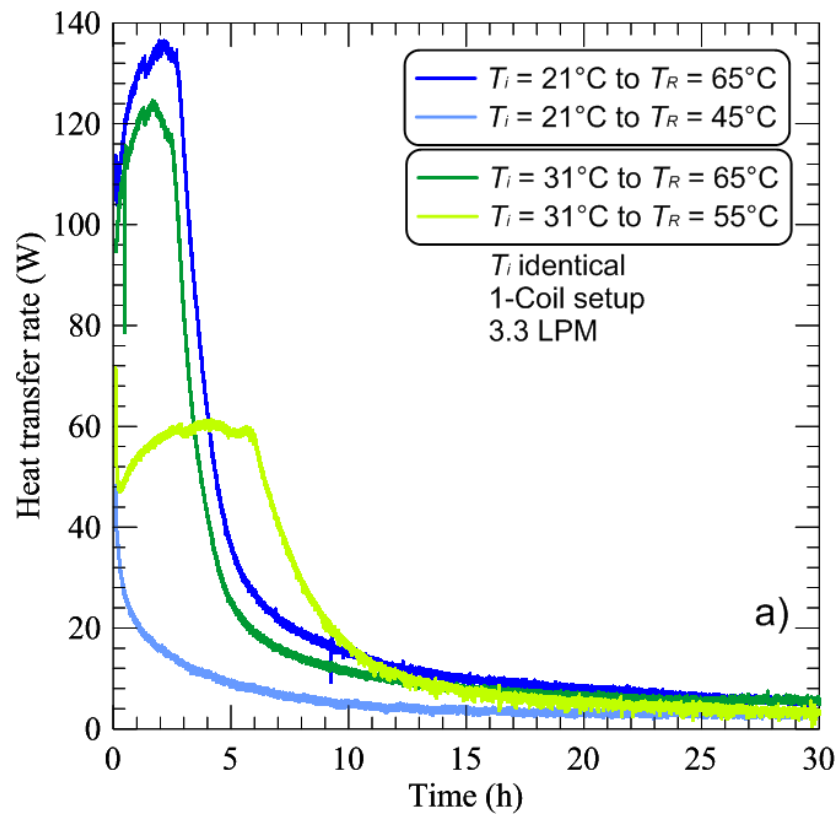
**Figure 3.5: Equivalent energy ( $E$ ) experiment results (power curves) obtained during the charging process of a) 1-coil, b) 2-coil and c) 3-coil setups with a HTF flow rate of 3.3 L/min.**

The results from Fig. 3.5 show that the temperature difference between the HTF and the PCM melting point plays a very significant role in the heat transfer process in the PCM-HX. This figure shows charging processes that ultimately exchange the same amount of energy and start with the same initial overall temperature difference between the HTF and the PCM. However, the amount of heat transfer through a given exchange system increases with an increase of the driving force being the temperature difference between the HTF and the PCM melting point, *i.e.* ( $T_R - T_m$ ).

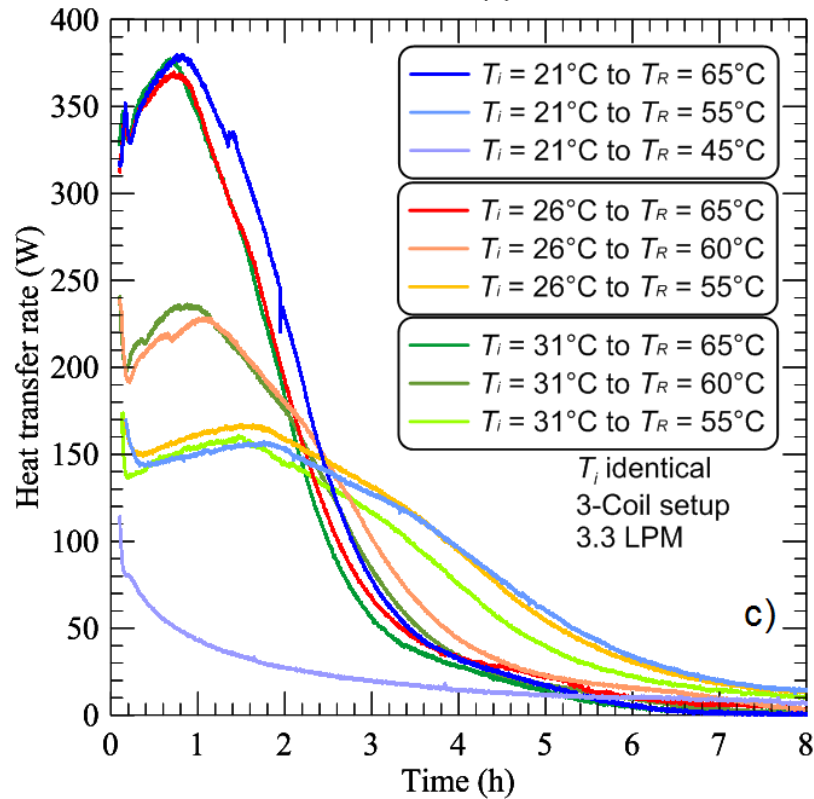
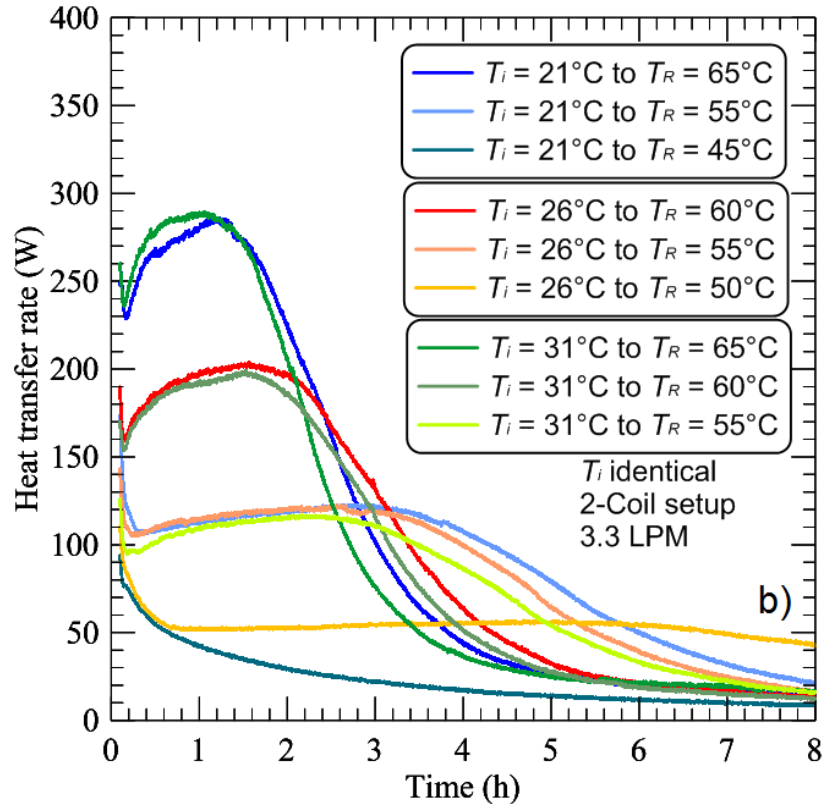
The same conclusion is reached by looking at Fig. 3.6. In these experiments, the starting temperature of PCM inside the PCM-HX is identical but the HTF temperature passing through it is different. Hence, the amount of energy to be transferred is different in each

experiment. The results show that the larger the HTF temperature is, the higher the maximum power obtained.

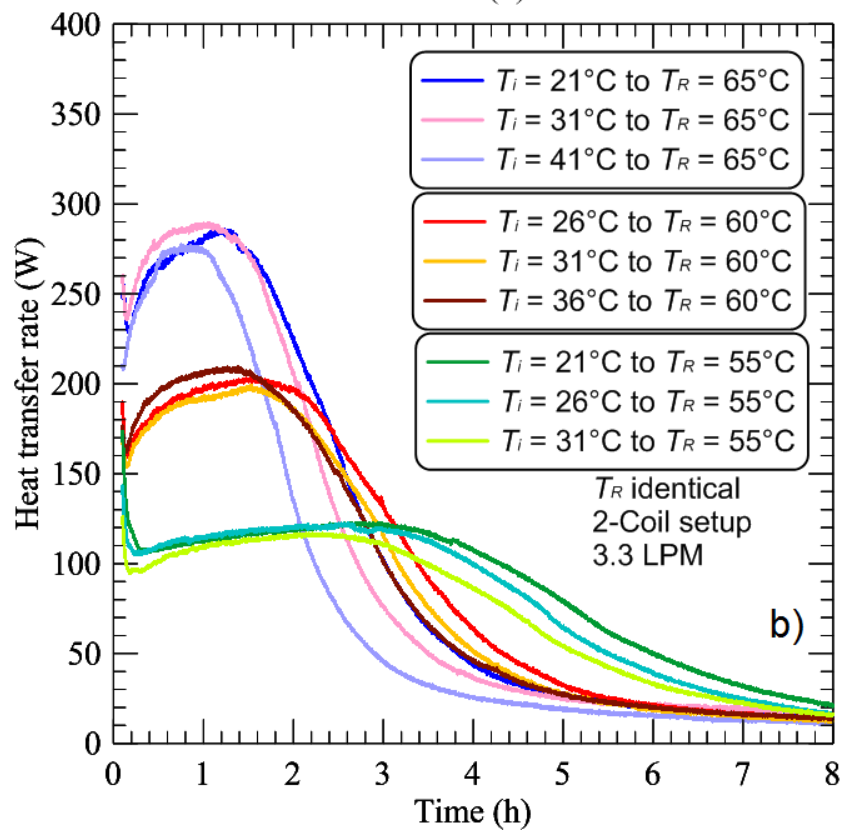
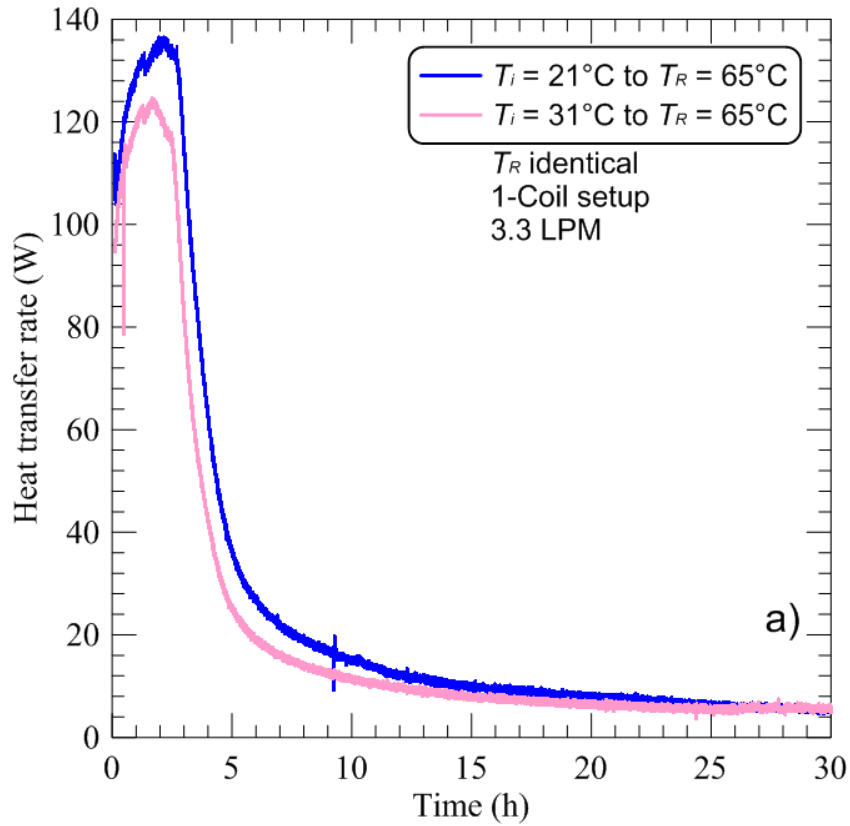
Finally, Fig. 3.7 points to the fact that in the heat transfer process, the initial temperature of the PCM plays a very minor role compared to the temperature difference between the HTF and the PCM melting point. The power curves look almost identical in this case irrespective of the initial PCM temperature, and by extension the initial temperature difference between HTF and PCM, ( $T_R - T_i$ ). This points to the difference between the HTF temperature and PCM melting point being an important factor in determining the power. This can be explained by the smaller amount of sensible heat stored in the solid PCM, so the solid PCM quickly warms up to the melting temperature.







**Figure 3.6: Same initial PCM temperature ( $T_i$ ) experiment results (power curves) obtained during the charging process of a) 1-coil, b) 2-coil and c) 3-coil setups with a HTF flow rate of 3.3 L/min.**



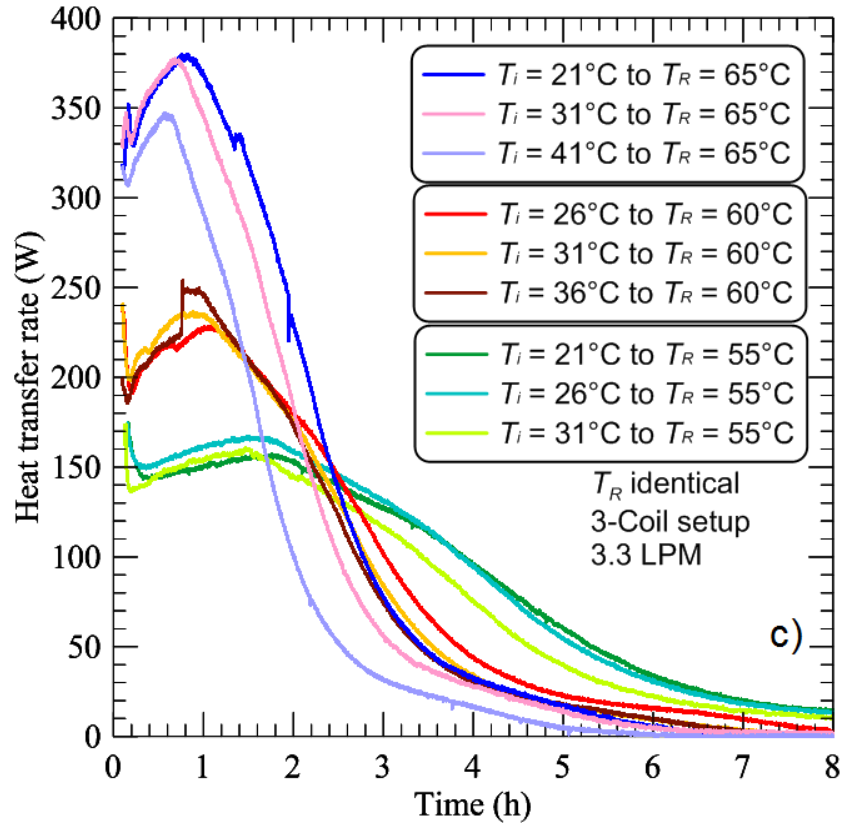


**Figure 3.7: Same final PCM temperature ( $T_R$ ) experiment results (power curves) obtained during the charging process of a) 1-coil, b) 2-coil and c) 3-coil setups with a HTF flow rate of 3.3 L/min.**

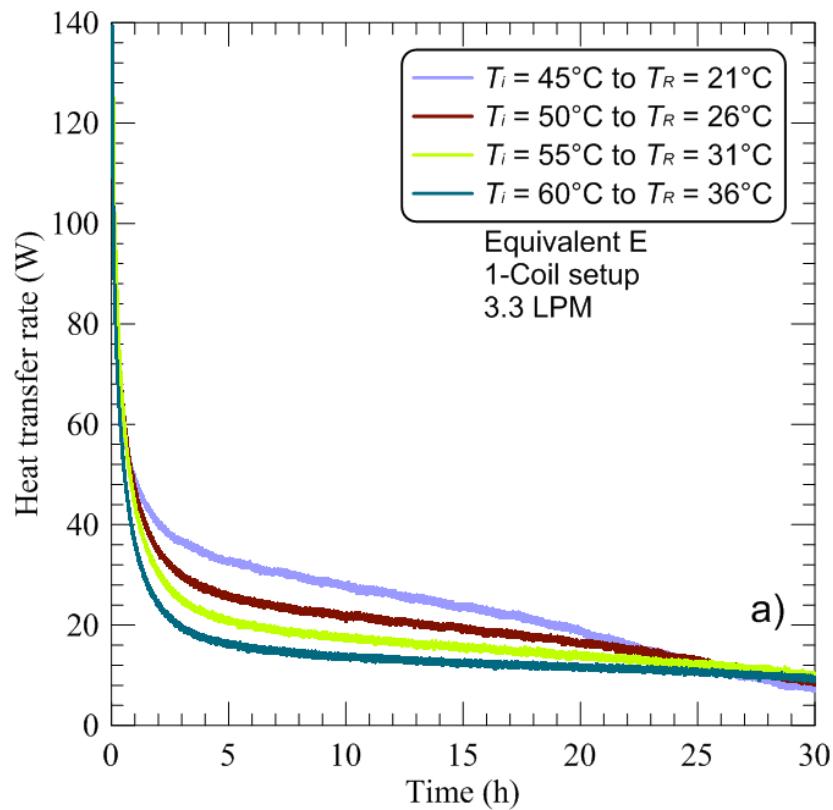
### 3.4 Discharging experiment results

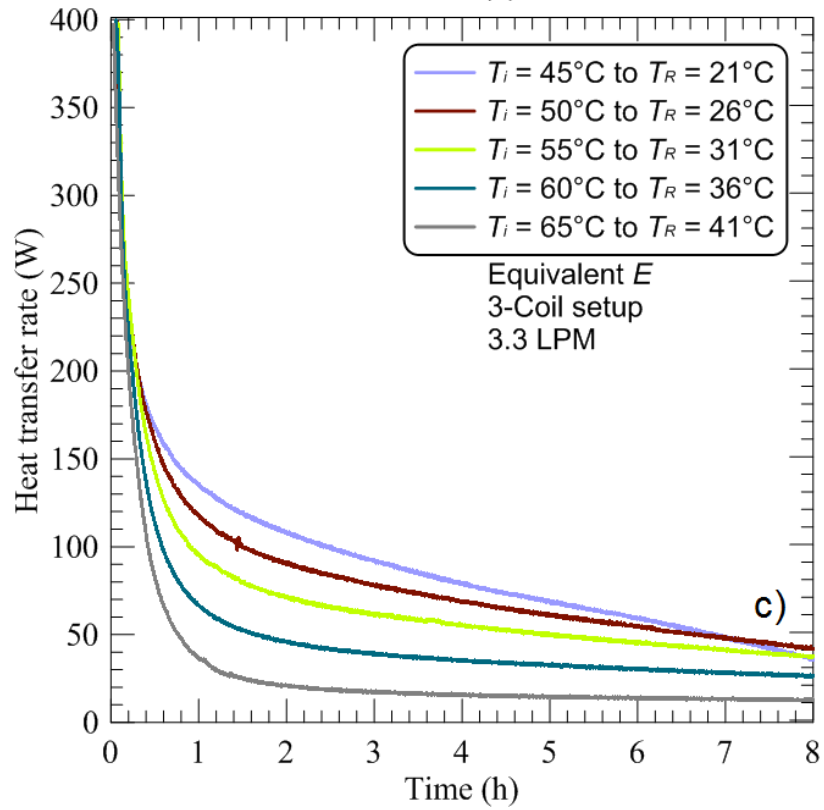
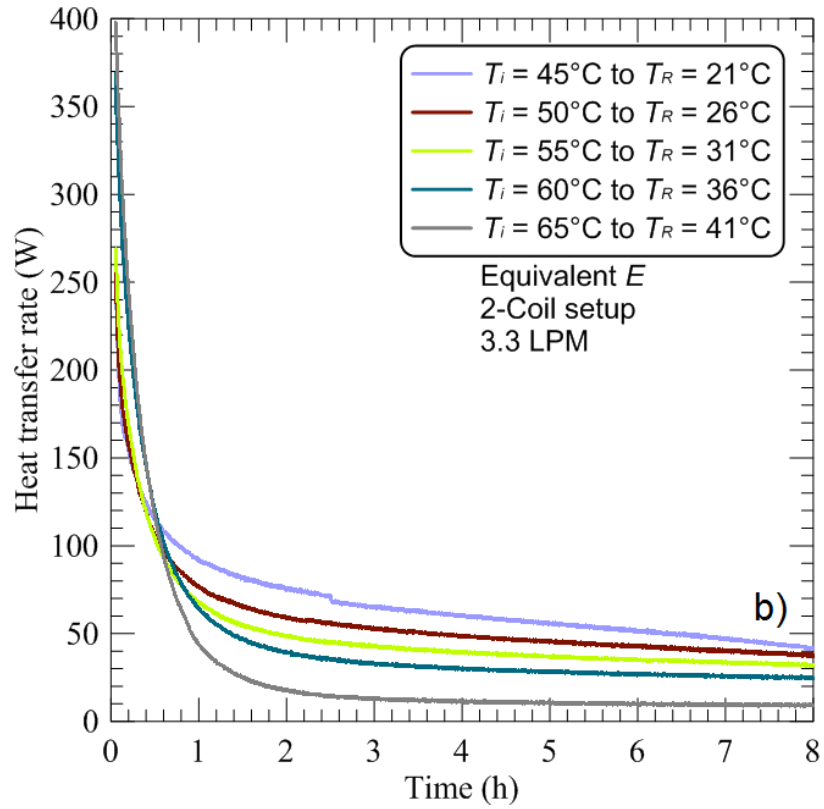
Figures 3.8, 3.9 and 3.10 show the power curves obtained during the various discharging experiments performed on 1-coil, 2-coil and 3-coil setups with a HTF flow rate of 3.3 L/min. Again, these experiments are classified into 3 groups and presented in separate graphs as follows: Fig. 3.8 presents the results for experiments with the same equivalent energy ( $E$ ) change, Fig. 3.9 presents the results obtained for experiments with the same initial temperature of PCM ( $T_i$ ), and Fig. 3.10 presents the results obtained for experiments with the same final temperature of PCM ( $T_R$ ).

Like charging, all the results for discharging follow a similar pattern. The main mode of heat transfer during the entire process is conduction, which leads to a constant decrease in

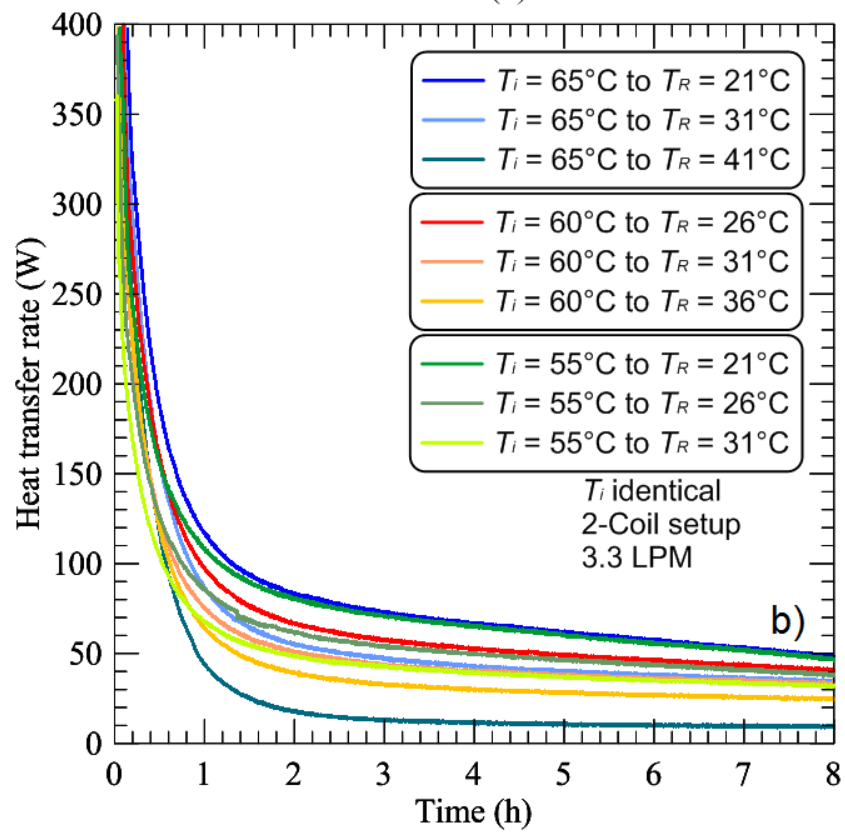
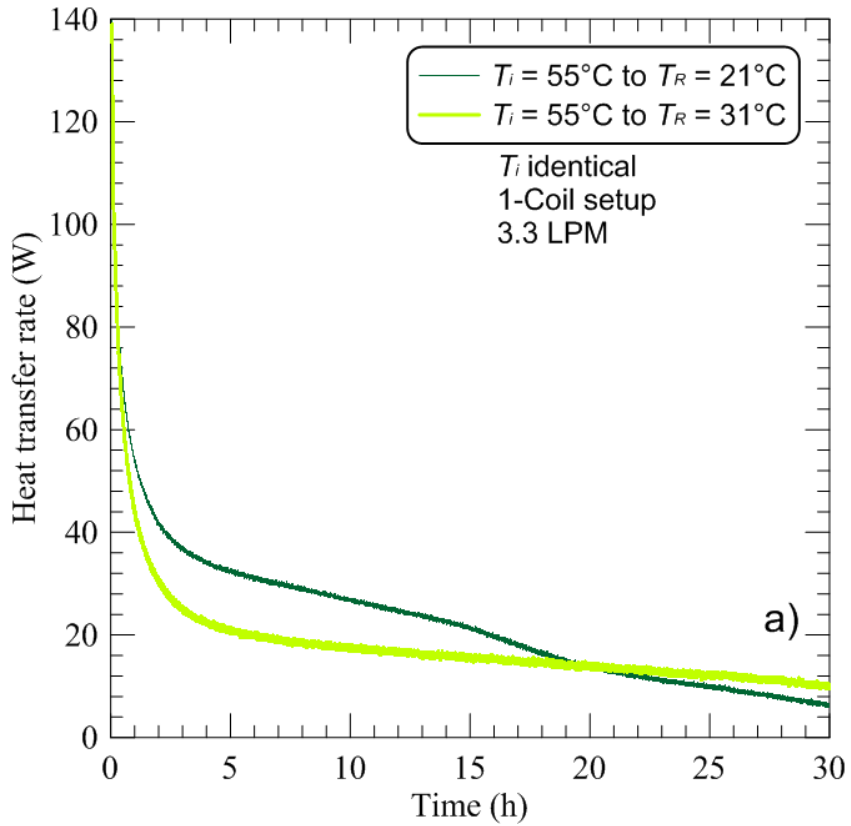
the heat transfer rate over time. This constant decrease can be explained by the combination of two processes: i) the slow build-up of solid PCM around the coils in the enclosure, adding to the overall heat transfer resistance, and ii) the ever-decreasing temperature difference between the HTF and the PCM in the enclosure.

Similar conclusions as the ones reached from the results of Figs. 3.5, 3.6 and 3.7 can be reached here in terms of the impact of initial, final/HTF and melting temperatures. During the discharging process, the temperature between the HTF and PCM melting point has significant impact on the obtained heat transfer rates. However, its impact is not as pronounced as it is during the melting process.





**Figure 3.8: Equivalent energy ( $E$ ) experiment results (power curves) obtained during the discharging process for the a) 1-coil, b) 2-coil and c) 3-coil setups with a HTF flow rate of 3.3 L/min.**



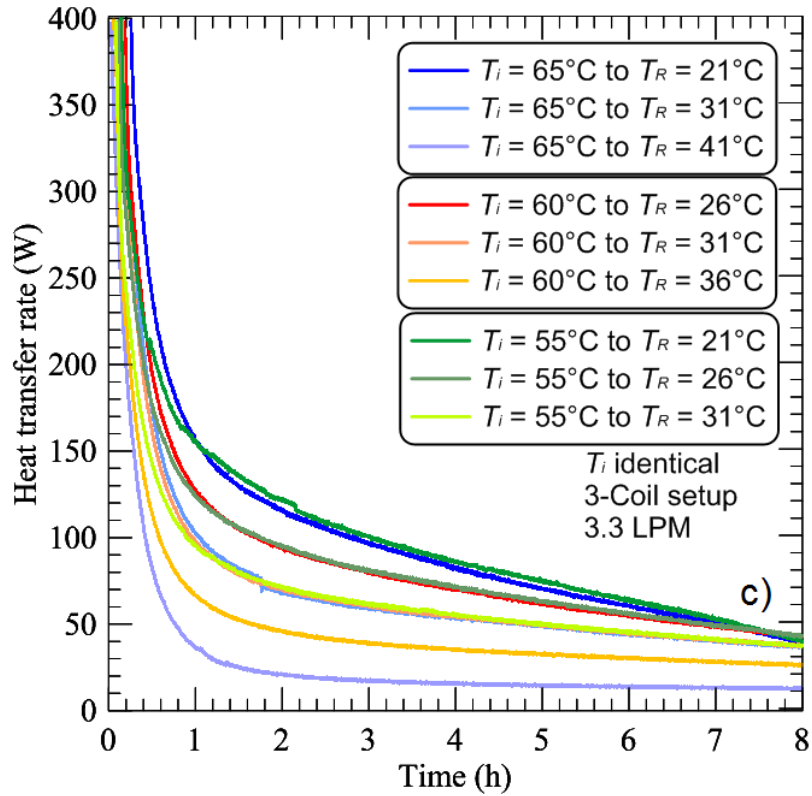
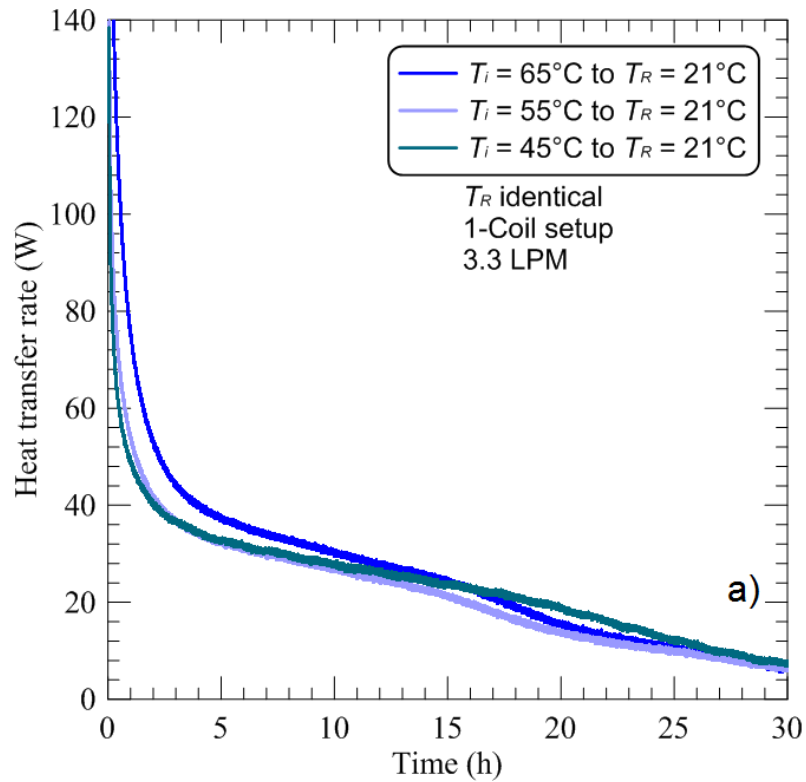


Figure 3.9: Same initial PCM temperature ( $T_i$ ) experiment results (power curves) obtained during the discharging process of a) 1-coil, b) 2-coil and c) 3-coil setups with a HTF flow rate of 3.3 L/min.



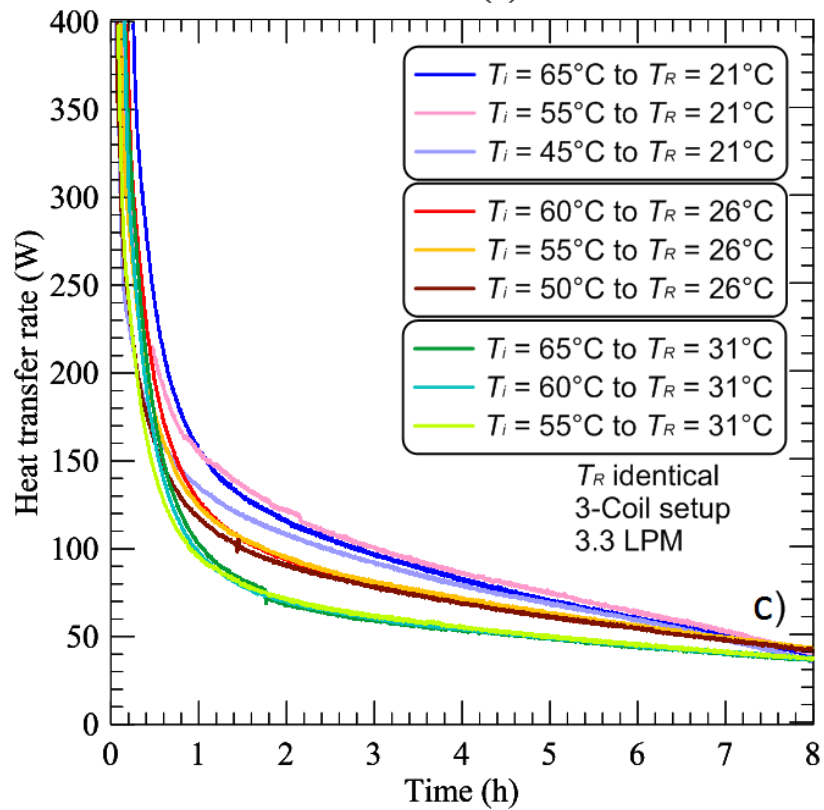
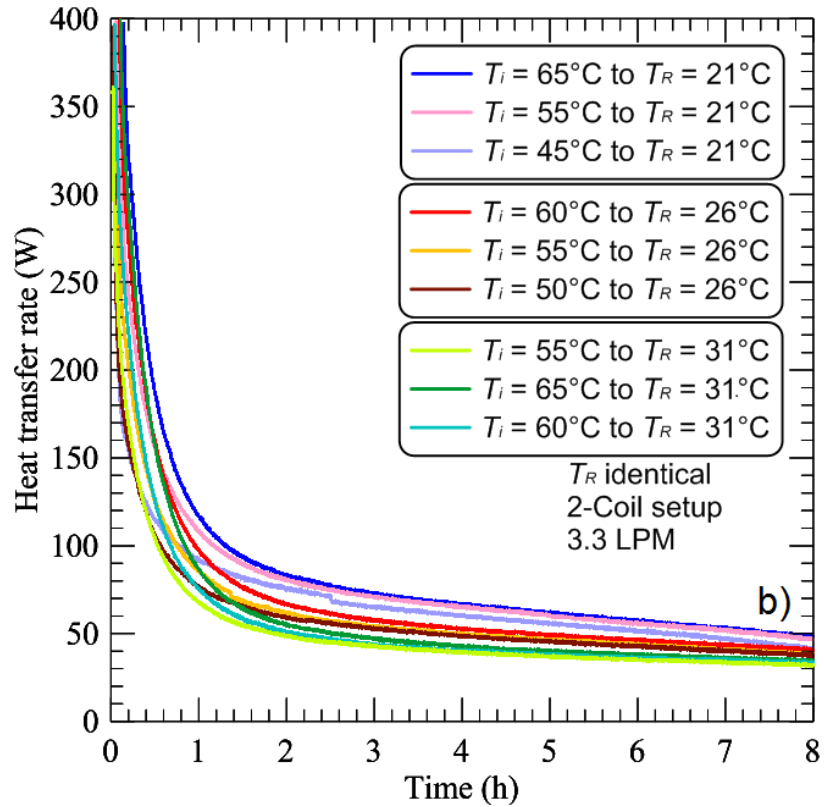


Figure 3.10: Same final PCM temperature ( $T_R$ ) experiment results (power curves) obtained during the discharging process of a) 1-coil, b) 2-coil and c) 3-coil setups with a HTF flow rate of 3.3 L/min.



### **3.5 HTF flow rate variation**

Figure 3.11 shows the comparison of power curves obtained during the charging (Fig. 3.11a) and discharging processes (Fig. 3.11b) using the 3-coil setup with two different HTF flow rates of 3.3 L/min and 6.3 L/min. From the charging results, it can be observed that the power curves hardly change with this change of flow rate, especially for the experiments using the highest (or lowest) HTF temperature. In that case, the already large temperature differential between the HTF and PCM is barely affected by the slight increase in the overall heat transfer coefficient caused by the increased HTF flow rate. A minor deviation in the power curve is observed during the charging experiments at lower HTF temperatures; showing a slight effect of an increased flow rate.

The discharging results show no noticeable difference with the change in the flow rate. It can be explained by the fact that the thermal resistance at the PCM side is way larger than the HTF side due to the low thermal conductivity of the PCM. Hence, a slight improvement in the HTF side thermal resistance is not affecting the overall thermal resistance between the HTF and PCM.

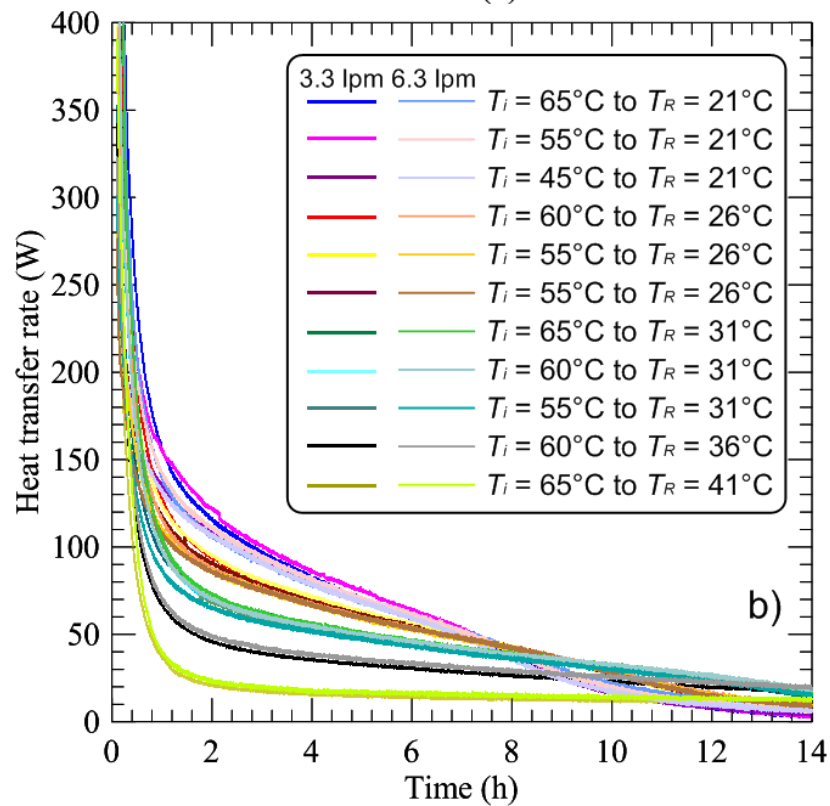
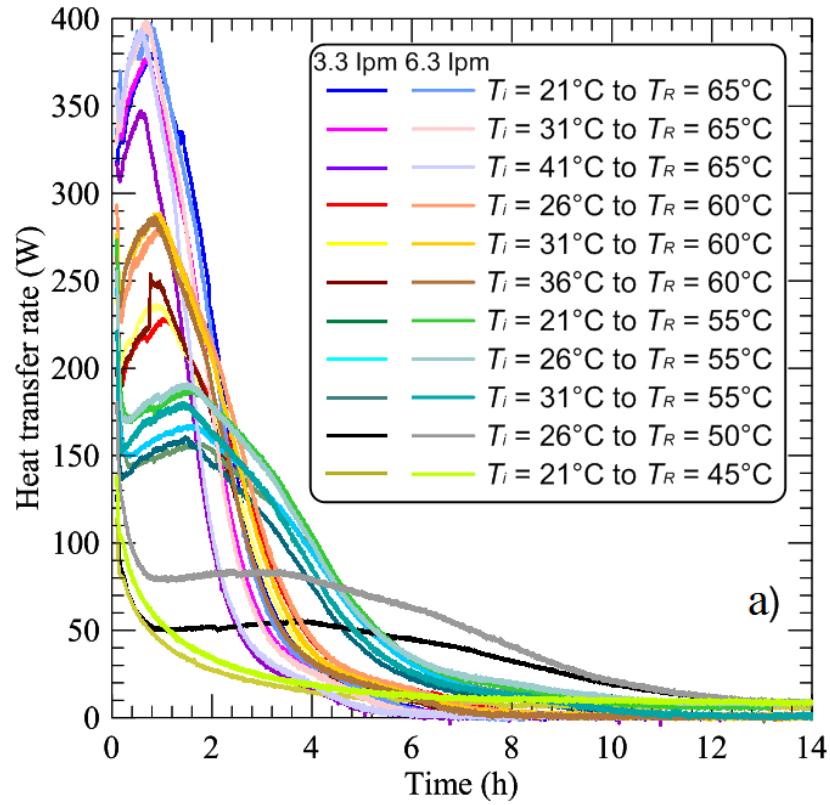


**Figure 3.11: Heat transfer rates as a function of time using the 3-coil setup with flow rates of 3.3 and 6.3 L/min for various temperature combinations: a) during charging and b) during discharging.**

### **3.6 Chapter conclusion**

In this chapter, the nature of measured temperatures and cumulative energy stored profiles for charging and discharging experiments are observed. From these figures, it is found that by measuring the change in the HTF temperature from inlet to outlet of PCM-HX, the energy stored inside the PCM can be reasonably calculated. Also, the pressure drop readings measured across the different PCM-HX configurations suggested that the HTF velocity through individual coils plays a larger role in determining the pressure drop than the additional minor losses through the piping and fittings, etc.

Also, the various charging and discharging experiments are compared by plotting their characteristic power curves. It has been observed that the heat transfer rate of PCM-HX device increases with each additional coil. Also, it is noticed that the HTF temperature has a greater impact on the heat transfer rate between the PCM and HTF than the initial PCM temperature. Moreover, the results of equivalent energy experiments showed that the difference between the HTF temperature and PCM melting point has a great effect on the heat transfer rate. Also, the comparison of different HTF flow rate experiments has proved that the HTF flow rate has a negligible effect on the heat transfer rate, over the range of flow rates used in this experimental work.

These obtained transient results are not very helpful in comparing the performance of different designs of PCM-HXs as the heat transfer rate varies largely in each experiment. Also, each experiment stores different amounts of energy and takes different amounts of time for their completion. Thus, the question arises which heat transfer rates to choose for the comparison? And which time frame results should be considered for the comparison? To solve this problem, there is a need to convert these transient results into single time-

independent metrics, which will incorporate the effect of different operating and geometrical variations. It will make the comparison process easier, quicker and more universally applicable.

## **Chapter 4: Data reduction, comparison and discussion**

In the previous chapter, different experiments performed on the PCM-HXs were compared by plotting their transient heat transfer rates as a function of time. During these experiments, the various operating parameters like initial PCM temperature, HTF temperature, the mass of PCM used (although kept constant in this work) and the surface area between the PCM and HTF etc. influenced the obtained heat transfer rates. However, it is difficult to quantify the effect of these parameters by simply referring to the transient heat transfer rate graphs as the question arises: which time data should be considered to measure their effects? Thus, there is a need to reduce these obtained transient results and present them as a time-independent quantity. Therefore, using different methods, the obtained transient results are converted into various time-independent quantities and compared in this chapter. These methods involved calculating average heat transfer rates over the various duration of experiments, plotting graphs of instantaneous heat transfer rate as a function of stored/extracted energy, calculating the average heat transfer rates over the total stored/extracted energy during experiments and obtaining normalized average power (defined in Eq. (1.6)) values for different experiments.

### **4.1 Comparison of experiments using average power obtained over specific period**

The average heat transfer rate obtained during an experiment is easy to calculate and unique to the experiment. Thus, it can be a possible time-independent representation of transient results. Hence, in this section, the charging and discharging results of different coil configurations presented in the previous chapter are reduced by using average power terms in order to make the comparison independent of time. This term is calculated by

integrating the area under the instantaneous power curve over a specific period of operation, starting from  $t = 0$ . In most of the experiments mentioned in Chapter 3, a large portion of the energy is stored (or extracted) in the first 4 hours of the experiments. Thus, the average power over the first 2 and 4 hours of operation are only calculated and compared. The uncertainties associated with the average power during a particular experiment are calculated by integrating the corresponding instantaneous  $Q_{actual,max}$  and  $Q_{actual,min}$ , described by the Eqs. (2.7) and (2.8), over the respective time periods.

Figures 4.1 and 4.2 compare various charging and discharging experiments performed on the different coil configurations of the PCM-TES using average power over the first 2 hours and 4 hours of operation respectively as a function of HTF temperature used for the various initial temperatures of the PCM. These figures show similar trends, first that the average power increase with the number of coils. This can be explained by the increase in the heat transfer area with each additional coil inside the PCM-TES device. During the discharging experiments, this increase in the heat transfer rate is uniform with the number of coils. In contrast, this increase is not in equal proportion for charging experiments as the increase in the heat transfer rate from 1-coil to 2-coil is greater than the increase from 2-coil to 3-coil setup. It can be explained by the natural convection process taking place at the bottom half of PCM-HX during charging process. In the case of 1-coil setup, the natural convection heat transfer process is totally absent in the bottom half of PCM-HX as there is no HTF carrying coil in this part. In the 2-coil setup, the bottom coil is well dipped in the bottom half of PCM-HX. Thus, in the 2-coil setup, the natural convection heat transfer starts in the bottom half of the PCM-HX and it largely increases the heat transfer rate inside the 2-coil setup compared to 1-coil setup.

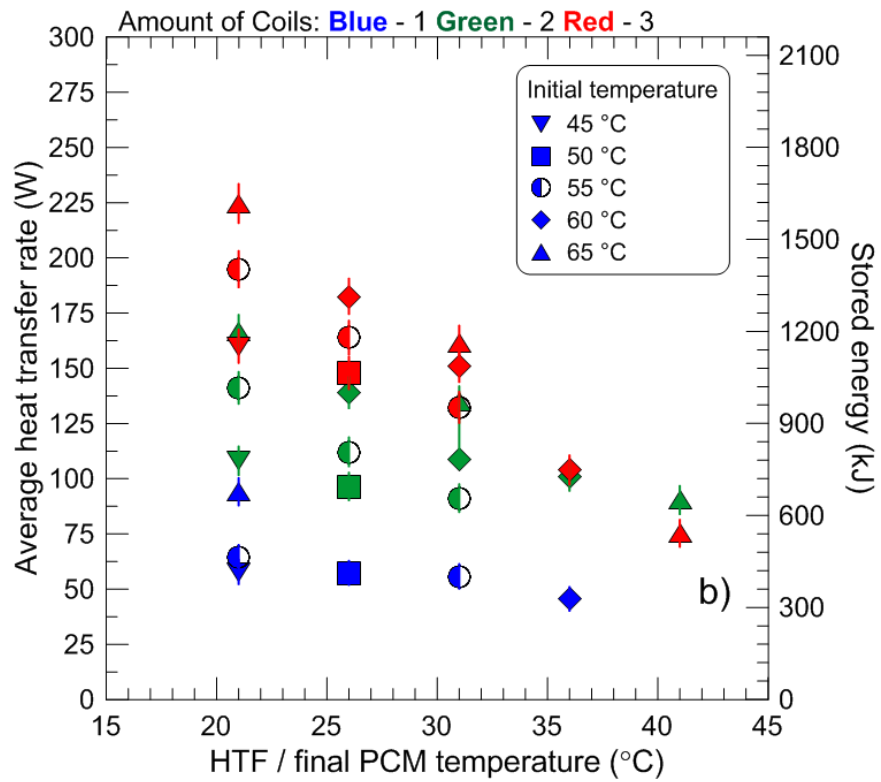
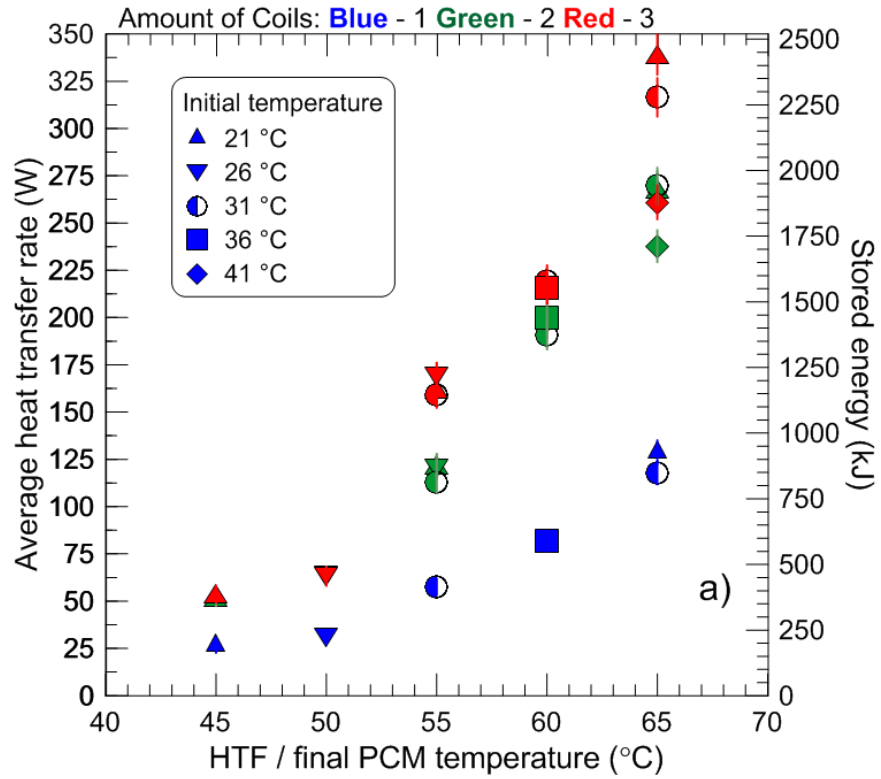


**Figure 4.1: Average system power over the first 2 hours as a function of the HTF temperature obtained during a) charging and b) discharging processes at 3.3 L/min HTF flow rate.**

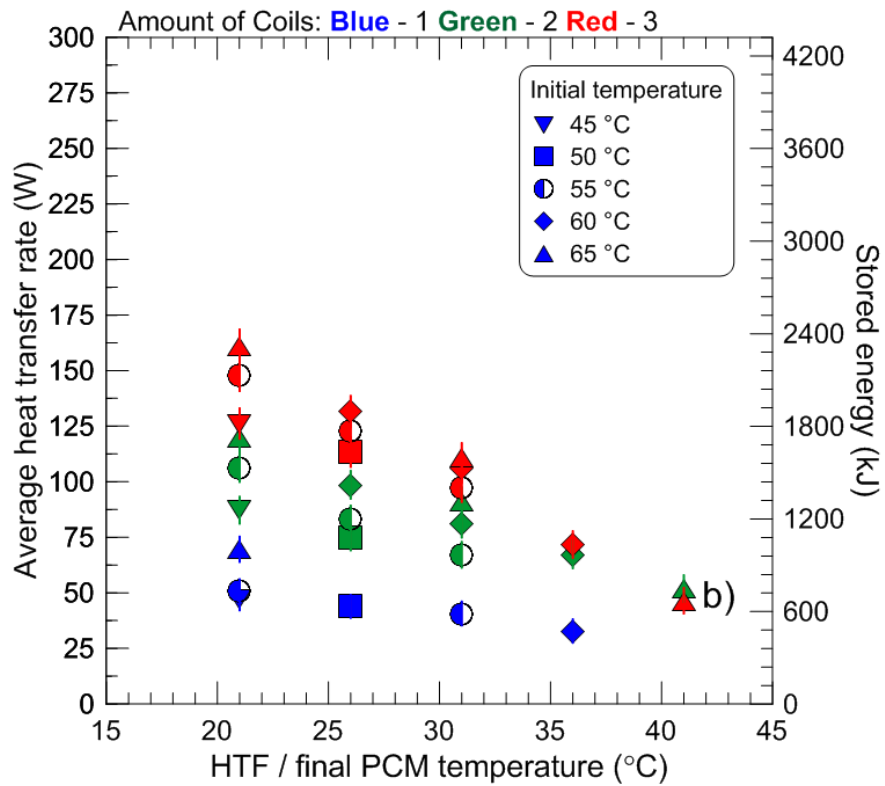
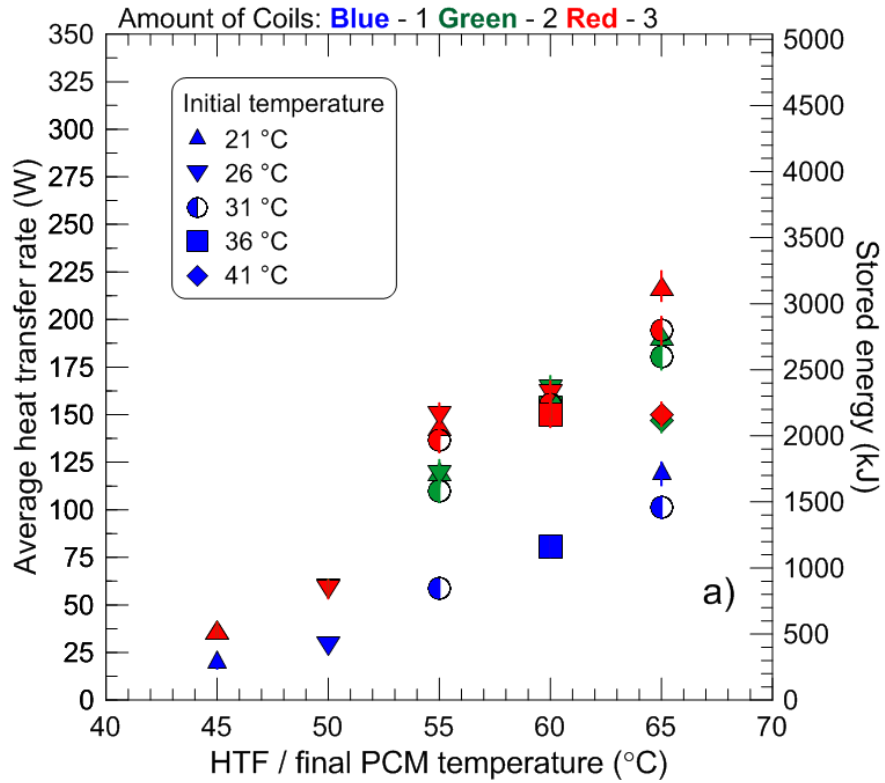


**Figure 4.2: Average system power over the first 4 hours as a function of the HTF temperature obtained during a) charging and b) discharging processes at 3.3 L/min HTF flow rate.**



On the other hand, in the 3-coil setup, the position of its bottom coil changes slightly compared to the bottom coil position of 2-coil setup. Therefore, the natural convection heat transfer increases slightly in the bottom half of PCM-HX of 3-coil setup compared to the 2-coil setup. Also, the amount of HTF flowing through the coils of the 3-coil setup is less than that of the 2-coil setup, as the total HTF flow rate of these two setups are identical. Hence, only a slight increase in the heat transfer rate is observed from 2-coil to 3-coil setup.

Secondly, the HTF temperature shows a greater impact on the obtained average heat transfer rate than the initial temperature of the PCM. Also, very little impact of the initial PCM temperature on the heat transfer rate can be seen during the discharging experiments. However, this effect is hardly noticeable in the charging experiments. Moreover, it appears that the impact of initial PCM temperature on the heat transfer rate increases as the difference between the HTF temperature and PCM melting point increases.

Figures 4.1 and 4.2 used the HTF temperature and PCM initial temperatures to compare heat transfer rates. However, their influence on the heat transfer process inside the PCM changes with the properties of PCM used (Sponagle and Groulx, 2016). Therefore, to compare different systems that could be using different PCMs with different melting temperatures and latent heat capacities, it would be useful to compare the charging and discharging characteristics of those systems on a dimensionless basis. Therefore, the use of Stefan number is helpful in this regard as it incorporates the effect of the used PCM transition temperature and latent heat capacity. There can be two types of Stefan numbers defined for PCMs one based on the PCM melting temperature and another based on the initial temperature of the PCM. In the previous chapter, it has been seen that the heat

transfer rates are more influenced by the temperature difference between the HTF temperature and PCM melting point than the HTF temperature and initial PCM temperature. Thus, the heat transfer results are compared as functions of different melting Stefan number ( $Ste_m$ ) values at different total Stefan numbers ( $Ste_t$ ).

Therefore, in Figs. 4.3 and 4.4, the average power over the first 2 and 4 hours of operations obtained during various charging and discharging experiments performed on the different coil configurations of the PCM-TES are shown as a function of melting  $Ste_m$  for various  $Ste_t$ . Logically, these results show a similar trend as shown in Figs. 4.1 and 4.2, *i.e.*, the average heat transfer rate increases with the increasing number of coils used inside the PCM-TES device. And the  $Ste_m$  has a more significant impact on the obtained average heat transfer than the  $Ste_t$ . Also, the effect of  $Ste_t$  on the heat transfer rate increases with the higher  $Ste_m$  value.

Finally, from Figs. 4.1, 4.2, 4.3 and 4.4, it can be observed that for any coil configuration the increase in the average heat transfer rate for charging experiments appears to be parabolic, whereas this increase is linear for the discharging experiments. Again, it can be seen that the average heat transfer rates obtained over the first 2 hours period during any experiment are greater than the corresponding results obtained over the first 4 hours period. This can be explained by the fact that during the initial period of experiments, a large amount of energy is stored (or extracted) as the temperature difference between the PCM and HTF is larger. However, as time passes, the temperature difference between the PCM and HTF decreases, resulting in lower instantaneous heat transfer rates. Thus, the average heat transfer rates obtained over the first 4 hours period appear to be lower than the first 2 hours period.

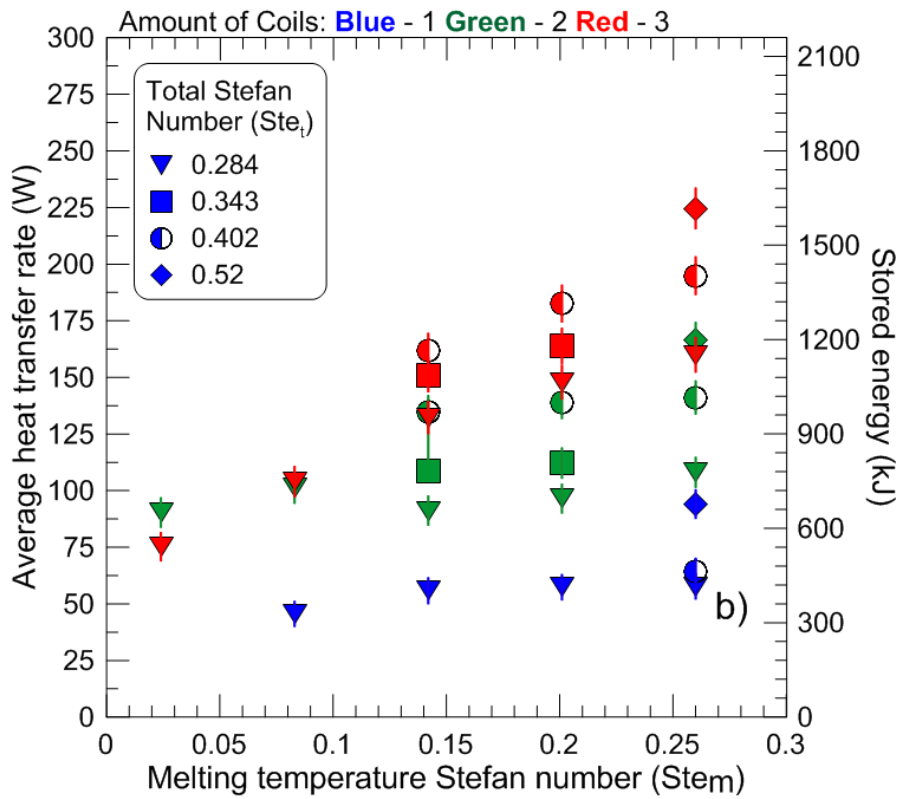
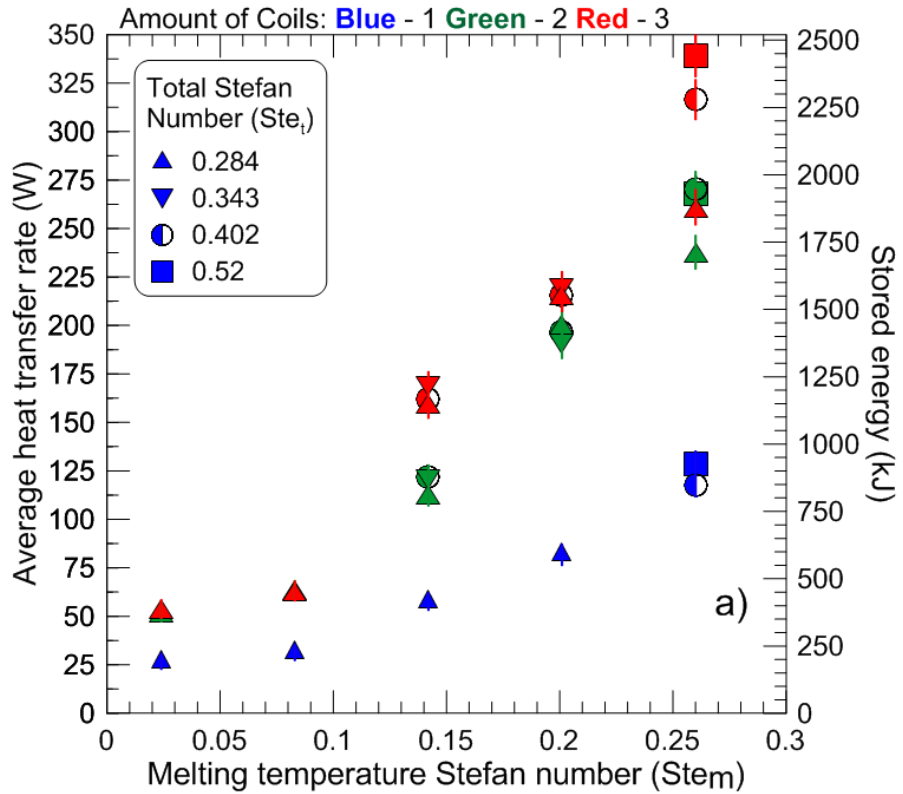


Figure 4.3: Average system power over the first 2 hours as a function of  $Stem$  for various  $Ste_t$  obtained during a) charging and b) discharging processes at 3.3 L/min HTF flow rate.

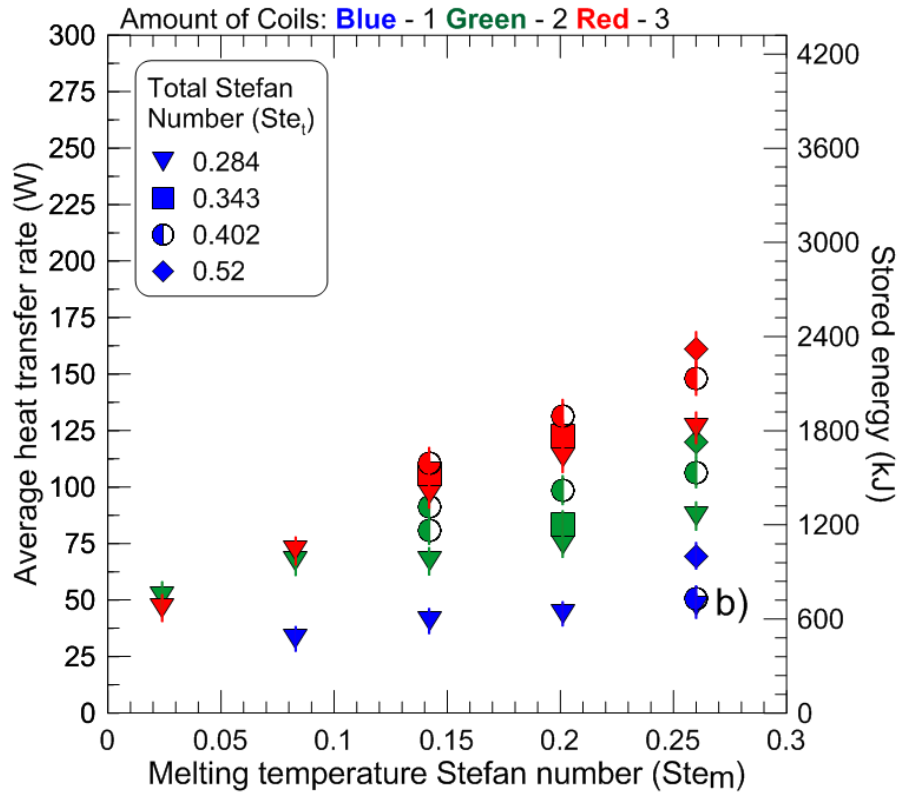
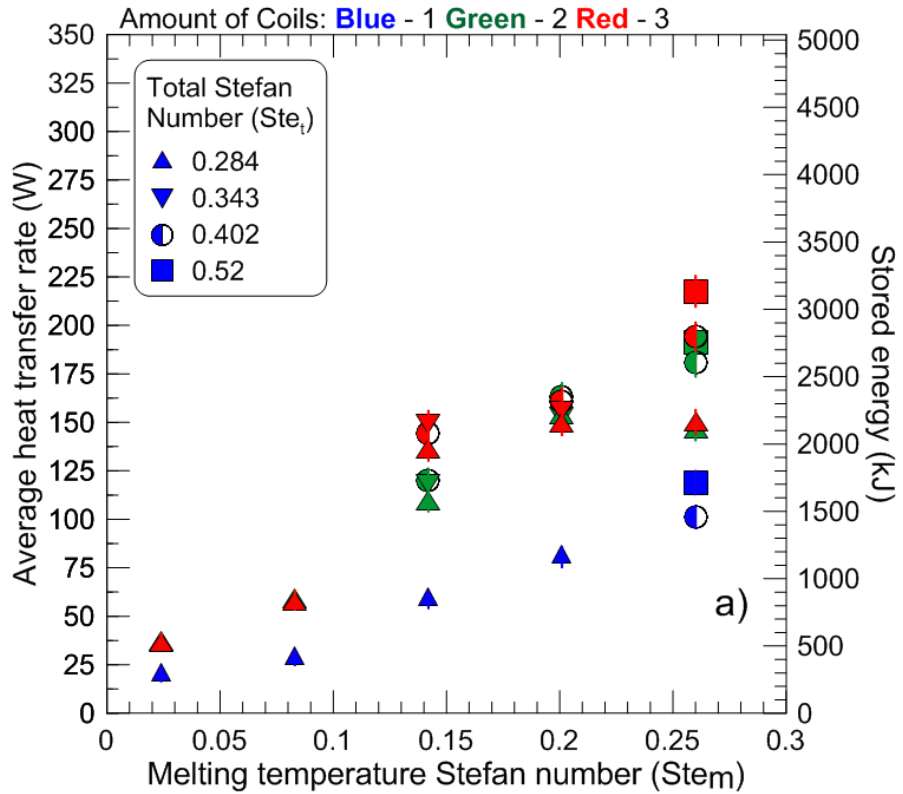


Figure 4.4: Average system power over the first 4 hours as a function of  $Stem$  for various  $Ste_t$  obtained during a) charging and b) discharging processes at 3.3 L/min HTF flow rate.

This does point to the fact that simply taking an average over an arbitrary time span cannot be the fundamental way of determining a comparative average power. And there is a need for a much broader and unique characteristic approach to define the overall heat transfer process of the experiments.

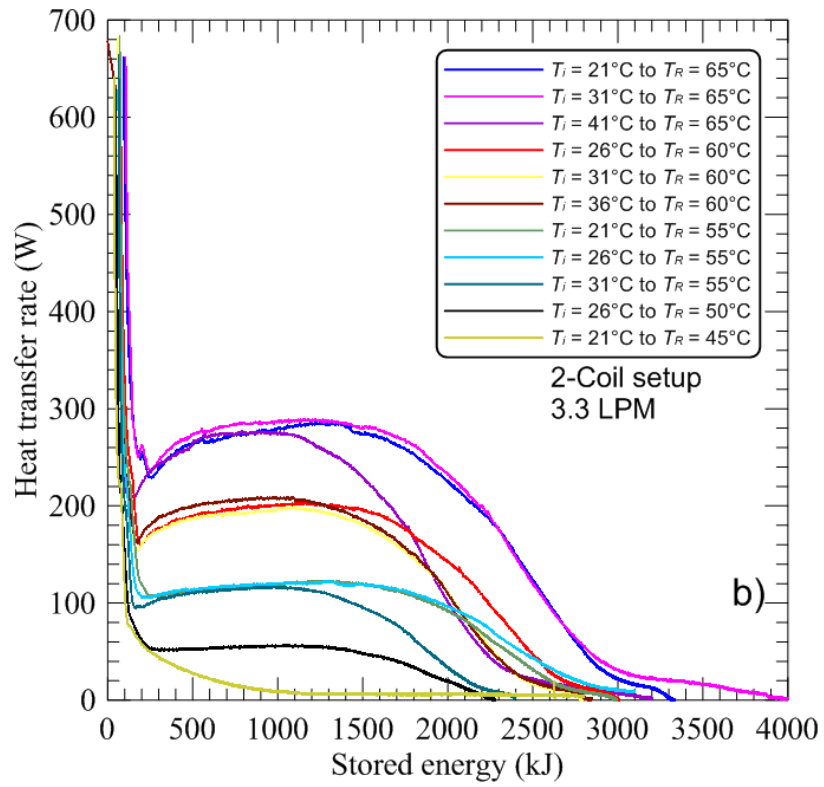
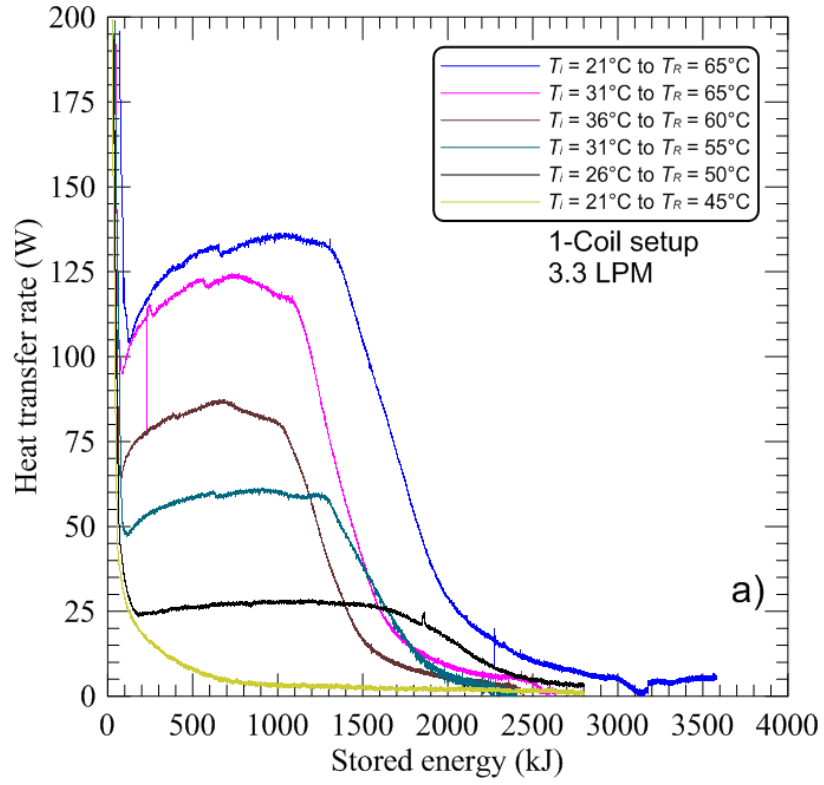
## **4.2 Comparison of experiments using average power obtained over total energy stored/extracted**

All these performed experiments stored different amounts of energy and required different amounts of time for completion. At the end of these experiments, the heat transfer rate decreases very slowly as the driving temperature difference between the PCM and HTF is very low. In such a situation, it is very hard to determine when the experiment has finished precisely. Therefore, it is very difficult to accurately calculate the average heat transfer rate during the entire period of the experiment. On the other hand, at the end of the experiment, the heat transfer rate is very low, total energy stored/removed during the end of the experiment does not change much. Therefore, the end of an experiment can be precisely predicted. Thus, the average heat transfer rate per unit energy stored during the experiment ( $Q_{mean}(E)$ ) can be precisely found. Thus, in this section, the instantaneous heat transfer rate as a function of the stored/extracted energy parameter developed by Lazaro *et al.* (2019) is plotted and the average heat transfer rate per unit stored (or removed) energy is calculated using Eq. (4.1) and different experiments are compared using it.

$$Q_{mean}(E) = \frac{\int_0^E Q(E) dE}{E} \quad (4.1)$$

where  $Q(E)$  is the instantaneous heat transfer rate per unit energy stored and  $E$  is the total energy stored/extracted at the end of an experiment.

Figures 4.5 and 4.6 show the graphs of instantaneous heat transfer rates as a function of cumulative energy stored/extracted from the PCM-TES device during the charging and discharging experiments, respectively. Each of these figures shows three separate graphs obtained for three different coil configurations. These graphs show similar trends as the instantaneous power as a function of time graphs mentioned in Chapter 3. However, they are very different from the instantaneous power as a function of time graphs due to their close-ended nature, *i.e.*, the instantaneous power becomes zero when the PCM-TES device reaches its maximum capacity at a given HTF and initial PCM temperatures. As the maximum energy storing capacity is unique to each experiment conditions, the average power obtained over the maximum energy storing capacity ( $Q_{mean}$ ) is also unique in nature. Therefore, the average power over stored energy can be considered as a fundamental way of determining a comparative average power. And it can be used to compare different coil configurations of the PCM-TES device.



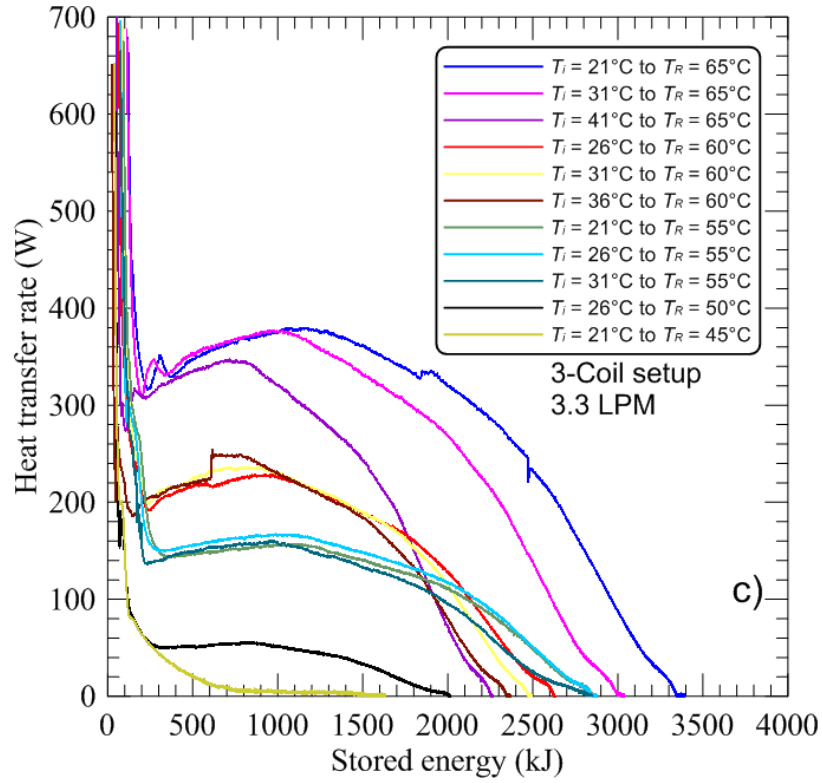
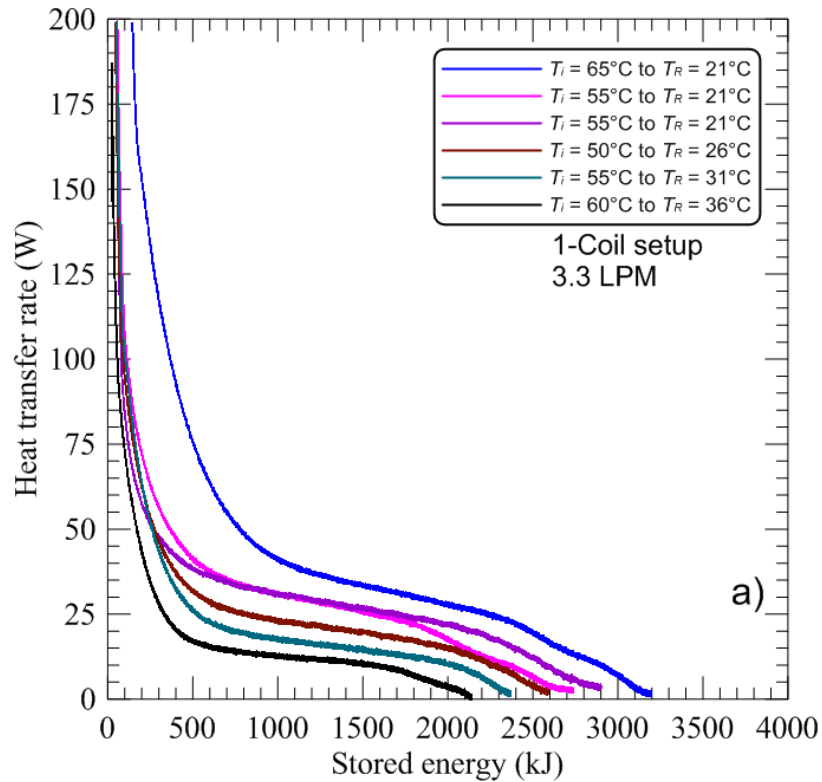


Figure 4.5: Heat transfer rate as a function of stored energy obtained during the charging process of a) 1-coil, b) 2-coil and c) 3-coil setups with a HTF flow rate of 3.3 L/min.





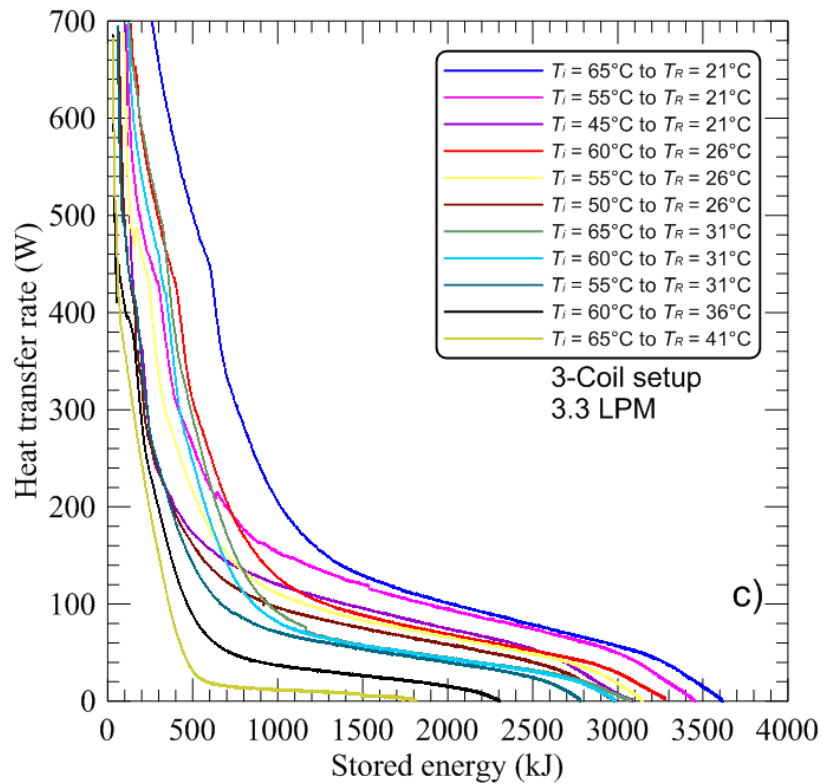
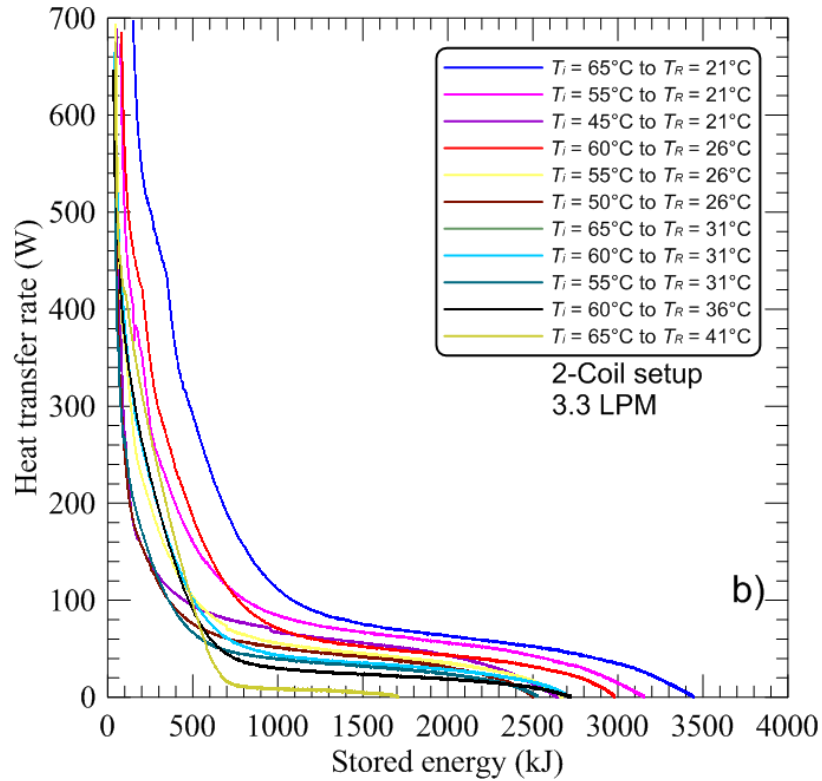


Figure 4.6: Heat transfer rate as a function of extracted energy obtained during the discharging process of a) 1-coil, b) 2-coil and c) 3-coil setups with a HTF flow rate of 3.3 L/min.

Figure 4.7 shows the average power obtained over total stored (or extracted) energy ( $Q_{mean}$ ) as a function of  $Ste_m$  at various  $Ste_r$  obtained during charging and discharging processes at 3.3 L/min HTF flow rate. The graph of instantaneous  $Q_{actual,max}$  is plotted as a function of  $E_{max}$  (defined in Eq. (2.9)) to find the upper limit of uncertainty for the  $Q_{mean}$  values and it is calculated by using the following equation.

$$Q_{mean,upper\ limit}(E_{max}) = \frac{\int_0^{E_{max}} Q_{actual,max}(E_{max}) dE_{max}}{E_{max}} \quad (4.2)$$

Similarly, the graph of instantaneous  $Q_{actual,min}$  is plotted as a function of  $E_{min}$  (defined in Eq. (2.10)) to find the lower limit of uncertainty for the  $Q_{mean}$  values and it is calculated by using the following equation.

$$Q_{mean,lower\ limit}(E_{min}) = \frac{\int_0^{E_{min}} Q_{actual,min}(E_{min}) dE_{min}}{E_{min}} \quad (4.3)$$

The results of this method do not show any better trend than the first method of using average power over a specific time period. However, these results are independent of the time parameter. From Fig. 4.7, it can be observed that the melting results show similar parabolic trends with increasing  $Ste_m$  value as the results obtained for average heat transfer rate over the first 2-hour and 4-hour period graphs. However, in the case of discharging experiments, only the 1-coil setup results show linear trends, whereas the 2-coil and 3-coil setups lack a clear linear trend, and these results overlap with each other. Besides, there is a wider spread in results caused by various initial PCM temperatures, especially during discharging experiments. It suggests that  $Ste_m$  might not be the best marker here to

compare the results and maybe a novel dimensionless number that accounts for both  $Ste$  should be searched.

Also, the uncertainty values obtained at lower  $Ste_m$  values appear larger than the other higher  $Ste_m$  value experiments. This could be explained by the fact that during these experiments, the measured temperature drop in HTF was very small, and thus the percentage error in the measurement was very high. Besides, these uncertainty values appear larger than the one obtained in the first method.

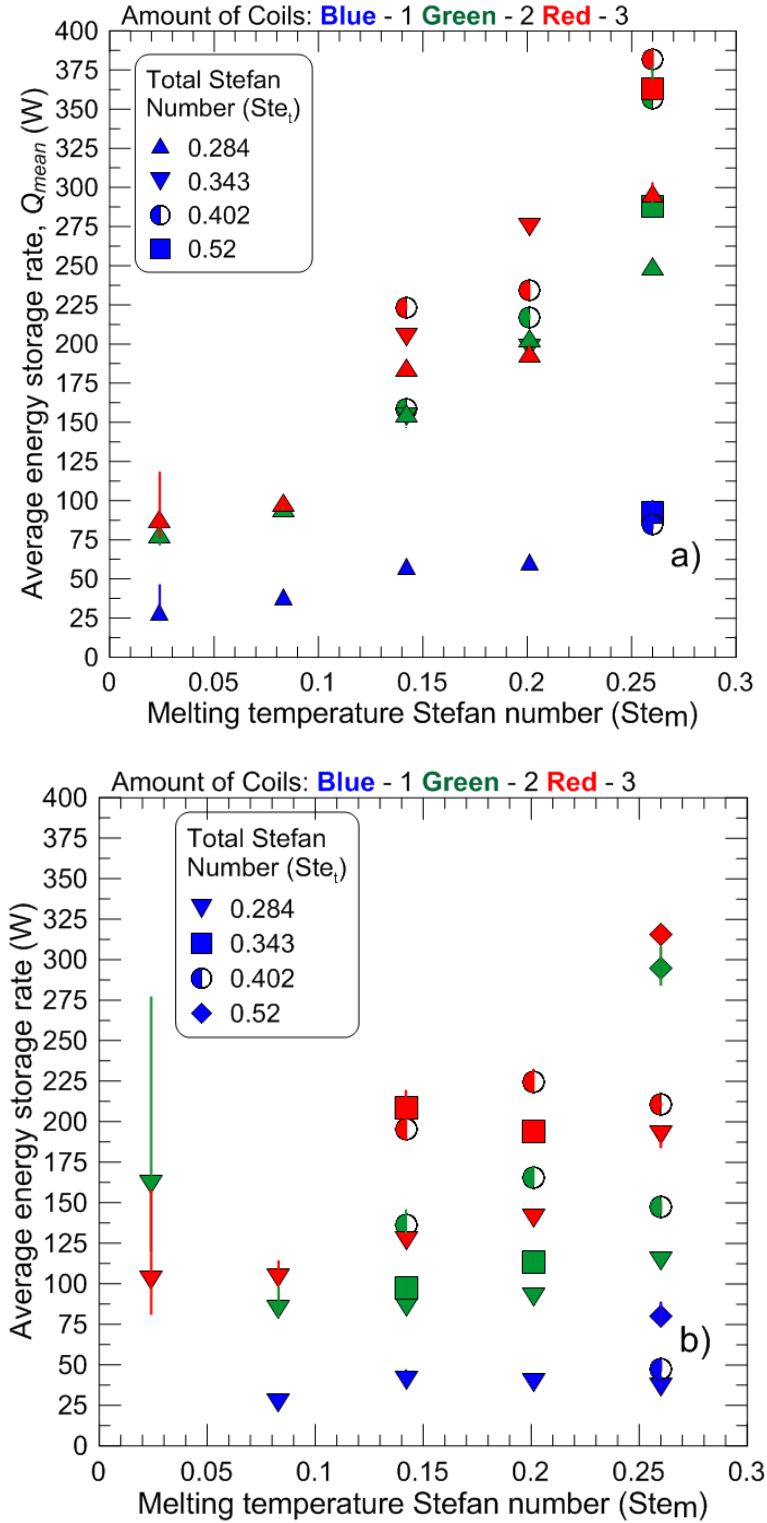


**Figure 4.7: Average power obtained over the entire energy storage capacity as a function of  $Ste_m$  for various  $Ste_t$ , obtained during a) charging and b) discharging processes at 3.3 L/min HTF flow rate.**

### 4.3 Comparison of experiments using normalized average heat transfer rate obtained over total energy stored/extracted

In this section, an attempt is made to compare different charging and discharging experiments independent of their size and operating conditions. For this purpose, the term normalized average power ( $Q_{norm}$ ) developed by Lazaro *et al.* (2019) is used. The  $Q_{norm}$  is defined as the average heat transfer rate obtained over the stored energy ( $Q_{mean}$ ) per unit temperature difference between the HTF and the PCM melting point ( $T_m - T_{HTF}$ ) per unit volume of the PCM used ( $V_{pcm}$ ) and shown in Eq. (4.2).

$$Q_{norm} = \frac{Q_{mean}}{V_{pcm} \cdot |(T_m - T_{HTF})|} \quad (4.2)$$

Figure 4.8 shows the normalized power as a function of  $Ste_m$  at various  $Ste_t$  obtained during charging and discharging processes at 3.3 L/min HTF flow rate. From the figure, it can be seen that the  $Q_{norm}$  values obtained for low  $Ste_m$  values on all coil setups are greatly skewed from the rest of the other experiment values. In these low  $Ste_m$  experiments, the temperature difference between the HTF and PCM melting point is very small. Thus, the heat transfer rate obtained during these experiments is very low and sluggishly decreases in these experiments. Therefore, like time-dependent power curves, it is very hard to accurately predict the total energy stored inside these experiments. Thus, there involves a large error in the calculation of  $Q_{norm}$  values for these experiments. Another possibility could be that these experiments were never completed and some part of the PCM did not undergo phase transformation. As these low  $Ste_m$  results make rest of the graph unreadable, it is better to neglect them and study rest of the results.

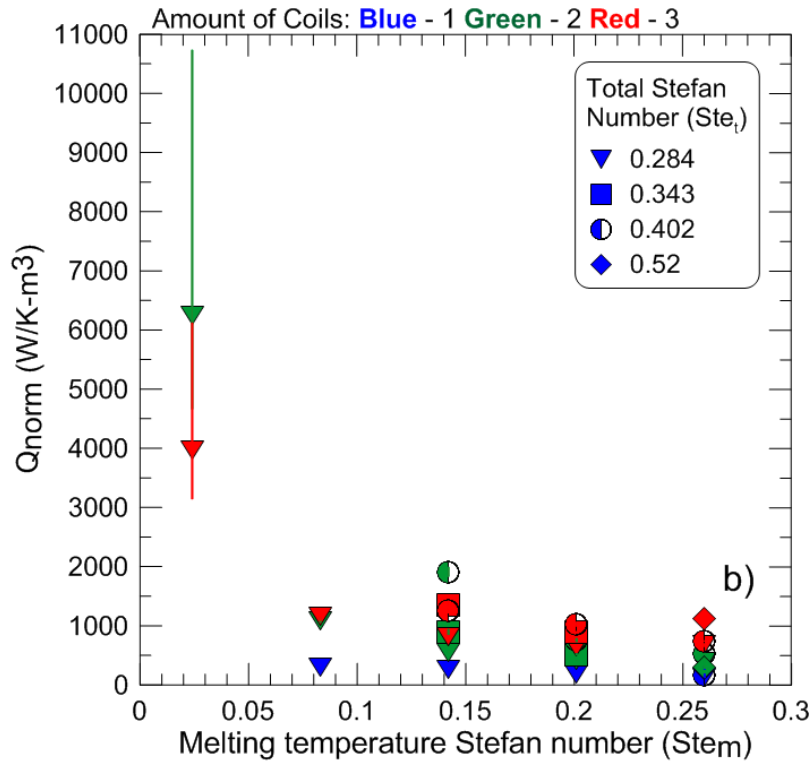
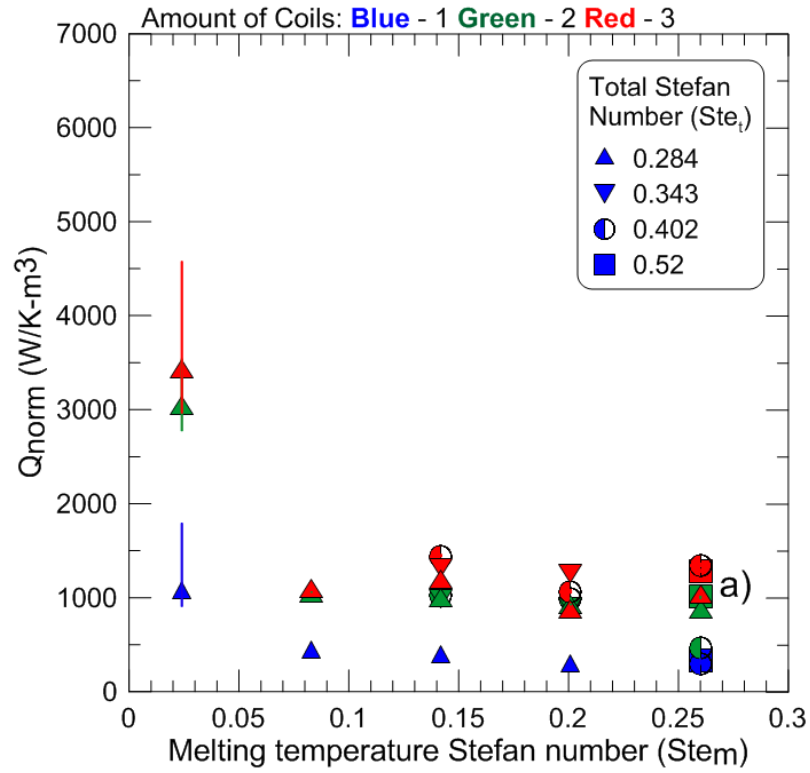


**Figure 4.8: Normalized power ( $Q_{norm}$ ) as a function of  $Stem$  for various  $Ste_t$  obtained during a) charging and b) discharging processes at 3.3 L/min HTF flow rate.**

Figure 4.9 shows the revised graphs of normalized power as a function of  $Ste_m$  at various  $Ste_t$  obtained during charging and discharging processes at 3.3 L/min HTF flow rate. The  $Q_{norm}$  results at low  $Ste_m$  values are excluded from them. From these graphs, it can be observed that the  $Q_{norm}$  values obtained during different charging or discharging experiment increases with the increase in the number of coils used in the PCM-HX. As in the previous two methods, this increase is uniform for the discharging experiments, whereas for charging experiments, this increase in the  $Q_{norm}$  values is not in equal proportion as the difference between the 1-coil and 2-coil setup values is greater than that from the 2-coil to 3-coil setup.

It is observed that the  $Q_{norm}$  values obtained during different charging experiments (except for the lowest  $Ste_m$  experiments) performed on any particular number of coil configurations are close to each other and appear fairly constant for any particular coil configurations. On the other hand, the  $Q_{norm}$  values obtained during different discharging experiments (except the lowest  $Ste_m$  experiments) performed on any particular number of coil configurations have a wider spread than the charging experiments. It shows that dividing average power by the temperature difference plays an important role in defining power for the charging experiment. But in case of discharging experiments, dividing average power by the temperature difference does not lead to the same behaviour as seen in the graph and it appears that for discharging power does not depend in the same way on this temperature difference. Therefore, for the melting experiments, the average  $Q_{norm}$  values with small deviation can be defined for different configurations. However, for solidification experiments, this deviation is large and thus, involves greater uncertainty in calculating the unknown  $Q_{norm}$  value for unformed experiments.

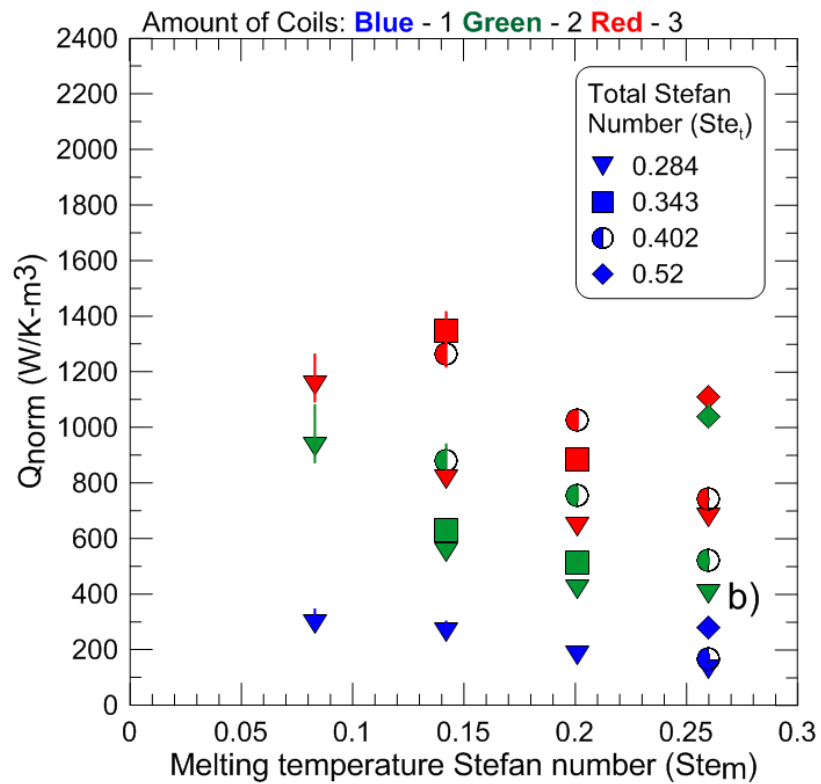
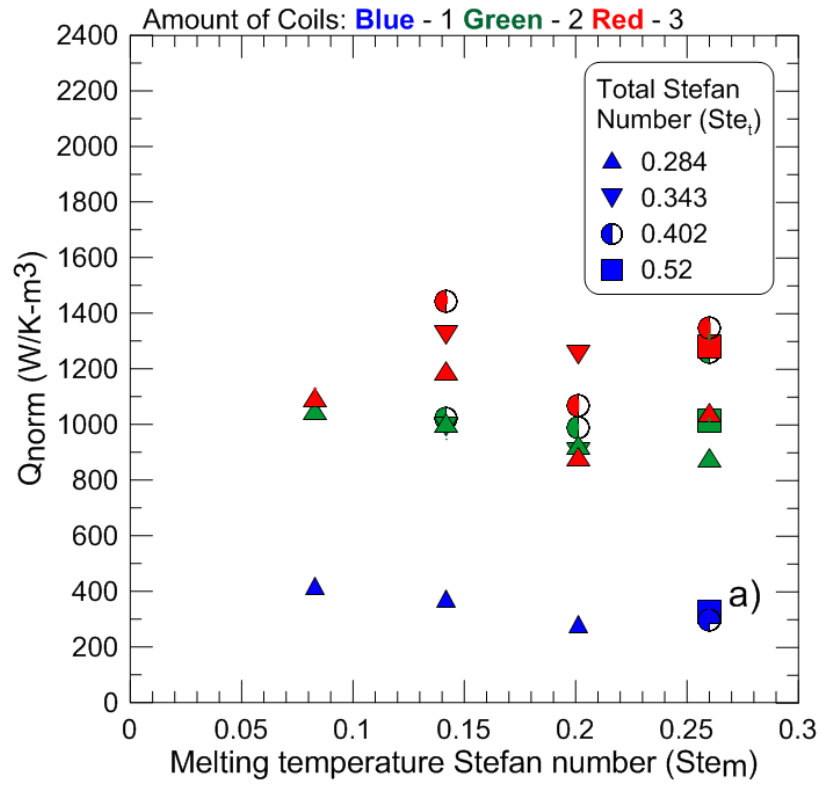


Figure 4.9: Revised graph of normalized power ( $Q_{norm}$ ) as a function of  $Stem$  for various  $Ste_t$  obtained during a) charging and b) discharging processes at 3.3 L/min HTF flow rate.



#### 4.4 Comparison of used data reduction methods

Using the above mentioned three methods of data reduction, the transient results of experiments are shown as a single value. Out of these three methods, in the first method, the average heat transfer rate during a particular time period was calculated. However, each experiment required different time durations for completion. Thus, the results of this method are not unique for the given operating condition of PCM-HX devices and depend on the experiment completion time. Thus, this method is faulty and fails to compare the different experiments accurately.

On the other hand, the results of the second and third method are unique for the given operating conditions of PCM-HX devices and independent of experiment completion time. Thus, these methods could be used to compare different experiments. These obtained results showed particular trends. Therefore, by plotting the best fit line/curve through these results, it could be possible to predict the unknown average power value ( $Q$ ) for any unperformed experiments within the used range of  $Ste_m$ . Thus, these obtained trendlines can help designers to select the operating conditions required to meet the desired average power demanded by their applications.

For example, in Fig. 4.10, three trendlines are plotted on the average power obtained over the entire energy storage capacity as a function of  $Ste_m$  for various  $Ste_t$  (Fig. 4.7 a). If a designer wanted to design a system with 2-coils and required to get an average heat transfer rate of 125 W, from the trendline of the 2-coil setup, the required operating condition (*i.e.* a  $Ste_m$  of 0.115) could be selected. This obtained  $Ste_m$  value could lead to a heat transfer value which would lie within the standard residual error of the trendline.

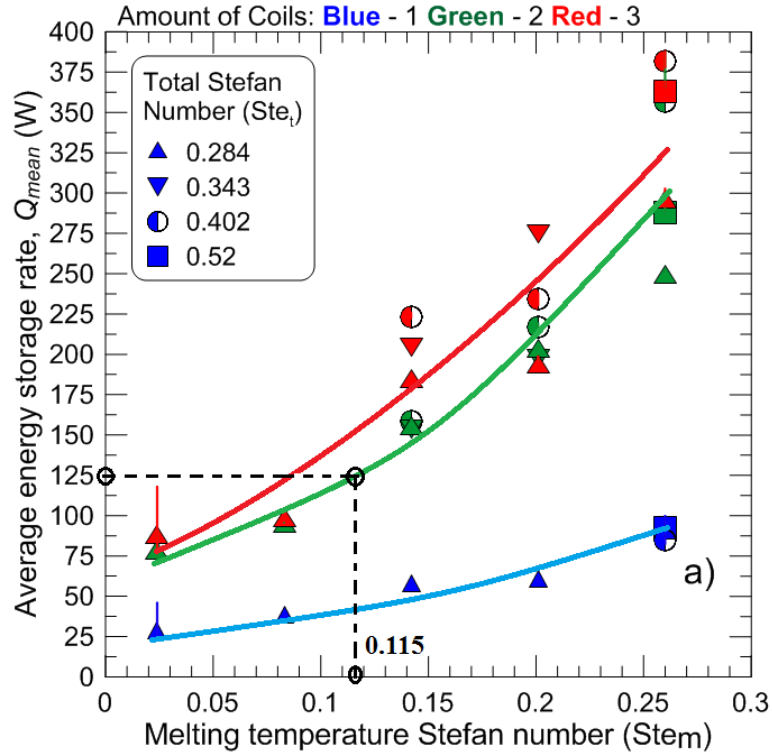


**Figure 4.10: The charging experiment graph of average power obtained over the entire energy storage capacity as a function of  $Ste_m$  for various  $Ste_t$ , with shown result trendlines.**

Now the question arises: which of these two methods (second and third methods) will give the most accurate results? To answer it, the percent deviations of results from their respective trendline points are calculated. While calculating trendlines for the third method, the results at low  $Ste_m$  values are omitted as they are outliers and their consideration significantly outweigh the effect of other result points. The obtained percent deviations from the trendline are shown in Table 4.1. From the table, it can be found that the percent deviation for charging experiments (highlighted in yellow) is lower than the discharging experiment (highlighted in green). Thus, it appears that the charging results can more accurately be predicted (value of  $Q$ ) than the discharging results. Also, the maximum percent deviation obtained for the third method is lower than that of the second method for both charging and discharging experiments.

**Table 4.1: Percent deviation from the trendlines of different data reduction methods.**

Method	Charging Experiment results				Discharging Experiment results			
	1-coil	2-coil	3-coil	Max	1-coil	2-coil	3-coil	Max
<b>2</b>	8.1 %	9.5 %	14.7 %	14.7 %	27.9 %	41.5 %	47.7 %	47.7 %
<b>3</b>	7.2 %	9.4 %	14.1 %	14.1 %	28.9 %	34.5 %	30.3 %	34.5 %

However, the difference between the percent deviations of these two methods is negligible in the case of charging, whereas this difference is significant in the case of discharging. Thus, it can be said that the results obtained using the third method trendline will be more accurate than the results obtained using the second method.

Also, in the third method, the average power is divided by the temperature difference between the HTF temperature and the PCM melting point. Therefore, the  $Q_{norm}$  values obtained for any particular coil configuration could be a constant and independent of  $St_m$  values. Therefore, the results obtained using the third method can also be expressed as a constant value with a certain amount of deviation. Therefore, it is worth to calculate the average  $Q_{norm}$  values obtained from the experiments and determine the range of deviation from the results. The percent deviations from the mean  $Q_{norm}$  values calculated for all configurations during charging and discharging is shown in Table 4.2. The maximum percent deviations obtained for charging is 16.6 and discharging is 33.9. Therefore, using this constant value approach,  $Q_{norm}$  values can also be more accurately predicted for charging than the discharging experiments. Also, these deviations are in the same range as the deviations obtained using the trendline approach for the third method. Therefore, the constant  $Q_{norm}$  value approach is equally valid along with the trendline approach.

**Table 4.2: The mean  $Q_{norm}$  values and their percent standard deviation for different configurations of PCM-HX.**

PCM-HX configuration	Mean $Q_{norm}$ value (W/K-m <sup>3</sup> )		Percent deviation from the mean value	
	Charging	Discharging	During Charging	During Discharging
1-coil	333.5	218	<b>16.6 %</b>	31.7 %
2-coil	1003.6	663.6	10.5 %	<b>33.9 %</b>
3-coil	1192	965	14.1 %	25.9 %

Just by multiplying the  $Q_{norm}$  value of any particular used configuration with the  $\Delta T$  used in the application, designers could predict an order of magnitude of their system's heat transfer rate per unit volume within the above-mentioned percent deviations.

#### **4.5 Chapter conclusion**

In this chapter, an attempt is made to reduce the transient heat transfer data of different experiments into time-independent heat transfer averages that could be used to compared different systems operating under different conditions. For this, three different methods are used in this chapter.

In the first method, the average heat transfer rate over the first 2 and 4 hours duration of the experiments are used for the comparison. However, the different experiments required different time periods for their completion, and there was a significant uncertainty associated with determining the end of experiments. Therefore, a second method is used in which the average heat transfer rate over total energy stored/extracted during experiments is calculated and compared. The results obtained using this method were independent of experimental time and showed a similar trend as the first method results.

The average heat transfer rate increased parabolically for charging experiments with respect to  $Ste_m$ , whereas for the discharging experiments, this trend was a linear increase. In the third method, normalized power ( $Q_{norm}$ ) is calculated. It includes the effect of used PCM amount (through the volume) and the temperature difference between the HTF and PCM melting point. Also, the obtained results are independent of time.

Out of these three methods, the first method should not be used for the experiment comparison as the results were not unique for an experiment and depended on the arbitrary time period chosen to calculate it. On the other hand, the remaining two methods, the second and third methods, can be used to compare the different experiments as their results were unique to the experiments and did not depend on the experiment completion time. By plotting trend line through the results of these two methods, unknown  $Q$  value can be obtained any  $Ste_m$  value within the range of  $Ste_m$  values used in this study. The percent deviations from the trendlines of these two methods showed that results predicted using the third method have less error than the second method. Thus, the third method is the best method for the comparison of different experiments.

Also, it is checked if  $Q_{norm}$  values can be expressed as constant value with a certain deviation in the results for specific PCM-HX setup. It is observed that this approach is valid and  $Q_{norm}$  values can be considered constant for a given coil configuration. Using this value, designers can predict the performance of that PCM-HX device at different operating conditions.

## **Chapter 5: Conclusion and future work**

In order to address the challenge of global warming and environmental pollution, it is necessary to reduce the dependence of human society on fossil fuels as a major energy source and increase the use of clean energy technologies like solar, wind and tidal energy. However, the availability of these clean energy sources varies largely depending on the time of the day, the season of the year and weather conditions. Thus, there is a gap between renewable energy generation and consumer demand. To bridge this gap, there is a need for thermal energy sources. Out of different types of thermal energy storage technologies, latent heat storage technology and especially solid-liquid transition involved LHS devices appears very promising due to their high energy storage density and narrow operating temperature range. In these devices, heat is stored in the form of latent heat of the PCM so it operates at a lower temperature than the conventional SHS devices. However, the common PCMs used in these devices have very low thermal conductivity, which leads to the heat transfer rate problem in PCM-TES. As a consequence, it takes longer to store and extract heat from these devices, which makes them impractical for high energy rate demanding applications.

To address this rate problem, researchers came up with many designs of PCM-TES. These designs vary from simple basic shell-and-tube configurations to use of multitube-in-shell and triplex tube configurations. Some designs incorporated fins on the inner tube of these designs. In some designs, PCM is encapsulated in rectangular or spherical modules and HTF passes over these modules. The variety of these designs is endless. However, there are hardly any studies comparing the performance of these different designs. Also, unlike conventional heat exchangers where two steady-state fluids exchange heat with each other,

in the PCM-TES devices, heat is exchanged between a steady flow of HTF and stationary mass of PCM undergoing a phase change process. Therefore, the heat exchange process within the PCM-TES devices is highly transient and unpredictable. There is no proper guideline available for designing such devices. Hence, selecting the most efficient PCM-TES design and building a right-sized one for a given application is a very challenging task.

In this work, a coil-and shell PCM-TES device filled with dodecanoic acid was built. By changing the number of coils inside the device, three different configurations, namely 1-coil, 2-coil and 3-coil setups, were made. An experimental setup was built to conduct different experiments. The HTF flow rate, inlet and outlet temperatures were varied and recorded, which provided the instantaneous heat transfer rates during different experiments. The experiments performed were categorized into 3 groups, namely 1) equivalent energy experiment, 2) same initial PCM temperature experiment and 3) symmetrical temperature experiments and from their results the following observations were made.

- Heat transfer rate increases with the increasing number of coils inside the device, which leads to a reduction in the experiment completion time.
- HTF temperature has a great effect on the heat transfer rate, whereas the heat transfer rate is slightly affected by the change in the initial temperature of the PCM.
- For the same  $Ste_m$  value, the charging experiments had higher heat transfer rates than the discharging experiments.
- The change in HTF flow rate had a negligible effect for the charging experiments. It had no effect on the discharging experiments.

In order to develop design guidelines, it is required to quantify the effect of above-mentioned parameters. One approach is to convert the obtained transient heat transfer result into single time-independent metrics. Three methods were used to reduce the transient data into a time-independent quantity.

1. The average heat transfer rate during the first 2 and 4 hours was calculated and plotted as a function of  $Ste_m$  at various  $Ste_t$  values.
2. The instantaneous heat transfer rate was plotted as a function of cumulative energy stored/extracted during the experiment and the average heat transfer rate per unit stored energy was then calculated and plotted as a function of  $Ste_m$  at various  $Ste_t$  values.
3. Normalized power was calculated and plotted as a function of  $Ste_m$  at various  $Ste_t$  values.

The results of the first two methods showed similar trends. The average heat transfer rate increased with increasing  $Ste_m$  value. For charging experiments, this trend was parabolic, whereas for discharging experiments, it was a linear increase. Also, the same  $Ste_m$  discharging experiments with different initial temperatures, the results were wide spread. Therefore, it suggests that  $Ste_m$  alone is not a good marker for comparison. A new variable combining both Ste numbers would be a better solution. The results of third method looked pretty much constant with certain deviations. For the charging experiments, these deviations were smaller, whereas for the discharging experiments, the results were widespread and had larger deviations.

Out of these three methods, the results of first method were dependant on the experiment completion time and were not unique for given operating conditions and geometry. Thus,



this method cannot be used in the experiment comparison process. On the other hand, the results of second and third method were unique for given operating conditions and geometry and were independent of experiment completion time. Thus, these two methods can be used for the comparison study. Using the second and third method, unknown  $Q$  value for different operating conditions can be found, provided experiment  $Ste_m$  lies within the range of  $Ste_m$  used in this study. This way, by referring to the results of these methods, designers can predict the performance of their system without actually performing the experiment.

The percent deviations of results from the trend lines of these two methods were calculated and compared. After comparison, it was found that the second method results had a greater deviation than the third method results. Thus, it is concluded that using the third method; unknown experiment results can be more accurately predicted.

Also, the validity of constant  $Q_{norm}$  value for any specific configuration approach is tested by calculating mean and the percent standard deviation from the mean  $Q_{norm}$  values. The percent deviations were in the range of trendline approach. Therefore, it is found  $Q_{norm}$  values for any specific configuration can be considered constant with some deviation. Using this value, designers can predict the performance of their system without actually performing the experiments.

## **Future Scope**

The first step in future work would be to perform additional experimental characterization using the PCM-HX described in this work, but for temperatures (both HTF and initial) that are different than the ones used and presented in this work. The results of this additional

experimental work could be used to verify the validation of the heat transfer rate prediction presented in Chapter 4.

The coils used in this study had six passes. By changing the number of passes, the coil area changes and so could the heat transfer rates. Thus, 4 and 8 pass coils could be manufactured, and similar experiments could be conducted to observe the effect of the number of passes. With those results, a similar analysis could be done, the results added to the ones obtained in this work to further look at methods of reducing the data.

Also, during this study, the size of PCM-HX has not changed. By building different sized coil-and-shell PCM-HXs, the effect of PCM volume on  $Q_{norm}$  values can be actually studied. This comparison of different sizes will determine if the third method, *i.e.* finding  $Q_{norm}$ , actually works in comparing different sized systems.

Again, work has already done on a system of roughly the same size using finned tubes. Therefore, the data from both studies can be compiled together to see how the comparative methods used here will work on systems with two different heat exchangers.

## References

- Abdulateef, A. M., J. Abdulateef, S. Mat, K. Sopian, B. Elhub and M. A. Mussa (2018). "Experimental and numerical study of solidifying phase-change material in a triplex-tube heat exchanger with longitudinal/triangular fins." International Communications in Heat and Mass Transfer **90**: 73-84.
- Abdulateef, A. M., S. Mat, J. Abdulateef, K. Sopian and A. A. Al-Abidi (2018). "Geometric and design parameters of fins employed for enhancing thermal energy storage systems: a review." Renewable and Sustainable Energy Reviews **82**: 1620-1635.
- Abdulateef, A. M., S. Mat, K. Sopian, J. Abdulateef and A. A. Gitan (2017). "Experimental and computational study of melting phase-change material in a triplex tube heat exchanger with longitudinal/triangular fins." Solar Energy **155**: 142-153.
- Agyenim, F. (2016). "The use of enhanced heat transfer phase change materials (PCM) to improve the coefficient of performance (COP) of solar powered LiBr/H<sub>2</sub>O absorption cooling systems." Renewable Energy **87**: 229-239.
- Agyenim, F., P. Eames and M. Smyth (2010). "Heat transfer enhancement in medium temperature thermal energy storage system using a multitube heat transfer array." Renewable Energy **35**(1): 198-207.
- Ahmadi, R., M. J. Hosseini, A. A. Ranjbar and R. Bahrampoury (2018). "Phase change in spiral coil heat storage systems." Sustainable Cities and Society **38**: 145-157.
- Akgun, M., O. Aydin and K. Kaygusuz (2007). "Experimental study on melting/solidification characteristics of a paraffin as PCM." Energy Conversion and Management **48**(2): 669-678.
- Akhmat, G., K. Zaman, T. Shukui and F. Sajjad (2014). "Does energy consumption contribute to climate change? Evidence from major regions of the world." Renewable and Sustainable Energy Reviews **36**: 123-134.
- Al-Abidi, A. A., S. Mat, K. Sopian, M. Y. Sulaiman and A. T. Mohammad (2013). "Internal and external fin heat transfer enhancement technique for latent heat thermal energy storage in triplex tube heat exchangers." Applied Thermal Engineering **53**(1): 147-156.
- Al-Abidi, A. A., S. Mat, K. Sopian, M. Y. Sulaiman and A. T. Mohammad (2013). "Numerical study of PCM solidification in a triplex tube heat exchanger with internal and external fins." International Journal of Heat and Mass Transfer **61**: 684-695.
- Almsater, S., A. Alemu, W. Saman and F. Bruno (2017). "Development and experimental validation of a CFD model for PCM in a vertical triplex tube heat exchanger." Applied Thermal Engineering **116**: 344-354.
- Amin, N. A. M., M. Belusko and F. Bruno (2014). "An effectiveness-NTU model of a packed bed PCM thermal storage system." Applied Energy **134**: 356-362.
- Amin, N. A. M., F. Bruno and M. Belusko (2012). "Effectiveness-NTU correlation for low temperature PCM encapsulated in spheres." Applied Energy **93**: 549-555.

- Archibold, A. R., J. Gonzalez-Aguilar, M. M. Rahman, D. Yogi Goswami, M. Romero and E. K. Stefanakos (2014). "The melting process of storage materials with relatively high phase change temperatures in partially filled spherical shells." Applied Energy **116**: 243-252.
- Ardahaie, S. S., M. J. Hosseini, A. A. Ranjbar and M. Rahimi (2019). "Energy storage in latent heat storage of a solar thermal system using a novel flat spiral tube heat exchanger." Applied Thermal Engineering **159**: 113900.
- Assis, E., L. Katsman, G. Ziskind and R. Letan (2007). "Numerical and experimental study of melting in a spherical shell." International Journal of Heat and Mass Transfer **50**(9-10): 1790-1804.
- Azad, M., D. Groulx and A. Donaldson (2019). Experimental Study of Natural Convection Onset during Phase Change Material Melting. Eurotherm 2019. Lleida, Spain: 10 p.
- Aziz, S., N. A. M. Amin, M. S. Abdul Majid, F. Bruno and M. Belusko (2018). "Effectiveness-NTU correlation for a TES tank comprising a PCM encapsulated in a sphere with heat transfer enhancement." Applied Thermal Engineering **143**: 1003-1010.
- Baby, R. and C. Balaji (2012). "Experimental investigations on phase change material based finned heat sinks for electronic equipment cooling." International Journal of Heat and Mass Transfer **55**(5-6): 1642-1649.
- Bastani, A., F. Haghghat and J. Kozinski (2014). "Designing building envelope with PCM wallboards: Design tool development." Renewable and Sustainable Energy Reviews **31**: 554-562.
- Belusko, M., N. H. S. Tay, M. Liu and F. Bruno (2015). "Effective tube-in-tank PCM thermal storage for CSP applications, Part 1: Impact of tube configuration on discharging effectiveness." Solar Energy **139**: 733-743.
- Bénard, C., D. Gobin and F. Martinez (1985). "Melting in rectangular enclosures: experiments and numerical simulations." Journal of Heat Transfer **107**(4): 794-803.
- Bilir, L. and Z. İlken (2005). "Total solidification time of a liquid phase change material enclosed in cylindrical/spherical containers." Applied Thermal Engineering **25**(10): 1488-1502.
- Cabeza, L. F., G. Svensson, S. Hiebler and H. Mehling (2003). "Thermal performance of sodium acetate trihydrate thickened with different materials as phase change energy storage material." Applied Thermal Engineering **23**(13): 1697-1704.
- Campos-Celador, Á., G. Diarce, J. T. Zubiaga, T. V. Bandos, A. M. García-Romero, L. M. López and J. M. Sala (2014). "Design of a Finned Plate Latent Heat Thermal Energy Storage System for Domestic Applications." Energy Procedia **48**: 300-308.
- Castell, A., M. Belusko, F. Bruno and L. F. Cabeza (2011). "Maximisation of heat transfer in a coil in tank PCM cold storage system." Applied Energy **88**(11): 4120-4127.
- Castell, A. and C. Solé (2015). "An overview on design methodologies for liquid–solid PCM storage systems." Renewable and Sustainable Energy Reviews **52**: 289-307.

- Chen, C., H. Zhang, X. Gao, T. Xu, Y. Fang and Z. Zhang (2016). "Numerical and experimental investigation on latent thermal energy storage system with spiral coil tube and paraffin/expanded graphite composite PCM." Energy Conversion and Management **126**: 889-897.
- Delgado, M., A. Lázaro, J. Mazo and B. Zalba (2012). "Review on phase change material emulsions and microencapsulated phase change material slurries: Materials, heat transfer studies and applications." Renewable and Sustainable Energy Reviews **16**(1): 253-273.
- Desgrosseilliers, L., C. A. Whitman, D. Groulx and M. A. White (2013). "Dodecanoic acid as a promising phase-change material for thermal energy storage." Applied Thermal Engineering **53**: 37-41.
- Eames, I. W. and K. T. Adref (2002). "Freezing and melting of water in spherocal enclosures of the type used in thermal (ice) storage systems." Applied Thermal Engineering **22**: 733-745.
- Ermis, K., A. Ereğ and I. Dincer (2007). "Heat transfer analysis of phase change process in a finned-tube thermal energy storage system using artificial neural network." International Journal of Heat and Mass Transfer **50**(15-16): 3163-3175.
- Esaipour, M., M. J. Hosseini, A. A. Ranjbar and R. Bahrampoury (2016). "Numerical study on geometrical specifications and operational parameters of multi-tube heat storage systems." Applied Thermal Engineering **109**: 351-363.
- Esaipour, M., M. J. Hosseini, A. A. Ranjbar, Y. Pahamli and R. Bahrampoury (2016). "Phase change in multi-tube heat exchangers." Renewable Energy **85**: 1017-1025.
- Fan, L.-W., X. Fang, X. Wang, Y. Zeng, Y.-Q. Xiao, Z.-T. Yu, X. Xu, Y.-C. Hu and K.-F. Cen (2013). "Effects of various carbon nanofillers on the thermal conductivity and energy storage properties of paraffin-based nanocomposite phase change materials." Applied Energy **110**: 163-172.
- Fang, M. and G. Chen (2007). "Effects of different multiple PCMs on the performance of a latent thermal energy storage system." Applied Thermal Engineering **27**(5-6): 994-1000.
- Fang, Y., J. Niu and S. Deng (2019). "An analytical technique for the optimal designs of tube-in-tank thermal energy storage systems using PCM." International Journal of Heat and Mass Transfer **128**: 849-859.
- Gasia, J., J. Diriken, M. Bourke, J. Van Bael and L. F. Cabeza (2017). "Comparative study of the thermal performance of four different shell-and-tube heat exchangers used as latent heat thermal energy storage systems." Renewable Energy **114**: 934-944.
- Gau, C. and R. Viskanta (1986). "Melting and solidification of a pure metal on a vertical wall." J. Heat Transfer **108**(1): 174-181.
- Groulx, D. (2015). Numerical study of nano-enhanced PCMs: are they worth it? . 1st Thermal and Fluid Engineering Summer Conference, TFESC. New York City, USA: 15 p.

- Groulx, D. (2018). The rate problem in solid-liquid phase change heat transfer: efforts and questions towards heat exchanger design rules. 16th International Heat Transfer Conference, IHTC-16. Beijing, China: 16 p.
- Groulx, D., A. C. Kheirabadi, L. Desgrosseilliers, M. Kabbara, M. Azad, A. Donaldson, A. Joseph and M. A. White (2016). Working Towards Solving the Rate Problem: Geometric vs Nano-Enhanced PCM Solutions. INNOSTORAGE Conference Ben-Gurion University of the Negev, Israel: 4 p.
- He, M., L. Yang, W. Lin, J. Chen, X. Mao and Z. Ma (2019). "Preparation, thermal characterization and examination of phase change materials (PCMs) enhanced by carbon-based nanoparticles for solar thermal energy storage." Journal of Energy Storage **25**: 100874.
- Herbinger, F., A. Patil and D. Groulx (2019). Characterization of Different Geometrical Variations of a Vertical Finned Tube-and-Shell Heat Exchanger. Eurotherm 2019. Lleida, Spain: 10 p.
- Herbinger, F., J. Skaalum and D. Groulx (2018). Experimental Study of a Latent Storage System using Vertical-Finned Tube and Shell Heat Exchanger: Early Results. 3rd Thermal and Fluids Engineering Conference (TFEC). Fort Lauderdale, FL, USA: 4 p.
- Ho, C. J. and R. Viskanta (1984). "Heat-Transfer during Inward Melting in a Horizontal Tube." International Journal of Heat and Mass Transfer **27**(5): 705-716.
- Ho, C. J. and R. Viskanta (1984). "Inward solid-liquid phase-change heat transfer in a rectangular cavity with conducting vertical walls." International Journal of Heat and Mass Transfer **27**(7): 1055-1065.
- Hosseini, M. J., M. Rahimi and R. Bahrapoury (2014). "Experimental and computational evolution of a shell and tube heat exchanger as a PCM thermal storage system." International Communications in Heat and Mass Transfer **50**: 128-136.
- Huang, X., Y. Lin, G. Alva and G. Fang (2017). "Thermal properties and thermal conductivity enhancement of composite phase change materials using myristyl alcohol/metal foam for solar thermal storage." Solar Energy Materials and Solar Cells **170**: 68-76.
- International Energy Agency (IEA) (2016). Key World Energy Statistics 2016.
- Izquierdo-Barrientos, M. A., C. Sobrino and J. A. Almendros-Ibáñez (2016). "Modeling and experiments of energy storage in a packed bed with PCM." International Journal of Multiphase Flow **86**: 1-9.
- Jin, H.-Q., L.-W. Fan, M.-J. Liu, Z.-Q. Zhu and Z.-T. Yu (2017). "A pore-scale visualized study of melting heat transfer of a paraffin wax saturated in a copper foam: Effects of the pore size." International Journal of Heat and Mass Transfer **112**: 39-44.
- Jung, E. G. and J. H. Boo (2014). "Thermal analytical model of latent thermal storage with heat pipe heat exchanger for concentrated solar power." Solar Energy **102**: 318-332.
- Kabbara, M. (2015). Real Time Solar and Controlled Experimental Investigation of a Latent Heat Energy Storage System. M.A.Sc, Dalhousie University, 156 p.

- Karami, R. and B. Kamkari (2019). "Investigation of the effect of inclination angle on the melting enhancement of phase change material in finned latent heat thermal storage units." Applied Thermal Engineering **146**: 45-60.
- Kazemi, M., M. J. Hosseini, A. A. Ranjbar and R. Bahrampoury (2018). "Improvement of longitudinal fins configuration in latent heat storage systems." Renewable Energy **116**: 447-457.
- Kibria, M. A., M. R. Anisur, M. H. Mahfuz, R. Saidur and I. H. S. C. Metselaar (2015). "A review on thermophysical properties of nanoparticle dispersed phase change materials." Energy Conversion and Management **95**: 69-89.
- Kim, K.-b., K.-w. Choi, Y.-j. Kim, K.-h. Lee and K.-s. Lee (2010). "Feasibility study on a novel cooling technique using a phase change material in an automotive engine." Energy **35**(1): 478-484.
- Kok, B. (2020). "Examining effects of special heat transfer fins designed for the melting process of PCM and Nano-PCM." Applied Thermal Engineering **170**: 114989.
- Koukou, M. K., M. G. Vrachopoulos, N. S. Tachos, G. Dogkas, K. Lymperis and V. Stathopoulos (2018). "Experimental and computational investigation of a latent heat energy storage system with a staggered heat exchanger for various phase change materials." Thermal Science and Engineering Progress **7**: 87-98.
- Kousha, N., M. Rahimi, R. Pakrouh and R. Bahrampoury (2019). "Experimental investigation of phase change in a multitube heat exchanger." Journal of Energy Storage **23**: 292-304.
- Lakhani, S., A. Raul and S. K. Saha (2017). "Dynamic modelling of ORC-based solar thermal power plant integrated with multitube shell and tube latent heat thermal storage system." Applied Thermal Engineering **123**: 458-470.
- Lazaro, A., M. Delgado, A. König-Haagen, S. Höhlelein and G. Diarce3 (2019). Technical performance assesment of phase change material components. . ISES conference: 12 p.
- Lazaro, A., P. Dolado, J. M. Marin and B. Zalba (2009). "PCM-air heat exchangers for free-cooling applications in buildings: Empirical model and application to design." Energy Conversion and Management **50**(3): 444-449.
- Li, W. Q., Z. G. Qu, Y. L. He and W. Q. Tao (2012). "Experimental and numerical studies on melting phase change heat transfer in open-cell metallic foams filled with paraffin." Applied Thermal Engineering **37**: 1-9.
- Lin, Y., Y. Jia, G. Alva and G. Fang (2018). "Review on thermal conductivity enhancement, thermal properties and applications of phase change materials in thermal energy storage." Renewable and Sustainable Energy Reviews **82**: 2730-2742.
- Lissner, M., J. Tissot, D. Leducq, K. Azzouz and L. Fournaison (2016). "Performance study of latent heat accumulators: Numerical and experimental study." Applied Thermal Engineering **102**: 604-614.

- Liu, C. and D. Groulx (2014). "Experimental study of the phase change heat transfer inside a horizontal cylindrical latent heat energy storage system." International Journal of Thermal Sciences **82**: 100-110.
- Liu, Y., J. Duan, X. He and Y. Wang (2018). "Experimental investigation on the heat transfer enhancement in a novel latent heat thermal storage equipment." Applied Thermal Engineering **142**: 361-370.
- Lizana, J., R. Chacartegui, A. Barrios-Padura and J. M. Valverde (2017). "Advances in thermal energy storage materials and their applications towards zero energy buildings: A critical review." Applied Energy **203**: 219-239.
- Longeon, M., A. Soupart, J.-F. Fourmigué, A. Bruch and P. Marty (2013). "Experimental and numerical study of annular PCM storage in the presence of natural convection." Applied Energy **112**: 175-184.
- López-Navarro, A., J. Biosca-Taronger, J. M. Corberán, C. Peñalosa, A. Lázaro, P. Dolado and J. Payá (2014). "Performance characterization of a PCM storage tank." Applied Energy **119**: 151-162.
- Mahdi, J. M., S. Lohrasbi, D. D. Ganji and E. C. Nsofor (2018). "Accelerated melting of PCM in energy storage systems via novel configuration of fins in the triplex-tube heat exchanger." International Journal of Heat and Mass Transfer **124**: 663-676.
- Mahdi, J. M. and E. C. Nsofor (2018). "Solidification enhancement of PCM in a triplex-tube thermal energy storage system with nanoparticles and fins." Applied Energy **211**: 975-986.
- Medrano, M., M. O. Yilmaz, M. Nogués, I. Martorell, J. Roca and L. F. Cabeza (2009). "Experimental evaluation of commercial heat exchangers for use as PCM thermal storage systems." Applied Energy **86**(10): 2047-2055.
- Murray, R. E. and D. Groulx (2014). "Experimental study of the phase change and energy characteristics inside a cylindrical latent heat energy storage system: Part 1 consecutive charging and discharging." Renewable Energy **62**: 571-581.
- Nallusamy, N., S. Sampath and R. Velraj (2007). "Experimental investigation on a combined sensible and latent heat storage system integrated with constant/varying (solar) heat sources." Renewable Energy **32**(7): 1206-1227.
- Nazir, H., M. Batool, F. J. Bolivar Osorio, M. Isaza-Ruiz, X. Xu, K. Vignarooban, P. Phelan, Inamuddin and A. M. Kannan (2019). "Recent developments in phase change materials for energy storage applications: A review." International Journal of Heat and Mass Transfer **129**: 491-523.
- Noël, J., S. Kahwaji, L. Desgrosseilliers, D. Groulx and M. A. White (2016). Phase Change Materials. Chapter in Storing Energy with Special Reference to Renewable Energy Sources, LETCHERENGLISH: 249-271.



- Pahamli, Y., M. J. Hosseini, A. A. Ranjbar and R. Bahrampoury (2016). "Analysis of the effect of eccentricity and operational parameters in PCM-filled single-pass shell and tube heat exchangers." Renewable Energy **97**: 344-357.
- Pakrouh, R., M. J. Hosseini, A. A. Ranjbar and R. Bahrampoury (2017). "Thermodynamic analysis of a packed bed latent heat thermal storage system simulated by an effective packed bed model." Energy **140**: 861-878.
- Pal, D. and Y. Joshi (2001). "Melting in a side heated tall enclosure by a uniformly dissipating heat source." International Journal of Heat and Mass Transfer **44**: 375-387.
- Parameshwaran, R., P. Dhamodharan and S. Kalaiselvam (2013). "Study on thermal storage properties of hybrid nanocomposite-dibasic ester as phase change material." Thermochimica Acta **573**: 106-120.
- Pardo, P., A. Deydier, Z. Anxionnaz-Minvielle, S. Rougé, M. Cabassud and P. Cognet (2014). "A review on high temperature thermochemical heat energy storage." Renewable and Sustainable Energy Reviews **32**: 591-610.
- Pielichowska, K. and K. Pielichowski (2014). "Phase change materials for thermal energy storage." Progress in Materials Science **65**: 67-123.
- Pizzolato, A., A. Sharma, K. Maute, A. Sciacovelli and V. Verda (2017). "Design of effective fins for fast PCM melting and solidification in shell-and-tube latent heat thermal energy storage through topology optimization." Applied Energy **208**: 210-227.
- Praveen, B. and S. Suresh (2018). "Experimental study on heat transfer performance of neopentyl glycol/CuO composite solid-solid PCM in TES based heat sink." Engineering Science and Technology, an International Journal **21**(5): 1086-1094.
- Qureshi, Z. A., H. M. Ali and S. Khushnood (2018). "Recent advances on thermal conductivity enhancement of phase change materials for energy storage system: A review." International Journal of Heat and Mass Transfer **127**: 838-856.
- Rabienataj Darzi, A. A., M. Jourabian and M. Farhadi (2016). "Melting and solidification of PCM enhanced by radial conductive fins and nanoparticles in cylindrical annulus." Energy Conversion and Management **118**: 253-263.
- Rahimi, M., A. A. Ranjbar, D. D. Ganji, K. Sedighi, M. J. Hosseini and R. Bahrampoury (2014). "Analysis of geometrical and operational parameters of PCM in a fin and tube heat exchanger." International Communications in Heat and Mass Transfer **53**: 109-115.
- Rathod, M. K. and J. Banerjee (2013). "Thermal performance of phase change material-based latent heat thermal storage unit." Heat Transfer - Asian Research **43**(8): 706-719.
- Rathod, M. K. and J. Banerjee (2015). "Thermal performance enhancement of shell and tube Latent Heat Storage Unit using longitudinal fins." Applied Thermal Engineering **75**: 1084-1092.
- Raul, A. K., P. Bhavsar and S. K. Saha (2018). "Experimental study on discharging performance of vertical multitube shell and tube latent heat thermal energy storage." Journal of Energy Storage **20**: 279-288.

- Rempel, A. and A. Rempel (2013). "Rocks, Clays, Water, and Salts: Highly Durable, Infinitely Rechargeable, Eminently Controllable Thermal Batteries for Buildings." Geosciences **3**(1): 63-101.
- Rizan, M. Z. M., F. L. Tan and C. P. Tso (2012). "An experimental study of n-octadecane melting inside a sphere subjected to constant heat rate at surface." International Communications in Heat and Mass Transfer **39**(10): 1624-1630.
- Sciacovelli, A., F. Gagliardi and V. Verda (2015). "Maximization of performance of a PCM latent heat storage system with innovative fins." Applied Energy **137**: 707-715.
- Seddegh, S., X. Wang and A. D. Henderson (2016). "A comparative study of thermal behaviour of a horizontal and vertical shell-and-tube energy storage using phase change materials." Applied Thermal Engineering **93**: 348-358.
- Seddegh, S., X. Wang, M. M. Joybari and F. Haghghat (2017). "Investigation of the effect of geometric and operating parameters on thermal behavior of vertical shell-and-tube latent heat energy storage systems." Energy **137**: 69-82.
- Sharma, A., V. V. Tyagi, C. R. Chen and D. Buddhi (2009). "Review on thermal energy storage with phase change materials and applications." Renewable and Sustainable energy reviews **13**(2): 318-345.
- Skaalum, J. and D. Groulx (2017). Experimental Investigation of Bifurcated-Fin Heat Exchanger for Latent Heat Energy Storage System. 9th World Conference on Experimental Heat Transfer, Fluid Mechanics and Thermodynamics. Iguazu Falls, Brazi: 12 p.
- Sparrow, E. M. and J. A. Broadbent (1982). "Inward Melting in a Vertical Tube Which Allows Free Expansion of the Phase-Change Medium." journal of Heat Transfer **104**(2): 309-315.
- Sparrow, E. M. and J. A. Broadbent (1983). "Freezing in a Vertical Tube." Journal of Heat Transfer **105**(2): 217-225.
- Sponagle, B. N. and D. Groulx (2016). Numerical Study of Temperature Control in Tablet Computers using Phase Change Material Thermal Energy Storage. 4th International Forum on Heat Transfer, IFHT2016. Sendai (Japan): 6 p.
- Tatsidjoudoung, P., N. Le Pierrès and L. Luo (2013). "A review of potential materials for thermal energy storage in building applications." Renewable and Sustainable Energy Reviews **18**: 327-349.
- Tay, N. H. S., M. Belusko and F. Bruno (2012). "Experimental investigation of tubes in a phase change thermal energy storage system." Applied Energy **90**(1): 288-297.
- Tay, N. H. S., M. Belusko, A. Castell, L. F. Cabeza and F. Bruno (2014). "An effectiveness-NTU technique for characterising a finned tubes PCM system using a CFD model." Applied Energy **131**: 377-385.
- Tay, N. H. S., F. Bruno and M. Belusko (2012). "Experimental validation of a CFD model for tubes in a phase change thermal energy storage system." International Journal of Heat and Mass Transfer **55**(4): 574-585.

- Trp, A., K. Lenic and B. Frankovic (2006). "Analysis of the influence of operating conditions and geometric parameters on heat transfer in water-paraffin shell-and-tube latent thermal energy storage unit." Applied Thermal Engineering **26**(16): 1830-1839.
- Wang, C., T. Lin, N. Li and H. Zheng (2016). "Heat transfer enhancement of phase change composite material: Copper foam/paraffin." Renewable Energy **96**: 960-965.
- Wolff, F. and R. Viskanta (1988). "Solidification of pure metal at a vertical wall in the presence of liquid superheat." International Journal of Heat and Mass Transfer **31**(8): 1735-1744.
- Xiao, X., P. Zhang and M. Li (2013). "Preparation and thermal characterization of paraffin/metal foam composite phase change material." Applied Energy **112**: 1357-1366.
- Yazici, M. Y., M. Avci, O. Aydin and M. Akgun (2014). "On the effect of eccentricity of a horizontal tube-in-shell storage unit on solidification of a PCM." Applied Thermal Engineering **64**(1-2): 1-9.
- Youssef, W., Y. T. Ge and S. A. Tassou (2018). "CFD modelling development and experimental validation of a phase change material (PCM) heat exchanger with spiral-wired tubes." Energy Conversion and Management **157**: 498-510.
- Yusuf Yazıcı, M., M. Avci, O. Aydın and M. Akgun (2014). "Effect of eccentricity on melting behavior of paraffin in a horizontal tube-in-shell storage unit: An experimental study." Solar Energy **101**: 291-298.
- Zhao, C. Y., W. Lu and Y. Tian (2010). "Heat transfer enhancement for thermal energy storage using metal foams embedded within phase change materials (PCMs)." Solar Energy **84**(8): 1402-1412.
- Zheng, X., N. Xie, C. Chen, X. Gao, Z. Huang and Z. Zhang (2018). "Numerical investigation on paraffin/expanded graphite composite phase change material based latent thermal energy storage system with double spiral coil tube." Applied Thermal Engineering **137**: 164-172.

# Appendix A: Copper coil drawings

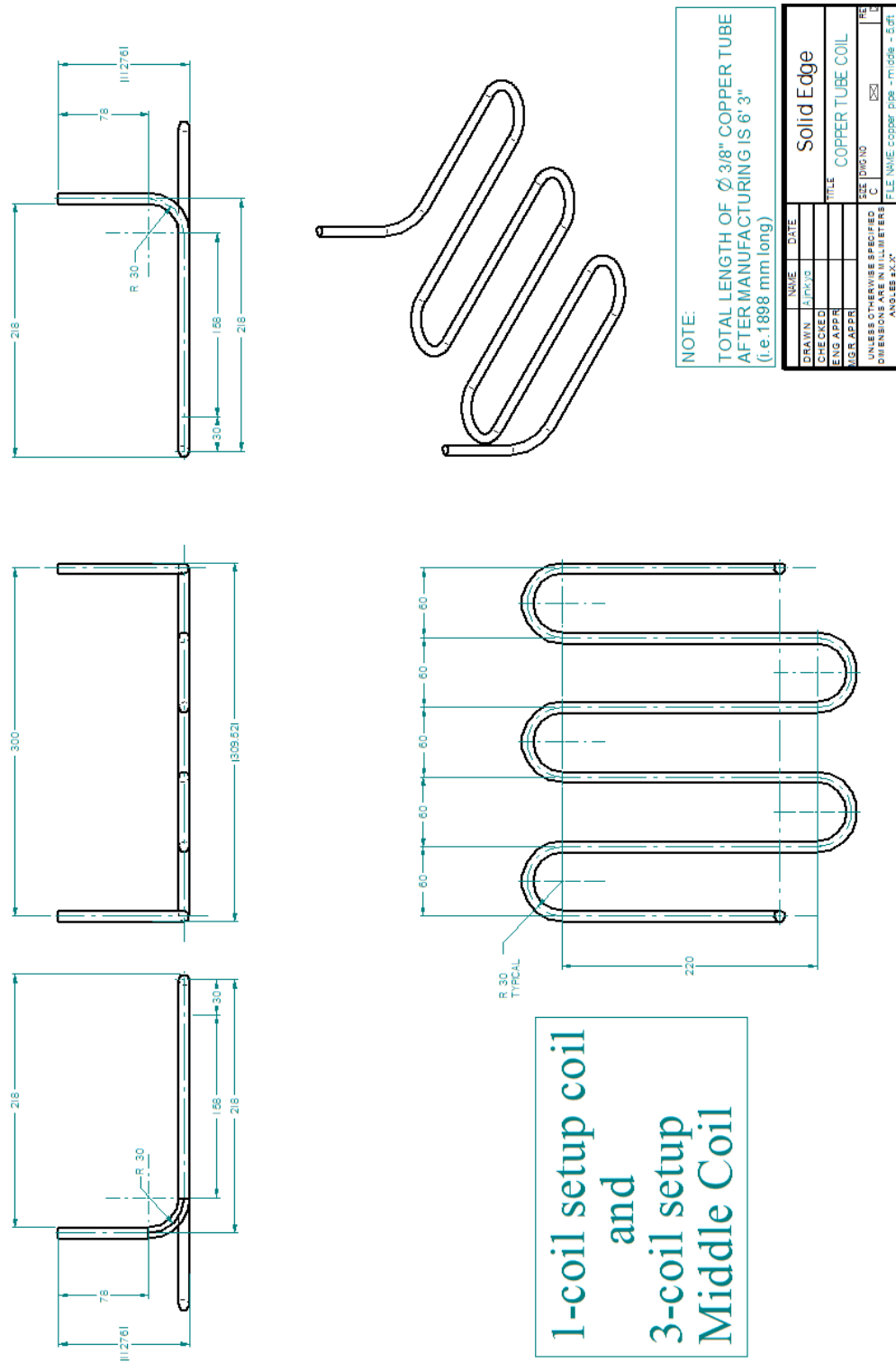
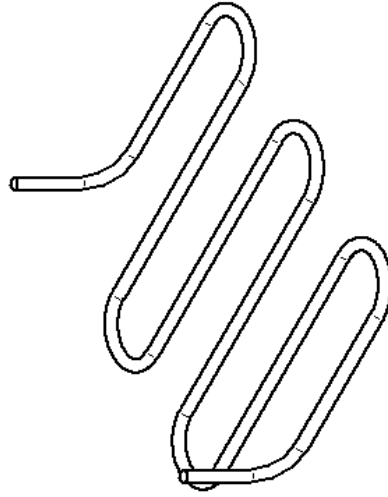
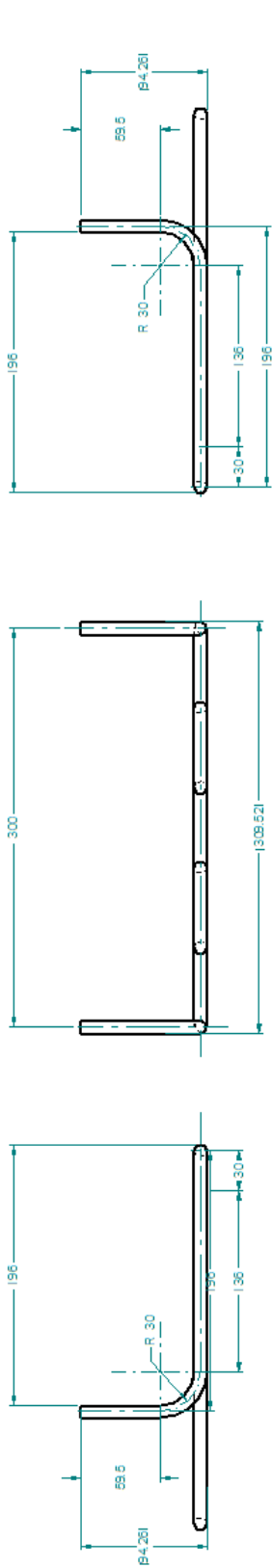


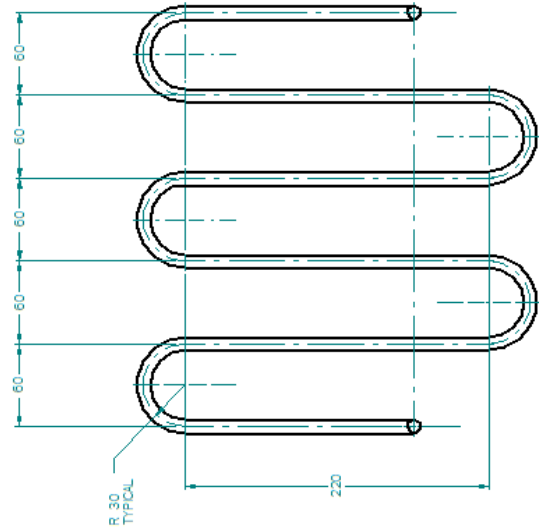
Figure A.1: Drawing of 1-coil setup coil or 3-coil setup middle coil.

+



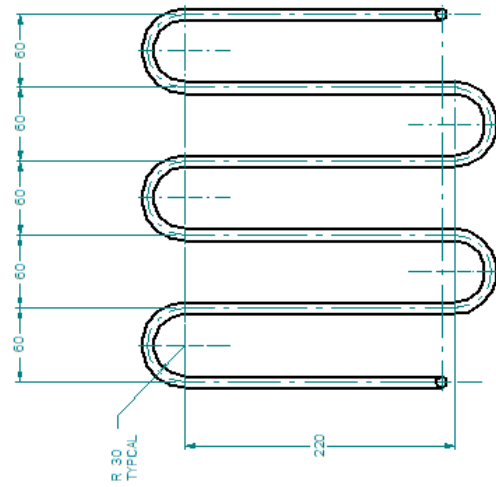
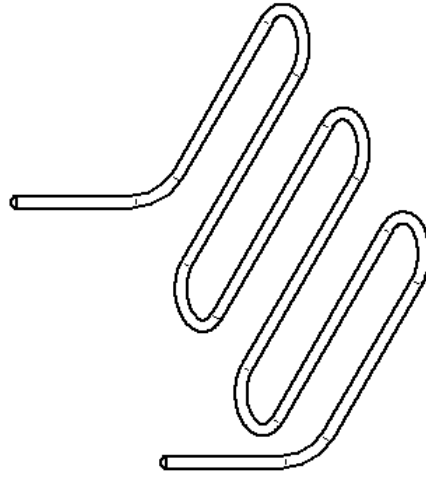
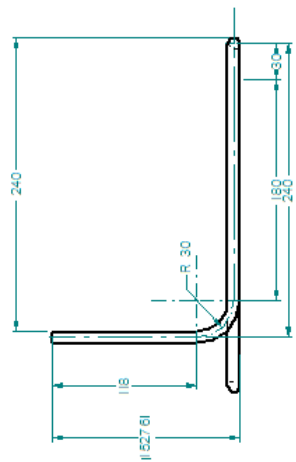
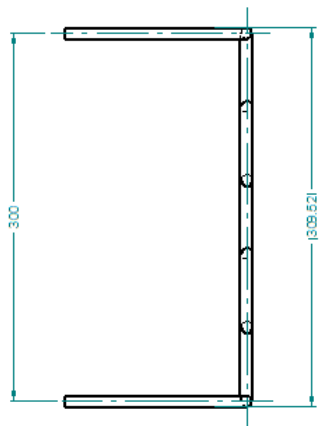
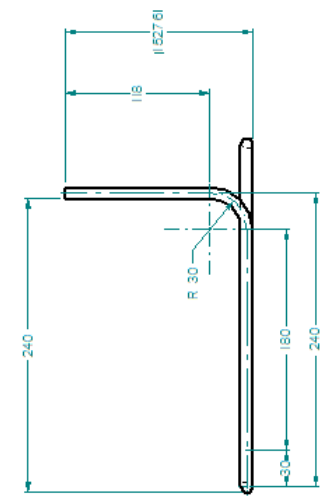
NOTE:  
TOTAL LENGTH OF  $\varnothing$  3/8" COPPER TUBE  
AFTER MANUFACTURING IS 5' 11"  
(i.e. 1798 mm long)

DATE	NAME	DATE	NAME
	DRAWN		CHECKED
	CHKD		ENGR
	APPD		APPD
	DATE		DATE
	SCALE		SCALE
	UNLESS OTHERWISE SPECIFIED DIMENSIONS ARE IN MILLIMETERS		
	ANGLES IN DEGREES		
	FILE NAME: C:\COPPER\008 - Top - 2.TUBES -		



3-coil setup  
Top Coil

Figure A.2: Drawing of top coil in the 3-coil setup.



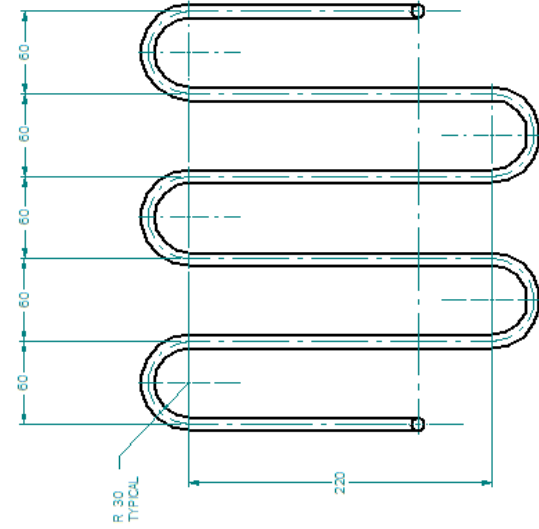
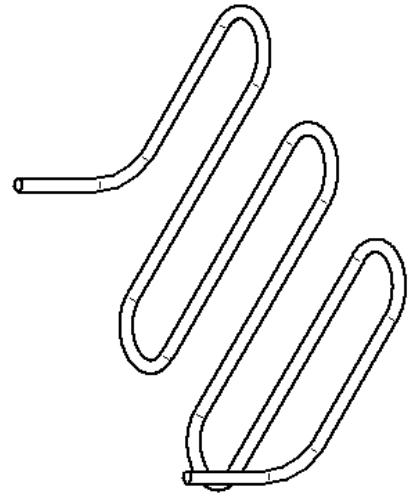
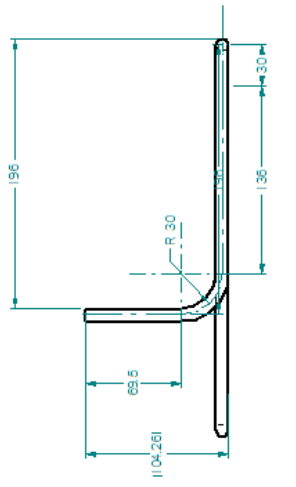
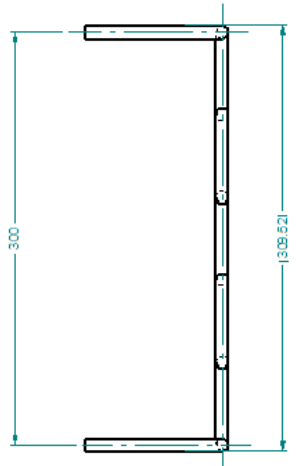
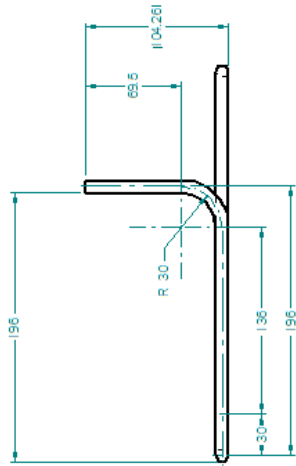
3-coil setup  
Bottom coil

NOTE:

TOTAL LENGTH OF  $\varnothing 3/8"$  COPPER TUBE  
AFTER MANUFACTURING IS 6' 8"  
(i.e. 2011 mm long)

DATE	DATE	Solid Edge
DRAWN	CHK'D	TITLE
CHECKED	ENG APPR	COPPER TUBE COIL
ENG APPR	SIZE	DWG NO
UNLESS OTHERWISE SPECIFIED	C	REV
DIMENSIONS ARE IN MILLIMETERS	1:1	FILE NAME: COOPER_TUBE_BOTTOM_COIL
ANGLES XXX°		

Figure A.3: Drawing of bottom coil in the 3-coil setup.



2-coil setup  
Top Coil

**NOTE:**  
TOTAL LENGTH OF  $\varnothing 3/8"$  COPPER TUBE  
AFTER MANUFACTURING IS 5'11"  
(i.e. 1798 mm long)

NAME	DATE	Solid Edge
DRAWN	JLR/10/10	
CHECKED		
ENG APPR		
DES APPR		TITLE COPPER TUBE COIL
UNLESS OTHERWISE SPECIFIED DIMENSIONS ARE IN MILLIMETERS ANGLES IN DEG		SEE DWG NO <input checked="" type="checkbox"/> REV FILE NAME: C:\COPPER\TOP - 2-10-08

Figure A.4: Drawing of top coil in the 2-coil setup.

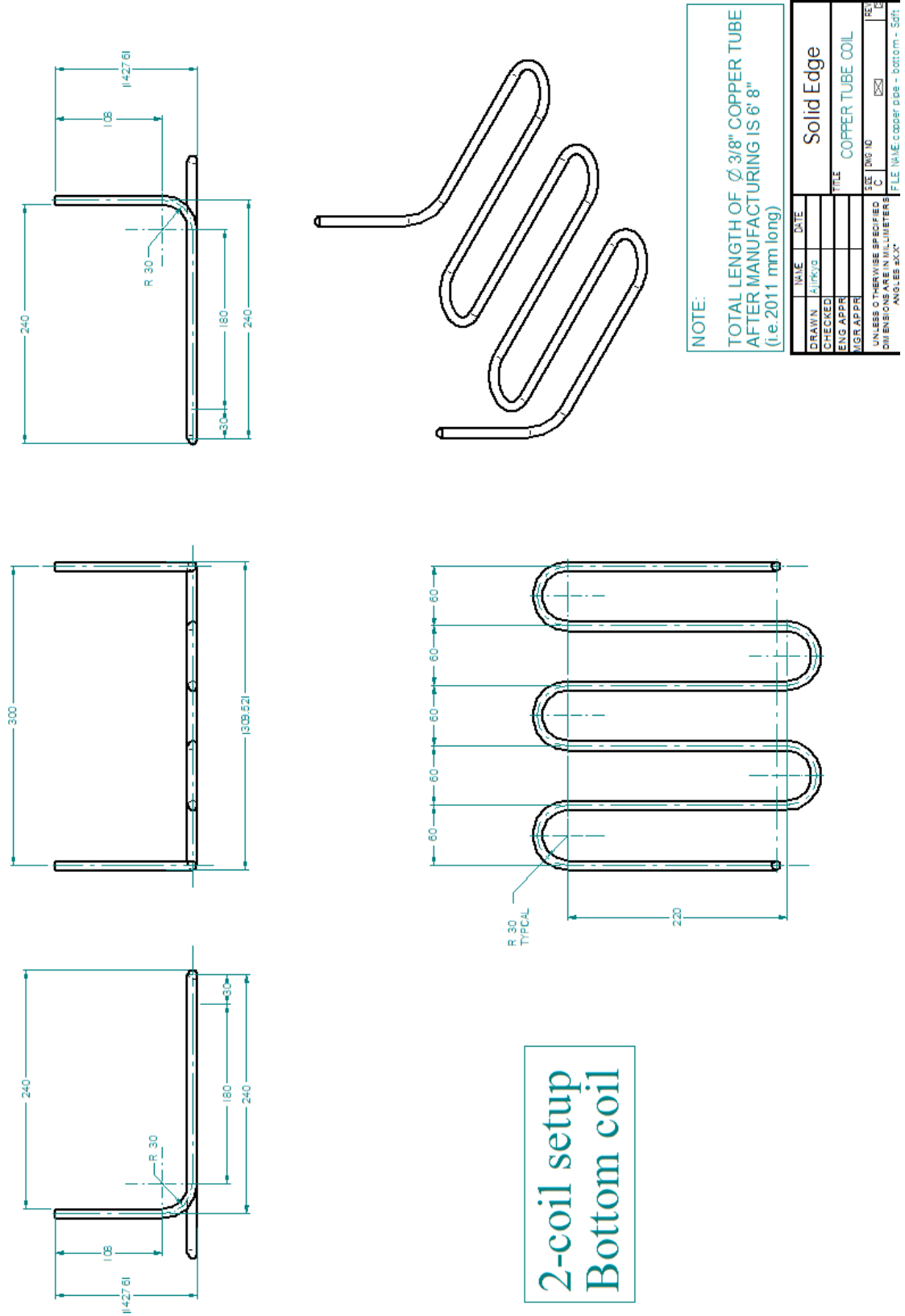
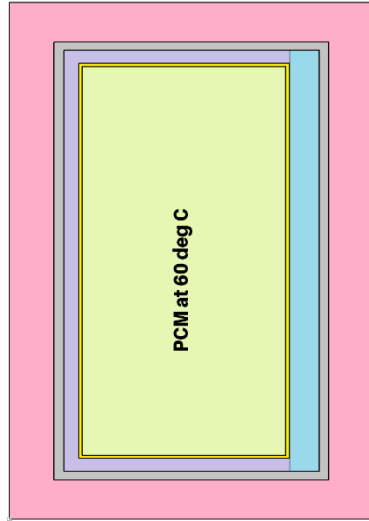


Figure A.5: Drawing of bottom coil in the 2-coil setup.



# Appendix B: Heat loss calculations

$$R_{top} = 0.075 + 0.44 + 0.65 + 1 = 2.165 \text{ (m}^2 \cdot \text{K/W)}$$

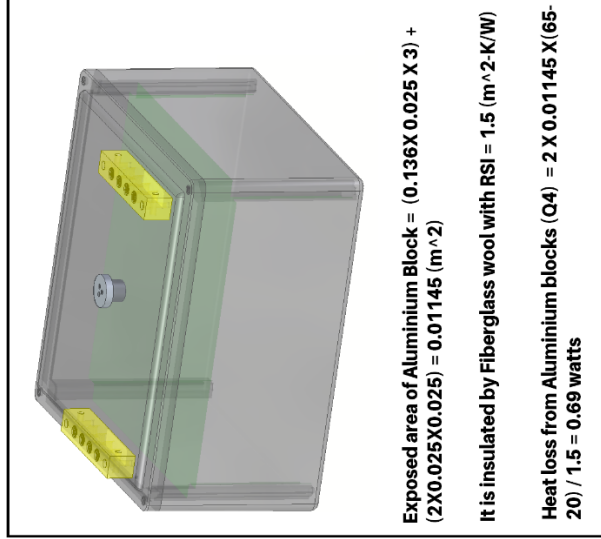


- Fiber glass box (RSI - 0.075)
- 1/2" polystyrene (RSI - 0.44)
- 1" Polystyrene (RSI - 0.88)
- 5/16" bubble wrap (RSI - 0.65)
- Fiberglass wool (RSI - 1)

Ambient Temperature = 20 deg C

$$R_{side} = 0.075 + 0.44 + 0.65 + 1 = 2.165 \text{ (m}^2 \cdot \text{K/W)}$$

$$R_{bottom} = 0.075 + 0.88 + 0.65 + 1 = 2.61 \text{ (m}^2 \cdot \text{K/W)}$$



Exposed area of Aluminium Block =  $(0.136 \times 0.025 \times 3) + (2 \times 0.025 \times 0.025) = 0.01145 \text{ (m}^2)$

It is insulated by Fiberglass wool with RSI = 1.5  $(\text{m}^2 \cdot \text{K/W})$

Heat loss from Aluminium blocks (Q4) =  $2 \times 0.01145 \times (65 - 20) / 1.5 = 0.69 \text{ watts}$

$$\text{Top Area} = 0.386 \times 0.335 = 0.13 \text{ (m}^2)$$

$$\text{Side Area} = 2(0.386 + 0.335) \times 0.178 = 0.257 \text{ (m}^2)$$

$$\text{Bottom Area} = 0.386 \times 0.335 = 0.13 \text{ (m}^2)$$

$$\text{Heat loss from the top face (Q1)} = \text{Area} \times \text{DT} / R_{top} = 0.13 \times (60 - 20) / 2.165 = 2.40 \text{ watts}$$

$$\text{Heat loss from side faces (Q2)} = \text{Area} \times \text{DT} / R_{side} = 0.257 \times (60 - 20) / 2.165 = 4.75 \text{ watts}$$

$$\text{Heat loss from bottom face (Q3)} = \text{Area} \times \text{DT} / R_{bottom} = 0.13 \times (60 - 20) / 2.61 = 2 \text{ watts}$$

**Total heat loss from the box (Q<sub>box</sub>) = Q1 + Q2 + Q3 + Q4 = 2.4 + 4.75 + 2 + 0.69 = 9.84 ~ 10 watts**

**Experimentally observed heat loss value = 11 to 12 watts**

# Appendix C: Data sheets

## Cole Parmer Water Bath Specifications

Stainless Steel Cooling/Heating Circulating Baths with Advanced Circulator				
Catalog Part Number Nameplate Identification	12122-12 3C6	12122-26 3C6F	12122-42 3C15	12122-56 3C15++
<b>Temperature Range</b> °C °F	-20 to 100 -4 to 212	-20 to 100 -4 to 212	-28 to 200 -18 to 392	-35 to 200 -31 to 392
<b>Heater Capacity</b> KWatts	1.2	1.2	1.2	1.2
<b>Stability</b> °C	0.025	0.025	0.025	0.025
<b>Bath Volume</b> liters gallons	5.4 - 6.5 1.4 - 1.7	5.4 - 6.5 1.4 - 1.7	6.8 - 8.6 1.8 - 2.3	6.8 - 8.6 1.8 - 2.3
<b>Cooling Capacity</b> watts @20°C	250	250	500	800
<b>Refrigerant</b>	R134a	R134a	R134a	R404a
<b>Dimensions<sup>1</sup></b> (H x W x L) mm inches	640.0 x 203.2 x 416.6 25.2 x 8.0 x 16.4	444.5 x 467.4 x 416.6 17.5 x 18.4 x 16.4	655.3 x 259.1 x 490.2 25.8 x 10.2 x 19.3	706.1 x 370.8 x 528.3 27.8 x 14.6 x 20.8
<b>Electrical</b> Nominal VAC Operating VAC Range Operating Frequency Input Current Rating Amps Total Wattage Line Cord Plug (NEMA)	115V 103V - 127V 60 Hz 11.5 1328 N5-15	115V 103V - 127V 60 Hz 11.5 1328 N5-15	115V 103V - 127V 60 Hz 11.7 1345 N5-15	115V 103V - 127V 60 Hz 14.4 1662 N5-20
<b>Net Weight</b> kg lb	27.2 60.0	29.9 66.0	36.3 80.0	55.8 123.0

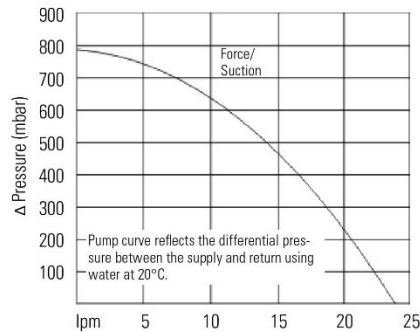
\*Overall dimensions. Add -15 mm to L for drain fitting

- Stability is measured as follows:

Fluid (specific heat of 0.55 Btu/lb-F) at -10°C, work area cover is on. Baths run in factory ambient at nominal line voltage. Pump speed set to high with short insulated loop on pump lines.

Stability is defined as ½ the total span of measured data over approximately 30 minutes.

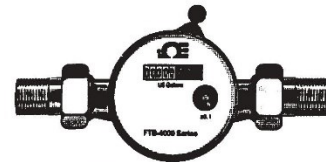
- Cole Parmer reserves the right to change specifications without notice.



- Pump testing is done with water at 20°C bath at nominal line voltage on high pump speed. Approximately one meter loop on pump with flow transducer and (2) pressure transducers with a ball valve to adjust the flow rate.



**Ω OMEGA™**  
**FTB-4000 and FTB-5000 Series**  
**Turbine Meters for Water**  
**Operator's Manual:**



FTB-4000 Shown

INSTRUCTION  
SHEET

M0504/1218

Shop online at [omega.com](http://omega.com) e-mail: [info@omega.com](mailto:info@omega.com)  
For latest product manuals: [www.omegamanual.info](http://www.omegamanual.info)

## General Description

Specifically designed for water billing applications, **Omega FTB-4000 and FTB-5000 Series Flow meters** are highly accurate and feature tamper-resistant, non-resettable totalizers. The large faces are easy to read and are fully rotatable for simplified mounting. **FTB-4605 and FTB-4607** have no local indication of the flow rate or total.

Optional reed relay scaled pulse outputs allow for remote totalization (6 feet of cable included). For the **FTB-4000 Series**, the pulse output is factory installed and must be requested at the time of order.

The **FTB-5000 Series** units feature field installation of the reed relay or optical pickup pulse outputs. The optical pickup is used for use with flow rate frequency meters to provide remote rate indication (user DC power input required). **FTB-5000** units are supplied standard with one reed relay for remote totalization; a second relay is optional.

All **FTB** flow meters feature built-in strainers and are shipped complete with locking nuts, gaskets and coupling pieces. The units have a built-in flow finder which registers even a small trickle of water passing through the meter.

## WARNING

THESE WATER FLOW METERS HAVE PLASTIC INTERNAL PARTS THAT ARE RAPIDLY ATTACKED BY HYDROCARBON FLUIDS, SUCH AS GASOLINE, DIESEL FUEL, KEROSENE, AND SIMILAR MATERIALS. EVEN TRACE AMOUNTS OF THESE MATERIALS IN WATER WILL TEND TO ACCUMULATE IN THE PLASTIC PARTS LEADING TO COMPLETE FAILURE OF THE FLOW METER. NOTE: WATER AND ETHYLENE GLYCOL MIXTURES TYPICALLY PRESENT NO PROBLEM WHEN USED WITH THESE WATER FLOWMETERS.

## UNPACKING

Remove the packing list and verify that all equipment has been received. If there are any questions about the shipment, please call the **Omega Customer Service Department**.

Upon receipt of shipment, inspect the container and equipment for any signs of damage. Take particular note of any evidence of rough handling in transit. Immediately report any damage to the shipping agent.

## NOTE

The carrier will not honor any claims unless all shipping material is saved for their examination. After examining and removing contents, save packing material and carton in the event reshipment is necessary.

## MOUNTING

The **FTB-4000 Series** (only all 1/2" and 3/4") can be mounted either horizontally or vertically.

All **FTB-4000 Series** 1", 1 1/4", 1 1/2" and 2" horizontal only.

**FTB-5000X - FTB-5020** horizontal only.

**FTB-5020X to FTB-5080** all can be mounted either horizontally or vertically.



## SPECIFICATIONS (CONT'D)

### ACCURACY:

4600 Series:	From 10% of cont. to max. flow: $\pm 1.5\%$ of reading
	Below 10% of cont. flow: $\pm 2\%$ of reading
4000, 5000 Series:	From 20% of cont. to max. flow: $\pm 1\%$ of reading
	Below 20% of cont. flow: $\pm 3\%$ of reading

### MAX. TEMPERATURE:

4000 Series:	122°F (50°C)
4100 Series:	190°F (87.7°C)
4600 Series:	190°F (87.7°C)
5000 Series:	248°F (120°C)

### MAX. PRESSURE:

4000, 4600 Series:	150 PSI
5000 Series:	250 PSI

### PULSE OUTPUTS:

	Reed relay
4100P Series:	1 gal./pulse
5010 - 5020:	1 or 10 gal./pulse
5020X - 5040:	10 gal./pulse
5060 & 5080:	100 gal./pulse

### FTB4600 HIGH RESOLUTION PULSE OUTPUT:

FTB4605:	151.4 pulses/gal.
FTB4607:	75.7 pulses/gal. Requires 6-16 VDC @ 10mA max power; output requires pull-up to positive DC voltage.

### (OPTICAL PICKUP (= MIN. INCREMENT)):

5010 - 5020X:	0.5 gal./pulse
5030 & 5040:	1 gal./pulse
5060 & 5080:	5 gal./pulse

### MAX. READING (GAL.):

4000 Series:	100,000,000
5010 - 5040:	10,000,000
5060 - 5080:	100,000,000

### HOUSING:

4000, 4100, 5005 - 5015:	Cast brass
5020 - 5080:	Cast iron
4600 Series:	Brass

### BEARING:

Ceramic/sapphire

### TURBINE:

High temperature thermoplastic/fiberglass (polyimide)

### FLOW TRANSFER:

Ceramic magnet

### OTHER WETTED PARTS:

Stainless steel, polypropylene, EPDM O-ring





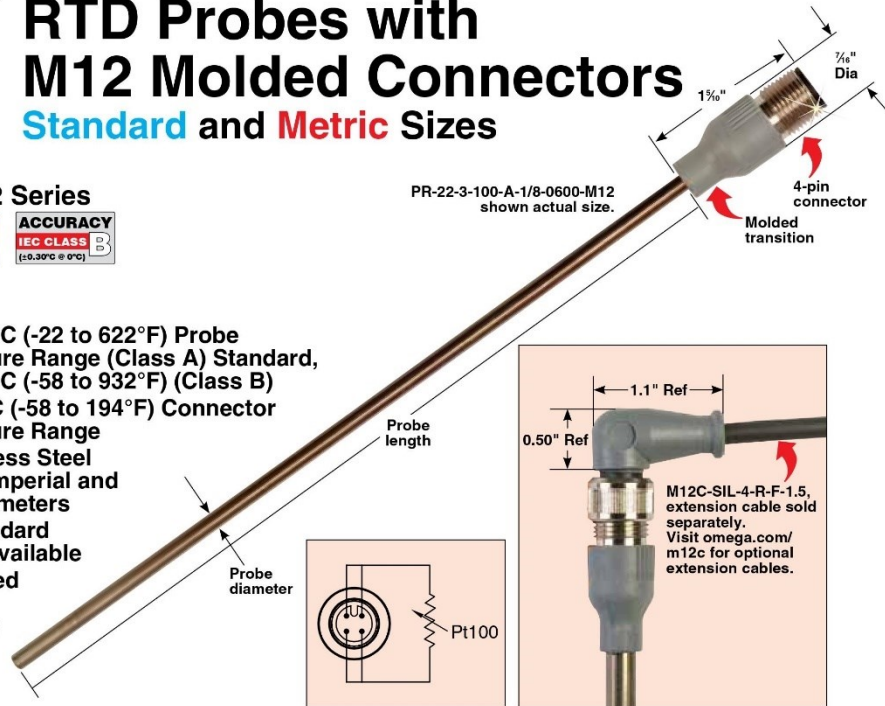
# RTD Probes with M12 Molded Connectors

## Standard and Metric Sizes

### PR-22 Series



- ✓ -30 to 350°C (-22 to 622°F) Probe Temperature Range (Class A) Standard, -50 to 500°C (-58 to 932°F) (Class B)
- ✓ -50 to 90°C (-58 to 194°F) Connector Temperature Range
- ✓ 316 Stainless Steel Probe in Imperial and Metric Diameters
- ✓ Many Standard Lengths Available
- ✓ IP67 Molded 4-Pin M12 Connector



### Standard

To Order Visit <a href="http://omega.com/pr-22">omega.com/pr-22</a> for Pricing and Details		
Model Number	Probe Length	Element Specification
PR-22-3-100-A-(*)-0600-M12	6"	Pt100, Class A
PR-22-3-100-A-(*)-0900-M12	9"	Pt100, Class A
PR-22-3-100-A-(*)-1200-M12	12"	Pt100, Class A
PR-22-3-100-A-(*)-1800-M12	18"	Pt100, Class A
PR-22-3-100-A-(*)-2400-M12	24"	Pt100, Class A

(\*) = Insert probe diameter of 1/8 of 1/4 inches.

For Class B, change "A" in model number to "B" and visit [omega.com/pr-22](http://omega.com/pr-22) for pricing.

Ordering Examples: PR-22-3-100-A-1/8-0600-M12, 1/8" diameter by 6" long Pt100 Class A RTD sensor with molded M12 connector.

PR-22-3-100-A-1/4-1200-M12, 1/4" diameter by 12" long Pt100 Class A RTD sensor with molded M12 connector.

### Metric

Model Number	Probe Length	Element Specification
PR-22-3-100-A-(*)-100-M12	100 mm	Pt100, Class A
PR-22-3-100-A-(*)-150-M12	150 mm	Pt100, Class A
PR-22-3-100-A-(*)-250-M12	250 mm	Pt100, Class A
PR-22-3-100-A-(*)-350-M12	350 mm	Pt100, Class A
PR-22-3-100-A-(*)-500-M12	500 mm	Pt100, Class A
PR-22-3-100-A-(*)-750-M12	750 mm	Pt100, Class A
PR-22-3-100-A-(*)-1000-M12	1000 mm	Pt100, Class A

(\*) = Insert probe diameter of "M2", "M3" or "M6" for 2 mm, 3 mm or 6 mm probe diameters shown in table. (M2 only available in 150 mm and 250 mm lengths.

For Class B, change "A" in model number to "B" and visit [omega.com/pr-22](http://omega.com/pr-22) for pricing.

Ordering Examples: PR-22-3-100-A-M3-250-M12, 3 mm diameter by 250 mm long Pt100 Class A RTD sensor with molded M12 connector.

PR-22-3-100-A-M6-500-M12, 6 mm diameter by 500 mm long Pt100 Class A RTD sensor with molded M12 connector.

OMEGAFILM® elements are manufactured to meet the requirements of IEC Standard 60751. This standard uses “Classes” to define the accuracy and interchangeability for the elements, the basic resistance vs. temperature characteristics, temperature ranges and other technical information relating to the OMEGAFILM RTD elements. Key portions of these requirements are summarized below.

Thin Film Interchangeability in °C			
Temp °C	Class B	Class A	½ DIN (AA)
-50	0.55	—	—
-30	0.45	0.21	—
0	0.30	0.15	0.10
100	0.80	0.35	0.27
150	1.05	0.45	0.36
200	1.30	0.55	—
300	1.80	0.75	—
400	2.30	—	—
500	2.80	—	—

**Accuracy Classes**

There are three accuracy “Classes” defined in IEC60751 for film type RTDs, they are: “Class A”, “Class B”, and ½ DIN (also known as AA). These “Classes” are defined as follows:

Tolerance (°C)	Temperature Range*
Class A = ±(0.15 + 0.002t)	(-30 to 300°C)
Class B = ±(0.30 + 0.005t)	(-50 to 500°C)
Class AA (was ½ DIN) = ±(0.1 + 0.0017t)	(0 to 150°C)
t = Temperature °C	

*Note: There is also an industry standard 1/10 DIN accuracy not available in film style RTDs.*

*\* Note: The temperature ranges shown are not the temperature ratings for the sensors. Temperature ranges for each product have been provided, please see the applicable page.*

**Equations**

Platinum RTD resistance can be calculated using the Callendar-Van Dusen Equation as follows:

For temperatures below 0°C: Rt = R0 [1 + At + Bt² + C(t-100)t³]	For temperatures above 0°C, this simplifies to: Rt = R0 (1 + At + Bt²)
where: A = 3.9083 x10 <sup>-3</sup> (C <sup>-1</sup> ) B = -5.775 x10 <sup>-7</sup> (C <sup>-2</sup> ) C = -4.183 x10 <sup>-12</sup> (C <sup>-4</sup> ) R0 = Resistance at 0°C t = Temperature in degrees celsius	

**Maximum Operating Current**

The maximum operating current is determined by the amount of electrical current that can be passed through the element without significant self heating occurring. OMEGA recommends a maximum operating current of 1 milliamp for all of the 100 ohm elements and sensors we supply. Higher or lower currents may be suitable for other resistances or sensor products, OMEGA recommends testing, for self heating effects before use.

**Resistance vs. Temperature Values per IEC60751**

Temp (°C)	Resistance (Ω)	Temp (°C)	Resistance (Ω)	Temp (°C)	Resistance (Ω)
-200	18.52	150	157.33	450	264.18
-150	39.72	200	175.86	500	280.98
-50	80.31	250	194.10	550	297.49
0	100.00	300	212.05	600	313.71
50	119.40	350	229.72	650	329.64
100	138.50	400	247.09	700	345.28

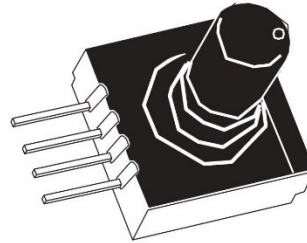






# PX26 SERIES

Pressure Transducers



M1608/1018

Shop online at: [omega.com](http://omega.com) e-mail: [info@omega.com](mailto:info@omega.com)  
For latest product manuals: [omegamannual.info](http://omegamannual.info)

## GENERAL INFORMATION

Omega's Pressure sensors are four-active piezoresistive bridge devices. When pressure is applied, a different output voltage proportional to that pressure, is produced.

Wet/Wet Differential Pressure Sensors simultaneously accept independent pressure sources. Gage Pressure Sensors provide a form of differential pressure measurement in which atmospheric pressure is used as a reference.

The PX26 is available in variety of PSI ranges and as differential and gage sensors:

MODEL NUMBER (GAGE)	RANGE	MODEL NUMBER (DIFFERENTIAL)	RANGE
PX26-001GV	0-1 PSIG	PX26-001 DV	0-1 PSID
PX26-005GV	0-5 PSIG	PX26-005DV	0-5 PSID
PX26-015GV	0-10 PSIG	PX26-015DV	0-15 PSID
PX26-030GV	0-30 PSIG	PX26-030DV	0-30 PSID
PX26-100GV	0-100 PSIG	PX26-100DV	0-100 PSID
PX26-250GV	0-250 PSIG	PX26-250DV	0-250 PSID

## UNPACKING

Remove the packing list and verify that all equipment has been received. If there are any questions about the shipment, please call Omega Customer Service Department at 1-800-622-2378 or 203-359-1600. We can also be reached on the Internet at [omega.com](http://omega.com) e-mail: [info@omega.com](mailto:info@omega.com)

Upon receipt of shipment, inspect the container and equipment for any signs of damage. Take particular note of any evidence of rough handling in transit. Immediately report any damage to the shipping agent.

NOTE

The carrier will not honor any claims unless all shipping material is saved for their examination. After examining and removing contents, save packing material in event reshipment is necessary.

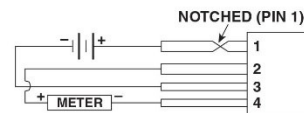
## MEDIA COMPATIBILITY

Input media are limited to those media which will not attack polyester, fluoro-silicon, or silicon, such as oils, lacquer thinner, hydraulic fluid, most petroleum products, water and salt water. Not recommended for freons.

## SOLDERING

Limit soldering temperature to 600°F (315°C) for 10 seconds duration maximum.

## ELECTRICAL CONNECTION



### WARNING! READ BEFORE INSTALLATION

Fluid hammer and surges can destroy any pressure transducer and must always be avoided. A pressure snubber should be installed to eliminate the damaging hammer effects.

Fluid hammer occurs when a liquid flow is suddenly stopped, as with quick closing solenoid valves. Surges occur when flow is suddenly begun, as when a pump is turned on at full power or a valve is quickly opened.

Liquid surges are particularly damaging to transducers if pipe is original empty. To avoid damaging surges, fluid lines should remain full (if possible), ports should be up to power slowly, and valves opened slowly. To avoid damage from both fluid hammer and surges, a surge chamber should be installed, and a pressure snubber should be installed on every transducer.

Symptoms of fluid hammer and surges damaging effects:

- a) Pressure transducer exhibits an output at zero pressure (large zero offset). If offset is less than 10% FS, user can usually re-zero meter, install proper snubber and continue monitoring pressures.
- b) Pressure transducer output remains constant regardless of pressure.
- c) In severe cases, there will be no output.

**SPECIFICATIONS**

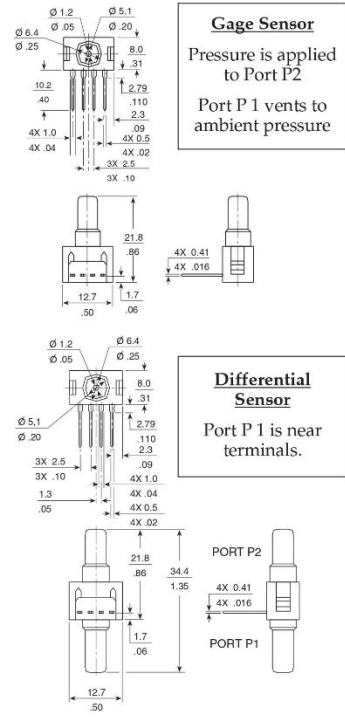
**EXCITATION:**  
**OUTPUT:**

**ACCURACY:**  
**LINEARITY:**  
**HYSTERESIS & REPEATABILITY:**  
**ZERO BALANCE:**  
**SPAN TOLERANCE:**  
**STORAGE TEMPERATURE:**  
**OPERATING TEMPERATURE:**  
**COMPENSATED TEMPERATURE:**  
**THERMAL EFFECTS:**  
**PROOF PRESSURE:**

**INPUT RESISTANCE:**  
**OUTPUT RESISTANCE:**  
**RESPONSE TIME:**  
**SHOCK:**  
**VIBRATION:**  
**GAGE TYPE:**  
**WETTED PARTS:**  
**MATING CONNECTOR:**  
**PRESSURE PORT:**  
**ELECTRICAL CONNECTION:**

**WEIGHT:**

10Vdc, 16Vdcmax @ 2mA  
100mV, 1 10mV/V  
(16.7mV, 1.67mV/V for  
1 PSI range)  
(50mV, 5mV/V for 5PSI range)  
1% FS  
1.0% FS BFSL  
0.2% FS  
±1.5mV  
±3.0 mV  
-67° to 212°F (-55° to 100°C)  
-40 to 185°F (-40° to 85°C)  
32° to 122°F (0° to 50°C)  
**ZERO:** 1 mV  
**SPAN:** 1% Rdg  
20 PSI for 1 and 5 PSI range  
45 PSI for 15 PSI range  
60 PSI for 30 PSI range  
200 PSI for 100 PSI range  
500 PSI for 250 range  
7.5k Ω  
2.5k Ω  
1 msec.  
Qualified to 150 G  
Qualified to 2kHz @ 20 G sine  
Silicon sensor  
Polyester, Silicon, fluorsilicon  
CX136-4, not included  
0.20" dia. & 0.25" collar dia.  
**Pin 1 +EXC** (notched)  
**Pin 2 +OUT**  
**Pin 3 -EXC**  
**Pin 4 -OUT**  
Approx 0.07 oz (2 gm)



# 7102 FLUKE Micro bath specifications

## 3.1 Specifications

Table 2. Specifications

<b>Range</b>	-5 to 125 °C (23 to 257 °F)
<b>Accuracy</b>	±0.25 °C
<b>Stability</b>	±0.015 °C at -5 °C (oil, 5010) ±0.03 °C at 121 °C (oil, 5010)
<b>Uniformity</b>	±0.02 °C
<b>Resolution</b>	0.01 °C/F
<b>Operating Temperature</b>	5 to 45 °C (41 to 113 °F)
<b>Heating Time</b>	25 °C to 100 °C (77 °F to 212 °F): 30 minutes
<b>Cooling Time</b>	25 °C to 0 °C (77 °F to 32 °F): 30 minutes
<b>Well Size</b>	2.5" dia. x 5.5" deep (64 x 139 mm) (access opening is 1.9" [48 mm] in diameter )
<b>Exterior Dimension</b>	12" H x 7.2" W x 9.5" D (31 cm x 18 cm x 24 cm)
<b>Weight</b>	15 lb. (6.8 kg) with fluid
<b>Power</b>	115 VAC ( ±10 %), 1.8 A, or 230 VAC ( ±10 %), 0.9 A, switchable, 50/60 Hz, 200 W
<b>Readout</b>	Switchable °C or °F
<b>Controller</b>	Digital controller with data retention
<b>Thermal Electric Devices (TED)</b>	150 W
<b>Cooling</b>	Fan and Thermal Electric Devices (TED)
<b>Fault Protection</b>	Sensor burnout and short protection
<b>Safety</b>	Overvoltage (Installation) Category II, Pollution Degree 2 per IEC 61010-01
<b>Fuse Rating</b>	115 V: 250 V 3A SB (slow blow) 230 V: 250 V 1.6 A T (time delay)